

# Mesoscopic quantum emitters coupled to plasmonic nanostructures

**Andersen, Mads Lykke**

*Publication date:*
2010

*Document Version*
Publisher's PDF, also known as Version of record

# Mesoscopic Quantum Emitters Coupled to Plasmonic Nanostructures

A dissertation
submitted to the Department of Photonics Engineering
at the Technical University of Denmark
in partial fulfillment of the requirements
for the degree of
philosophiae doctor

Mads Lykke Andersen
September 6, 2010

# Mesoscopic Quantum Emitters Coupled to Plasmonic Nanostructures

# Preface

This thesis describes research carried out from March 2007 to September 2010 at DTU Fotonik - The Department of Photonics Engineering at the Technical University of Denmark. The work was conducted in the course of my Ph.D. studies in the Quantum Photonics group within the Nanophotonics cluster under supervision of associate professor Peter Lodahl and professor Jesper Mørk.

The subject of this thesis falls within the field of solid state quantum optics, which as the name implies, is a multi-disciplinary field that incorporates elements of theoretical solid state physics, quantum mechanics, and optics. Traditionally, research within this field is divided into nano-structure fabrication, optical characterization, and theoretical modeling - with Ph.D. projects normally centered around one of these. That was, however, not the case with this project. This thesis covers all three subdisciplines and, as a consequence, a number of people have contributed to the results, which I intend to acknowledge with the following:

When I started my Ph.D. studies in the Quantum Photonics group I was introduced to the cleanroom facilities at DanChip by Søren Stobbe. We fabricated interface structures in GaAs, which are studied in Chapter 4. Søren had, prior to my arrival, developed the epitaxial lift-off procedure and also developed the procedure for turning the wafer upside-down. I began the fabrication of plasmonic nanowires guided by Rasmus Bundgaard Nielsen, who also provided helpful comments over the course of the development process of the waveguide fabrication recipe presented in Chapter 5. The optical measurements on single quantum dots coupled to plasmonic waveguides, presented in Chapter 5, were performed by Serkan Ates, who also participated in the waveguide fabrication. Throughout my studies Søren Stobbe also engaged with me in many theoretical discussion on the nature of decay dynamics of extended quantum emitters.

These discussion greatly helped to form the theoretical model presented in this thesis. For the calculation of decay dynamics near plasmonic waveguides, I used a finite-element code developed by Yuntian Chen, to calculate the field of the guided modes. The fabrication of plasmonic wedge waveguides was initiated by Søren Stobbe and performed by Jin Liu.

I would like to thank a number of people who have contributed to this project in various ways. Firstly, I would like to thank my supervisor Peter Lodahl, under whose supervision it has been a privilege to work, for teaching me the skills of excellent scientific practice and for guiding me into the field of solid state quantum optics. I would also like to show my gratitude towards Anders Søndberg Sørensen, who has been a collaborator throughout the project, for providing a seemingly newer-ending string of ideas for new structures to investigate, and Claus Birger Sørensen for providing the quantum dot wafers used in this thesis. I am also thankful towards Jørn Märcher Hvam and Jesper Mørk who have build-up and sustained a well-functioning scientific working environment and a pleasant atmosphere in the Nanophotonics cluster at DTU Fotonik.

I am thankful for the help I have received in the cleanroom from those mentioned above but also from Peixiong Shi, Kresten Yvind, David Larsson, and Luisa Ottaviano who have been helpful in various ways. Furthermore, I am glad for the collaborative atmosphere in the quantum photonics cluster and would like to express my appreciation towards: Toke Lund-Hansen, Henri Thyrrestrup Nielsen, Jin Liu, Kristian Høgh Madsen, David Garcia-Fernández, Luca Sapienza, and Qin Wang. Early in my Ph.D. studies I was introduced to the optical setup by Jeppe Johansen - whose skillful approach to optical alignment is a source of inspiration. Furthermore, I have during the course of my Ph.D.-studies consulted Philip Trøst Kristensen many times on theoretical questions of varying complexity and never walked away more puzzled than I came. I would like to thank Yuntian Chen, who provided the modeling framework for studying the coupling to plasmonic waveguides, and Serkan Ates who helped on their fabrication and who did measurements on these. I am indebted to Søren Stobbe for his involvement in my project, which would have turned out very differently without him.

During the last three years I have been working alongside many colleagues who have have grown to be my friends, especially I have appreciated the delight-

ful daily company of Philip Trøst Kristensen, Stephan Smolka, Per Lunnemann Hansen, Toke Lund-Hansen, and Søren Stobbe, with whom I have shared many good times both on and off campus.

Finally, I am grateful to my wife Signe for sharing all the highs and lows of scientific practice that I encountered throughout this project, and my daughter Frida for being such a beautiful little person who during my thesis-writing cared a great deal more about the sounds of various animals than about physics.

Mads Lykke Andersen
September 6th, 2010

# Abstract

This thesis reports research on quantum dots coupled to dielectric and plasmonic nano-structures by way of nano-structure fabrication, optical measurements, and theoretical modeling.

To study light-matter interaction, plasmonic gap waveguides with nanometer dimensions as well as samples for studies of quantum dots in proximity to semiconductor/air and semiconductor/metal interfaces, were fabricated.

We measured the decay dynamics of quantum dots near plasmonic gap waveguides and observed modified decay rates. The obtainable modifications with the fabricated structures are calculated to be too small to allow for efficient plasmon-based single-photon sources. Theoretical studies of coupling and propagation properties of plasmonic waveguides reveal that a high-refractive index of the medium surrounding the emitter, e.g. $n_{\mathrm{GaAs}} = 3.5$, limits the realizability of efficient plasmon-based single-photon sources using self-assembled quantum dots.

The measured decay dynamics of quantum dots in proximity to semiconductor/metal interfaces reveal that the dipole approximation generally does not hold for quantum dots due to their mesoscopic size. In order to explain the observations, a theoretical model for the spontaneous emission of mesoscopic quantum emitters is developed. The light-matter interaction is in this model modified beyond the dipole expectancy and found to both suppress and enhance the coupling to plasmonic modes in excellent agreement with our measurements.

We demonstrate that this mesoscopic effect can be utilized to strongly modify the coupling to plasmonic modes on metal nanowires and gap waveguides and we propose its use for spontaneous-emission control beyond the dipole approximation in nano-structured environments in general.

# Resumé

Denne afhandling beskriver forskning i koblingen af kvantepunkter til dielektriske og plasmoniske nano-strukturer ved hjælp af nano-fabrikation, optiske målinger og teoretisk modellering.

For at undersøge vekselvirkningen mellem lys og stof, er plasmoniske mellemrumsbølgeledere samt prøver til at studere kvantepunkter nær et halvleder-luft og et halvleder-metal grænselag blevet fremstillet.

Vi har målt henfaldsdynamikken af kvantepunkter nær de plasmoniske mellemrumsbølgeledere hvorved vi observerede modificerede henfaldsrater. Vi udregner at den opnåelige modifikation med de fremstillede strukturer er for lille til at tillade effektive plasmonbaserede enkeltfotonkilder. Teoretiske studier af koblings- og propageringsegenskaberne af plasmoniske bølgeledere afslører at det høje brydningsindeks af materialet der omgiver lyskilden, for eksempel $n_{\mathrm{GaAs}} = 3.5$, begrænser mulighederne for realiseringen af effektive plasmonbaserede enkeltfotonkilder som inkorporerer selvsamlede kvantepunkter.

Den målte henfaldsdynamik af kvantepunkter i nærhed af halvleder-metal grænselag viser at dipol-approksimationen generelt ikke er opfyldt for kvantepunkter grundet deres mesoskopiske størrelse. For at beskrive disse observationer, udvikler vi en teoretisk model for den spontane lysudsendelsen af mesoskopiske kvante lyskilder. Vekselvirkningen mellem lys og stof er i denne model modificeret udover forventningen for en dipol-lysudsender og resulterer i både undertrykkelse og forstærkning af koblingen til plasmoniske tilstande i god overensstemmelse med vores målinger.

Vi påviser at den mesoskopiske effekt kan blive brugt til at modificere koplingen til plasmoniske tilstande på metal- nanotråde og mellemrumsbølgeledere kraftigt, og foreslår at denne effekt generelt bruges til at kontrollere spontant henfald udover dipol-approksimationen i nano-strukturerede omgivelser.

# List of publications

The work carried out during this Ph.D.-project has resulted in the publications listed below.

### Journal publications

1. M. L. Andersen, S. Stobbe, A. S. Sørensen and P. Lodahl, *Strongly modified plasmon-matter interaction with mesoscopic quantum emitters*, to be published in Nature Physics (*http://dx.doi.org/10.1038/NPHYS1870*)

### Journal publications in preparation

1. M. L. Andersen, S. Ates and P. Lodahl, *InAs quantum dots coupled to plamonic nano-gap waveguides*, work in progress.

2. M. L. Andersen, S. Stobbe, A. S. Sørensen and P. Lodahl, *Light emission from mesoscopic quantum dots*, in preparation

### Conference contributions

1. M. L. Andersen, S. Stobbe, J. Johansen and P. Lodahl, *Coupling of self-assembled InAs quantum dots to surface plasmon polaritons*, CLEO/QELS, San Jose, USA (2008).

2. M. L. Andersen, S. Stobbe, J. Johansen and P. Lodahl, *Coupling of self-assembled InAs quantum dots to surface plasmon polaritons*, Dansk Fysisk Selskabs Årsmøde, Nyborg, Denmark (2008).

### Popular articles

1. P. L. Hansen, M. L. Andersen, M. van der Poel and J. Mørk, *Nanofotonik : Nanofotonik kaster lys over fremtiden*, in **Nanoteknologiske Horisonter**, p. 144-159, DTU (2008).

# Contents

# Chapter 1

# Introduction

During the twentieth century, quantum optics of atoms have been a tremendously successful field of research. Early breakthroughs include the formulation of the wave-particle duality and the quantization of the light field [1, 2]. A consequence of this quantization is that the vacuum light-field exhibits fluctuations around its mean zero amplitude. These fluctuations are essential to explain the Lamb shift [3], spontaneous emission [4], and the Casimir effect [5], to name only a few experimentally verified, important physical phenomenons. On the other hand, quantum optics provide a powerful tool to experimentally investigate fundamental issues such as hidden variables and non-locality that are of interest to physicist and philosopher alike [6, 7, 8]. Presently, the seemingly non-local interactions are well-understood as entangled states, which have been experimentally realized, and even used for teleportation of quantum information between light and matter in numerous ways [9, 10, 11, 12].

The quantum theory of solids was well-established when the invention of the electronic transistor and integrated circuits paved the way for modern computer technology. The invention of techniques for crystal growth made the fabrication of epitaxial semiconductor hetero-structures possible. These new techniques, combined with the planar technology of integrated circuits made new structures and devices that combine optics and electronics realizable, notably: Lasers, photo-diodes, and solar cells. Recently, the merging of the two research fields of quantum optics and solid state physics has grown to such size and importance that it deserves a name of its own: Solid state quantum optics.

This field is receiving considerable attention due to the prospects of engineering optical systems at the nanometer length scale. Solid state quantum optics is a subfield of the broader field *photonics*, whose name emphasizes the expectancy that photonic circuits will overtake many of the roles of present day electronic circuits.

With the invention of quantum computing [13] and quantum cryptography [14] the need for the controlled interaction between single quantum emitters and single quanta of light arose [15]. For this, self-assembled semiconductor quantum dots provide an essential link as they possess an atom-like discrete electronic transition spectrum while, at the same time, their hosting wafers benefit directly from semiconductor fabrication techniques. Thus, the building blocks for investigating light-matter interaction are available in an environment that may be integrated monolithically into existing photonic devices. The light-matter interaction with a quantum dot can be strongly enhanced by defining an optical cavity around it [4]. Over the past decades there has been tremendous progress in manipulating single quantum dot excitation and single photons in such cavity systems. However, despite spectacular theoretical and experimental progress in cavity quantum-electro-dynamics [16], these systems remain technically challenging and difficult to scale.

It is thus tempting to ask whether alternative physical systems and phenomena can be realized to procure strong and coherent light-matter coupling. Fortunately, many promising candidate systems exist: Plasmonic systems [17] and photonic crystals [18] are among those that are being actively studied for their potential to manipulate the light-matter interaction.

In this work, the coupling of quantum emitters to plasmonic waveguides is investigated. The plasmonic modes of cylindrical nanowires can very efficiently harvest the decay of a nearby excited emitter [19] and even realize a single-photon transistor [20]. Thus the potential of coupling quantum emitters to guided plasmonic modes seems promising. We investigate the potential for developing plasmon-based single-photon sources in an all-solid-state system employing quantum dots as the light source. To this end, we fabricate nanoscale plasmonic waveguides, measure the coupling to these of single quantum dots, compare the results to theory, and theoretically investigate the feasibility of utilizing these systems to realize very efficient light-matter coupling.

Traditionally, the decay rate of an emitter is proportional to its intrinsic

dipole moment and to the local density of optical states, as expressed in Fermi's golden rule [21]. This formalism is utilized in optical cavities, plasmonic systems, and photonic crystals, that provide strongly modified local densities of optical states, to enhance or suppress the light-matter interaction. However, it is to this end equally important to investigate the intrinsic properties of the emitters that also determine the interaction. In this work, we realize that one of the most commonly used approximations in atomic and solid state quantum optics, namely the dipole approximation, does not hold for quantum dots in general. This relies simply on the fact that the optical fields change over the spatial extension of the quantum dots. Consequently, we develop a theory for the decay rates of quantum emitters beyond the dipole approximation. In this theory the decay rate is also determined by the light-field gradients and an additional intrinsic property of the emitters: their mesoscopic moment.

Detailed comparisons between theory and experiments become increasingly rare as both disciplines grow more and more complex. A strong spatial dependence of the local density of optical states combined with an uncontrolled in-plane position of the self-assembled quantum dots, make it impossible to conclude whether a change in the decay rate is due to the emitter or its environment. We therefore employ the simplest nano-structure imaginable, an interface between the host medium for the quantum dots and silver, to unambiguously disprove the validity of the dipole approximation for self-assembled quantum dots and compare the measurements directly to the theory for mesoscopic emitters discussed above. In the interface structure the local density of optical states is only dependent on the distance to the interface which is well-controlled, wherefore it becomes possible to separate effect of the environment from those of the emitter.

These investigations are of great interest for both fundamental science and technology. The efficiency of photo-diodes, semiconductor lasers, solar cells, and single-photon sources rely on strong light-matter interaction and consequently novel decay mechanisms that enhance the interaction would be beneficial to these systems.

The outline of this thesis is as follows:

In Chapter 2 the foundation of this thesis is introduced: quantum dots, light-matter interaction, and surface plasmon polaritons. The chapter aims at introducing fundamental concepts and relations that will be used throughout

this thesis.

Quantum dots are spatially extended entities but are rarely treated as anything but point-sources of light. In Chapter 3 we develop a model for the decay dynamics of extended emitters through a Taylor expansion of the light-field modes. The inclusion of the light-field gradients gives rise to a mesoscopic moment of the quantum dots. We find that the mesoscopic moment contributes to the decay dynamics on the ground state transition due to the broken symmetry of the quantum dots along the growth direction. The mesoscopic moment provides a convenient parameter to describe the complicated interaction between extended emitters and spatially varying light fields.

In Chapter 4 we experimentally investigate the decay dynamics of quantum dots near a silver mirror, i.e., near a semiconductor/metal interface. Our experimental investigations allow us to demonstrate that the dipole approximation breaks down for quantum dots, and we can extract the value of the mesoscopic moment in correspondence with the theory introduced in Chapter 3. We find that especially the coupling to the plasmonic modes at the silver mirror is deviating from a point-dipole description. Furthermore, we calculate the decay dynamics near a nanowire and find that mesoscopic moments strongly modify the coupling to plasmonic modes on the wire.

Chapter 5 presents the fabrication of nano-scale plasmonic waveguides. In this chapter a discussion of the coupling mechanism between an emitter and plasmonic waveguides reveals that plasmonic gap waveguides are well-suited structures for coupling to quantum dots. We present our fabrication recipe for such plasmonic gap waveguides, and show our fabricated structures. The chapter also features an experimental investigation of the coupling of single quantum dots to these plasmonic gap waveguides and a comparison to theory.

The properties of surface plasmons on nano-structures are determined by both the material parameters and the size and shape of the metallic structures. The scaling of various relevant parameters with material composition and waveguide geometry is investigated in Chapter 6, with the aim of determining good candidate structures for plasmon-based single-photon sources.

Finally, our conclusions are presented in Chapter 7.

# Chapter 2

# Quantum dots and their interaction with light

In this chapter, the foundations upon which the rest of this thesis builds are presented. First, we will discuss the electronic and optical properties of quantum dots, which are the central light-sources of this thesis. As we will see in Chapter 3 and Chapter 4, we can use the controlled interaction of quantum dots with a light field to probe the internal properties of quantum dots and *viceversa*.

After introducing quantum dots, we discuss the rich dynamics that arise when emitters are interacting with a light field. A fully quantum mechanical treatment is a necessity to understand and describe the light-matter interaction of the systems considered in this thesis. Despite these very academic roots, light-matter interaction lies at the heart of one of the most successful new technologies of the last century, namely the laser. In a laser, excited states are stimulated to emit photons that are co-propagating and in-phase with the stimulating photons. Here we will be concerned with the spontaneous emission of photons, where there are no stimulating photons, but rather a field of virtual photonic states. Light-matter interaction is very interesting, both due to the fundamental physical insights obtainable as well as due to the technological possibilities it enables. Specifically, controlling the light-matter interaction, which determines the spontaneous emission of an emitter, is the essence of a range of scientific fields and also of this thesis.

In the last part of this chapter, we will discuss the polariton modes that can exist when metals and dielectric materials are brought together. These, so-called, surface plasmon polaritons can be confined below the diffraction limit of light in bulk materials, and have been used to achieve sub-wavelength guiding of light [22], to enhance the light-matter interaction with an emitter [19], as well as in a range of sensing applications [23]. Thus, this chapter will introduce the three major themes of this thesis: quantum dots, light-matter interaction and surface plasmon polaritons.

## 2.1 Electronic- and optical properties of self-assembled InAs quantum dots

Throughout this thesis we will study the interaction of nanoscale clusters of InAs embedded in GaAs, which are fabricated by self-assembly. We will denote these structures simply *quantum dots* even though there is some ambiguity as to which material system the term *quantum dot* refers.

The notation *quantum dots* has been used to refer to core-shell structures of CdSe and ZnS [24], to monolayer fluctuations in quantum well thicknesses [25], to electrically induced confining potentials [26], and to self-assembled clusters of different material combinations from the third and fifth group of elements, or from the second and sixth group [27]. In this thesis we investigate quantum dots made up of InAs in GaAs which are composed of elements from the third and fifth group.

Indium-arsenide quantum dots, which are the subject of this thesis, have been demonstrated to exhibit excellent single-photon emission [28] and to have a high quantum-efficiency [29]. Quantum dots offer atom-like quantized states with emission energies that can be engineered. Furthermore, they are nanoscale sized and can be positioned in three dimensions [30] within a host semiconductor material. The quantum dot containing wafers can be processed using mature semiconductor processing methods, which enables the realization of advanced structures around the quantum dots.

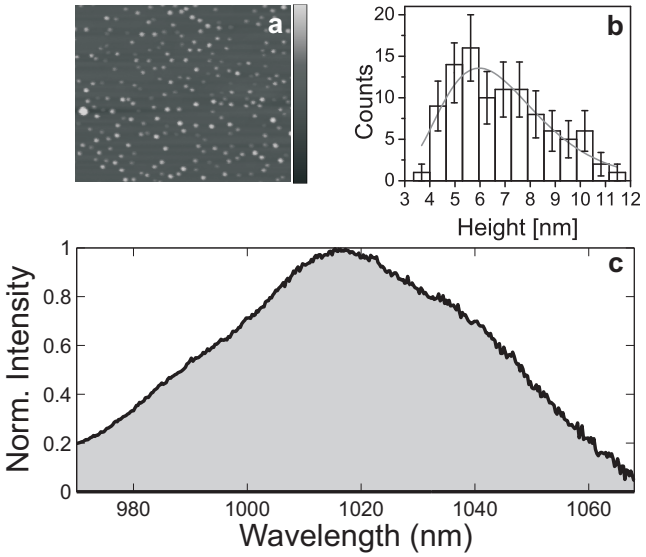


*Figure 2.1: Inhomogeneous distributions of quantum dots.* **a**, *Atomic force micrograph of an uncapped surface of quantum dots.* **b**, *Histogram of the height distribution of the uncapped quantum dots.* **c**, *Spontaneous emission spectrum from a wafer containing quantum dots, the inhomogenously broadened spectrum is due to the size-distribution of the quantum dots.* **a, b** *are from Ref. [31],* **c** *is from the experiment described in Chapter 4.*

### 2.1.1 Formation of self-assembled quantum dots

The quantum dots are grown by molecular beam epitaxy using the Stranski-Krastanov process [32]. First, a GaAs substrate is grown, crystal layer by crystal layer. Hereafter, a few monolayers of InAs are deposited onto the GaAs crystal. InAs and GaAs have the same zincblende crystal structure but slightly different lattice constants, 0.606 nm and 0.565 nm, respectively [33]. The energy associated with the strain induced by the lattice mismatch, will grow for each deposited InAs layer, until it becomes energetically favorable to release the strain through the formation of InAs islands. Under proper growth conditions the resulting structure contains islands of InAs (quantum dots) on top of a few monolayers of strained InAs (wetting layer). After this step, the structure is overgrown with GaAs to complete the three-dimensional confinement potential.

The self-assembly process results in quantum dots with slightly varying spatial dimensions, and thus different quantization energies. A layer of quantum dots can be left uncapped at the top of the wafer, which allows a direct measurement of their sizes by atomic force microscopy, see Fig. 2.1a. We note that the distribution of quantum dot heights obtained in this way, see Fig. 2.1b, is different to those of the capped quantum dots, as the material redistributes itself during overgrowth. The spectrum of an ensemble of quantum dots is inhomogenously broadened due to the size distribution of the quantum dots, see Fig. 2.1c. We note that material redistribution during growth and the presence of strain throughout the quantum dot makes detailed calculation of quantum dot properties a big challenge, since it essentially requires knowledge of the nano-structured composition as well as modeling the interaction between the tens of thousands of constituting particles. In Chapter 4 we extract effective quantum dot properties (dipole and mesoscopic moment) that account for some of these microscopic interactions.

### 2.1.2 Energy states and excitons in quantum dots

Quantum dots are made up of semiconductor crystals. We therefore begin this section with a discussion of the electronic properties of such crystals. This electronic structure is determined by the electrostatic potential defined by the atomic crystal lattice. The periodicity and symmetry of the lattice, give rise to a band structure that describes the dispersion for electrons propagating in the crystal. Semiconductors are defined by a gap between the highest occupied electron band (the valence band) and the lowest unoccupied electron band (the conduction band) at a temperature of 0 K - this gap is known as the bandgap, as shown in Fig. 2.2.

In a direct bandgap semiconductor, e.g. InAs or GaAs, the state of lowest energy in the conduction band and highest energy in the valence band are both found at the $\Gamma$-point in the reciprocal lattice corresponding to an electron wavevector of zero ($\mathbf{k} = 0$). The shape of the two bands can be approximated as parabolic around these extrema [34], which results in a electron-dispersion that is similar to a free-space electron except for a different effective mass as determined by the curvature of the parabola, see Fig. 2.2. This is known as the effective mass approximation [35]. When an electron is excited from the valence band to the conduction band it leaves a hole which can be interpreted

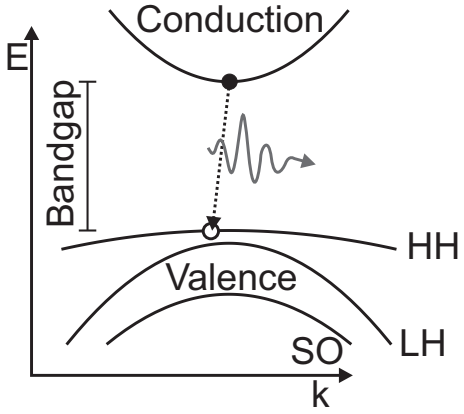


*Figure 2.2: Bandstructure of InAs in a quantum dot, sketched as energy versus crystal momentum. The split-off (SO) and light-hole (LH) band are not degenerate with the heavy-hole (HH) band at zero electron momentum (band extremas, Γ-point), due to spin-orbit coupling and strain, respectively. A bandgap exist between the least energetic conduction band state and the most energetic valence band state. An electron undergoing a transition from the conduction to the heavy-hole band must compensate for the resulting photon momentum, here exaggerated for clarity (slanted dotted line).*

as a positively charged particle with a different effective mass. In contrast to electrons in the conduction band, the finite angular momentum of electrons in the valence band leads to three bands that are degenerate at $\mathbf{k} = 0$, three bands termed split-off, light-hole, and heavy-hole are present as shown in Fig. 2.2. The degeneracy is, however, lifted in quantum dots due to interactions with the crystal. The split-off band is permanently shifted towards lower energies (also in bulk) due to spin-orbit coupling and is therefore not considered in the present work, see Fig. 2.2. The light- and heavy-hole occupy states with different angular momentums and different effective electron masses. Strain, induced by the quantum dot growth, lifts the degeneracy and results in the heavy-hole band being the valence band with the highest energy, and thus the only band relevant for this study. The momentum of a photon is much smaller than the momentum of an electron. The direct bandgap, therefore, allows the semiconductor to be optically active, as momentum conservation can easily be fulfilled when an electron and a hole recombine by emitting a photon, see

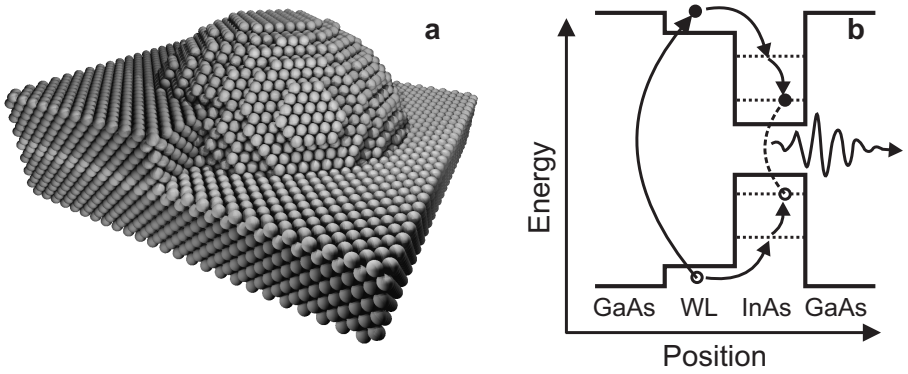


*Figure 2.3: Quantum dots as emitters of single photons.* **a**, *Sketch of a single quantum dot sitting on top of a wetting layer. Illustration from Ref. [36].* **b**, *Electronic structure of a quantum dot. Sketch of the energy of the valence and conduction band as function of position along the growth direction (solid lines). The quantized energy levels of a quantum dot are shown as dotted lines. A laser is tuned to the energy difference between the bands in the wetting layer (WL), which promotes an electron to the conduction band thereby creating a hole. Electron and hole relax to the lowest energy quantum dot state, from where they recombine through the emission of a photon.*

Fig. 2.2.

The bandgap of InAs is smaller than of GaAs, see Fig. 2.3. This results in a confining potential for electrons and holes in quantum dots. Furthermore, due to the nanoscale dimensions of the quantum dots ($\sim 20$ nm $\times$ 20 nm $\times$ 6 nm), the confinement leads to quantized energy levels for the trapped electrons and holes. An excited quantum dot consists of an electron promoted to the conduction band and a hole in the valence band, that together constitute an exciton. Thus, excited quantum dots can emit photons with well-defined energies. Excitons in bulk semiconductors are bound together by Coulomb interaction, but these binding energies are negligible compared to the quantization energies in quantum dots. The quantum dots are therefore referred to as being in the strong confinement regime, where exciton binding energies are neglected.

Depending on the size of the quantum dots, the energy and number of confined exciton states can vary. For weakly excited quantum dots, i.e. $\sim 0.1$ exciton per quantum dot per excitation pulse, only emission from the ground

state transition is typically observed. If electrons and holes occupy more energetic states, they decay to the empty ground state faster than they can decay through a radiative process, as shown in Fig. 2.3. The ground state exciton consists of an electron in the conduction band and a hole in the heavy-hole valence band. These single particle states have angular momentum $J = 1/2$ and $J = 3/2$ [37], respectively, both with a two-fold degeneracy due to spin. By considering the four possible combinations of electrons and holes, we see that the total angular momentum of the exciton is either $\pm 1$ or $\pm 2$. Photons posses an angular momentum of $\pm 1$, thus only excitons with unity angular momentum can couple to photons. Consequently, the excitons with angular momentum $\pm 1$ are called bright excitons and have the spin of electron and hole pointing in opposite directions. Excitons with angular momentum $\pm 2$ are called dark excitons and have the electron and hole spin pointing in the same direction. Dark excitons only decay non-radiatively or through a spin-flip to a bright state [38].

### 2.1.3 Decay dynamics of quantum dots

Excited quantum dots will decay to their ground state after some characteristic lifetime. In this section we describe this decay dynamics of quantum dots modeled as a multi-level system. Quantum dots are often modeled as ideal two-level systems coupled to the electromagnetic field vacuum state, for which the decay dynamics is a simple single-exponential decay. Real quantum dots, however, are more complex, and resultantly so are their decay dynamics as shown in Fig. 2.4. The measured non-single-exponential decay dynamics stem from the fine-structure of the exciton ground state. Both dark and bright excitons ground states are populated when quantum dots are excited non-resonantly.

The two excited states (dark and bright) are split in energy by exchange interaction [32], leading to the bright state being displaced $\sim 150$ μeV [32] above the dark exciton level. Furthermore, the dark and bright state themselves are split due to the broken rotational symmetry around the growth axis of the quantum dot [39]. However, the essential decay dynamics of the quantum dot can be captured by assuming a three-level system of exciton-states: dark $|d\rangle$, bright $|b\rangle$, and ground $|g\rangle$ as shown in Fig. 2.4b. The populations of the dark and bright energy levels are coupled via spin-flip rates, as a single

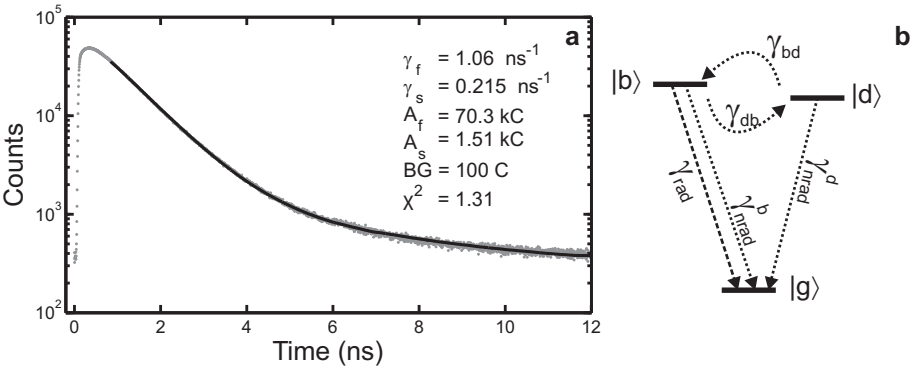


*Figure 2.4: Decay of an excited quantum dot.* **a**, *Decay curve from an sub-ensemble of quantum dots emitting at* 1030 nm *constructed as a histogram of emission times of single photons in relation to the excitation pulse. The data-points are fitted with a bi-exponential model (black line) and the fitting parameters are given within the figure.* **b**, *Three-level model of a quantum dot, the presence of a coupling rate between the dark and bright state leads to the bi-exponential decay shown in* **a**.

spin-flip of either electron or hole transforms a dark exciton to a bright, $\gamma_{db}$, or *viceversa*, $\gamma_{bd}$. Furthermore, a non-radiative decay of both dark, $\gamma^d_{nrad}$, and bright, $\gamma^d_{nrad}$, excitons take place, and the bright exciton can additionally decay with a radiative rate $\gamma_{rad}$ to the ground state whereas the dark exciton cannot.

The intensity of emitted photons as function of time from the initial excitation of a quantum dot is proportional to the constant rate of radiative coupling $\gamma_{\mathrm{rad}}$ and to the time-varying population of the bright state $\rho_b(t)$,

$$I(t) \propto \gamma_{\mathrm{rad}} \rho_b(t). \tag{2.1}$$

The time-evolution of the bright state can be understood by the three-level model presented above, and with this model we can fit the measured decay dynamics. Assuming that the spin-flip rates are slow compared to both the radiative and non-radiative decay rates, the population of the bright state decays as a bi-exponential function over time with two decay rates given as [38]

$$\gamma_f = \gamma_{\mathrm{rad}} + \gamma^b_{\mathrm{nrad}} + \gamma_{bd} \approx \gamma_{\mathrm{rad}} + \gamma^b_{\mathrm{nrad}} \tag{2.2}$$

$$\gamma_s = \gamma^d_{\mathrm{nrad}} + \gamma_{db} \approx \gamma^d_{\mathrm{nrad}}. \tag{2.3}$$

where $\gamma_f$ and $\gamma_s$ is the fast and slow decay rate respectively. The form of the measured decay curve given as intensity over time is bi-exponential

$$I(t) \propto A_f e^{-\gamma_f t} + A_s e^{-\gamma_s t} + BG, \tag{2.4}$$

with $A_f$ and $A_s$ as the amplitude of the fast and slow component, respectively, and $BG$ denotes the experimentally unavoidable background which is independent of time. In Fig. 2.4a the decay curve is fitted to a bi-exponential model which is in very good agreement with the measured data.

In this thesis we will focus on the ground-state bright-exciton, and treat the quantum dot as a two-level system with the excited state being the ground-state bright-exciton and the ground state being the unoccupied quantum dot. The decay rate of the excited state is given by $\gamma_f$ and is extracted from decay data as the fast rate of a bi-exponential fit as discussed above.

## 2.2 Light-matter interaction

The light-matter interaction of a dipole emitter with an optical environment describes the working mechanism in light-emitting diodes, solar cells, and lasers as well as the exciting regime of strong coupling where the light and matter degrees of freedom are intertwined. Here, we will introduce the interaction of a dipole emitter with a vacuum field. A detailed calculation of the light-matter interaction beyond the dipole-approximation is presented in Chapter 3, in which the interaction of a simple dipole emitter occurs as a special case. Therefore, we will only give a phenomenological discussion of the light-matter interaction here. We also introduce in detail the dyadic Green's function formalism and several characterization methods of decay dynamics in structured and homogeneous media.

### 2.2.1 Spontaneous emission

Spontaneous emission is the process in which an emitter in an excited state spontaneously decays to a state of lower energy by emitting a photon that carries the surplus energy. With a semi-classical model of light-matter interaction, where only the emitter is quantized, spontaneous emission cannot be explained and must be introduced phenomenologically [21]. Thus, a full quantum me-

chanical model where both emitter and light field are quantized is needed to give the correct description of spontaneous emission.

The quantization of the light field leads to a non-zero variance of the electromagnetic field, even for the vacuum field, which is in contrast to the classical description where the vacuum field is identically zero. The vacuum fluctuations of the quantum mechanical electromagnetic field have been depicted as virtual photons. Virtual photons can exist in brief moments of time as allowed by the uncertainty relations in quantum mechanics. In this picture, the virtual photons stimulate the excited emitter to 'spontaneously' emit a real photon.

The rate of spontaneous emission was believed to be an intrinsic property of the emitter, until the work of Purcell in 1946 [4]. E. M. Purcell found that the rate of emission from an emitter in a cavity was enhanced, when the cavity was in resonance with the emitter. The emission rate was enhanced with a factor $F^P = \frac{3Q\lambda^2}{4\pi^2 V_c}$, where $Q$ is the quality factor of the cavity and $V_c$ the mode volume - today $F^P$ is known as the Purcell factor. In 1970, K. H. Drexhage [40] found that the rate of spontaneous emission could be both enhanced and suppressed when the distance to a reflecting surface was varied. The observed modifications in the decay rate were more moderate than in a cavity in this case, but revealed that the effect does not rely on a resonance. Since then, emitters have been placed in cavities which have very small mode volumes and very high quality factors, leading to the strong-coupling regime [41], where the atomic and field population are intertwined. Strong suppression of the decay rate has been predicted in three-dimensional photonic crystals which can be made to have an optical bandgap. Emitters with an emission-frequency in the optical band-gap, placed within such a structure, have been experimentally confirmed to reveal a suppressed decay rate [42]. Generally, the emission rate of a dipole emitter in a dielectric environment can be written as (derived in Chapter 3)

$$\Gamma(\mathbf{r}_0, \omega) = \frac{2q^2}{m^2 c^2 \epsilon_0 \hbar} \mu_{j'}^{if} \mu_j^{fi} \mathrm{Im}(G_{j,j'}(\mathbf{r}_0, \mathbf{r}_0; \omega)), \tag{2.5}$$

where $q$ and $m$ are the charge and mass of the particle undergoing a transition. $\mu_j^{fi} = \langle f|\hat{p}_j|i\rangle$ is the naturally occurring dipole moment in the $\hat{\mathbf{p}} \cdot \mathbf{A}$ Hamiltonian formalism, which describes the transition from the initial, $|i\rangle$, to the final, $|f\rangle$, electronic state, with $\hat{p}_j$ being the momentum operator along the $j$th axis ($j,\ j' \in \{x, y, z\}$) (we do not explicitly write the sum over repeated coordinates indices). This moment is related to the usual transition dipole moment

$d_j^{fi} = q\langle f|r_j|i\rangle$ through $\mu_j^{fi} = i\frac{m\omega_0}{q}d_j^{fi}$, by using $\mathbf{p} = -m\frac{i}{\hbar}[\mathbf{r}, H_0]$ [43], where $H_0$ is the unperturbed Hamiltonian of the system and the brackets $[,]$ denote a commutator. We will in this thesis use both $\mu_j$ and $d_j$ to describe a point-dipole. We will use $\mu_j$ predominantly, but also use $d_j$ when discussing equations that are often expressed in this way in the literature. The electromagnetic environment is described by the dyadic Green's function tensor $G_{j,j'}(\mathbf{r}_0, \mathbf{r}_0; \omega)$, the definition of which we will give below. In terms of the dyadic Green's tensor the projected local density of optical states is given by

$$\rho(\mathbf{r}_0, \omega, \mathbf{e}_\mu) = \frac{2\omega}{\pi c^2}\left[\mathbf{e}_{\mu,j} \cdot \mathrm{Im}(G_{j,j'}(\mathbf{r}_0, \mathbf{r}_0; \omega)) \cdot \mathbf{e}_{\mu,j'}\right], \tag{2.6}$$

which defines the density of states seen by a dipole emitter that is positioned at $\mathbf{r}_0$, oscillating at the frequency $\omega$, and where $\mathbf{e}_{\mu,j}$ is the $j$'th component of its dipole moment unit vector. Comparing Eq. (2.5) and Eq. (2.6), we find that the decay rate is proportional to the local density of optical states and the size of the dipole moment, in agreement with Fermi's golden rule [21]. The local density of optical states provides the framework to understand the position dependent decay dynamics of emitters in structured media. $\rho(\mathbf{r}_0, \omega, \mathbf{e}_\mu)$ is explicitly dependent on position, in contrast to the density of optical states used to describe homogeneous media. The position dependence of the local density of states implies that the environment of an emitter can be engineered to control its decay dynamics.

### 2.2.2 Electromagnetism in structured media

Maxwell's equations lie at the starting point of any study involving electromagnetic fields. These are, for the case of a non-magnetic and charge- and current-free environment, given by [44]:

$$\nabla \cdot \mathbf{D} = 0, \tag{2.7a}$$

$$\nabla \cdot \mathbf{B} = 0, \tag{2.7b}$$

$$\nabla \times \mathbf{E} = -\frac{\partial \mathbf{B}}{\partial t}, \tag{2.7c}$$

$$\nabla \times \mathbf{H} = +\frac{\partial \mathbf{D}}{\partial t}. \tag{2.7d}$$

$\mathbf{B}$ and $\mathbf{E}$ are the magnetic induction and electric field, respectively, while $\mathbf{H}$ and $\mathbf{D}$ are the magnetic field and electric displacement. The fields are further

bound together through the relations

$$\mathbf{D} = \epsilon_0 \mathbf{E} + \mathbf{P} = \epsilon_0 \epsilon_r \mathbf{E}, \tag{2.8}$$

$$\mathbf{B} = \mu_0 \mathbf{H}, \tag{2.9}$$

where $\epsilon_0$ and $\mu_0$ are the vacuum permittivity and permeability, respectively, and $\epsilon_r$ is the relative permittivity. In a non-magnetic medium the relative permittivity and refractive index, $n$, are related through $n^2 = \epsilon_r$. In Eq. (2.8), $\mathbf{P}$ is the intrinsic polarization of the medium which occur in response to the electric field.

Combining the Maxwell's equations Eq. (2.7c) and Eq. (2.7d) with the field relations Eq. (2.8) and Eq. (2.9), we can write up the wave equation for the electric field:

$$\nabla \times \nabla \times \mathbf{E}(\mathbf{r}, t) + \frac{\epsilon_r(\mathbf{r})}{c^2} \frac{\partial^2}{\partial t^2} \mathbf{E}(\mathbf{r}, t) = 0, \tag{2.10}$$

where we have used that $\epsilon_0 \mu_0 = c^{-2}$. This equation gives rise to the harmonic time dependence of the electrical field

$$\mathbf{E}(\mathbf{r}, t) = \mathbf{E}(\mathbf{r}) e^{-i\omega t}. \tag{2.11}$$

Furthermore, the spatial dependence of the electric field must satisfy the Helmholtz equation

$$\nabla \times \nabla \times \mathbf{E}(\mathbf{r}) - \epsilon_r(\mathbf{r}) \frac{\omega^2}{c^2} \mathbf{E}(\mathbf{r}) = 0, \tag{2.12}$$

in the inhomogeneous dielectric environment given by $\epsilon_r(\mathbf{r})$. Equation (2.12) constitutes an eigenvalue equation with eigenmodes $\mathbf{f}_l(\mathbf{r})$, corresponding to an angular frequency $\omega = \omega_l$, that satisfy the normalization condition

$$\int d\mathbf{r} \epsilon_r(\mathbf{r}) \mathbf{f}_l^*(\mathbf{r}) \mathbf{f}_m^*(\mathbf{r}) = \delta_{l,m}, \tag{2.13}$$

onto which any solution $\mathbf{E}(\mathbf{r})$ to the Helmholtz equation, i.e. Eq. (2.12), can be expanded.

### 2.2.3 Dyadic Green's function formalism

We wish to calculate the resulting electric field in a structured media resulting from an extrinsic polarization $\mathbf{P}_{\text{ex}}(\mathbf{r}, t)$. In this case we can write the wave equation as

$$\nabla \times \nabla \times \mathbf{E}(\mathbf{r}, t) = -\frac{\partial^2}{\partial t^2} \mu_0 \left( \epsilon_0 \epsilon_r(\mathbf{r}) \mathbf{E}(\mathbf{r}, t) + \mathbf{P}_{\text{ex}}(\mathbf{r}, t) \right). \tag{2.14}$$

The corresponding result in the frequency domain is

$$\nabla \times \nabla \times \mathbf{E}(\mathbf{r},\omega) - \epsilon_r(\mathbf{r})\frac{\omega^2}{c^2}\mathbf{E}(\mathbf{r},\omega) = \frac{\omega^2}{\epsilon_0 c^2}\mathbf{P}_{\text{ex}}(\mathbf{r},\omega), \tag{2.15}$$

where the extrinsic polarization field is driving the electric field. In this case the electrical field can be calculated as [45]

$$\mathbf{E}(\mathbf{r},\omega) = \frac{\omega^2}{\epsilon_0 c^2}\int d\mathbf{r}'\mathbf{G}(\mathbf{r},\mathbf{r}';\omega)\mathbf{P}_{\text{ex}}(\mathbf{r}',\omega), \tag{2.16}$$

where $\mathbf{G}(\mathbf{r},\mathbf{r}';\omega)$ is the dyadic Green's function for the system. The dyadic Green's function is the solution to the equation

$$\nabla \times \nabla \times \mathbf{G}(\mathbf{r},\mathbf{r}';\omega) - \epsilon_r(\mathbf{r})\frac{\omega^2}{c^2}\mathbf{G}(\mathbf{r},\mathbf{r}';\omega) = \mathbf{I}\delta(\mathbf{r},\mathbf{r}'), \tag{2.17}$$

where $\mathbf{I}$ is the identity tensor. The strength of the dyadic Green's function approach is that for a given environment, determined by $\epsilon_r(\mathbf{r})$, it is straightforward to calculate the electric field originating from an arbitrary driving extrinsic polarization once the dyadic Green's function is known.

In the special case of a dipole emitter situated at $\mathbf{r}_0$, $\mathbf{P}_{\text{ex}}(\mathbf{r}',\omega) = \boldsymbol{\mu}(\omega)\delta(\mathbf{r_0}-\mathbf{r}')$, we find

$$\mathbf{E}(\mathbf{r},\omega) = \frac{\omega^2}{\epsilon_0 c^2}\mathbf{G}(\mathbf{r},\mathbf{r}_0;\omega)\mathbf{d}(\omega), \tag{2.18}$$

from which it becomes clear that we can interpret the dyadic Green's function as a propagator for the electric field in an environment $\epsilon_r(\mathbf{r})$, i.e. it gives the electric field at $\mathbf{r}$ resulting from a point-dipole at $\mathbf{r}_0$.

Closed expressions for the Green's function exists for a few specific environments, provided that these environment are sufficiently simple. This will be utilized in Chapter 3 and Chapter 4, where the decay dynamics in a slab structure of three different materials are investigated. The Green's function for the slab structure is presented in Appendix A.

### 2.2.4 Decay rates in homogeneous media

The decay rate of an emitter in a homogeneous medium can be evaluated by calculating the dyadic Green's function and using Eq. (2.5). The dyadic Green's function for a homogeneous medium is defined as [45],

$$\mathbf{G}_0(\mathbf{r},\mathbf{r}_0;\omega) = \frac{\exp(ikR)}{4\pi R}\left[\left(1+\frac{ikR-1}{k^2R^2}\right)\mathbf{I} + \frac{3-3ikR-k^2R^2}{k^2R^2}\frac{\mathbf{RR}}{R^2}\right], \tag{2.19}$$

where $R$ is the length of $\mathbf{R} = \mathbf{r} - \mathbf{r}_0$, $\mathbf{RR}$ is the outer product of $\mathbf{R}$ with itself and $k = 2\pi n/\lambda_0$ is the wavenumber with $n$ being the refractive index of the medium. We can expand $\exp(ikR) = 1 + ikR - (1/2)k^2R^2 + \ldots$ and let $R \to 0$ which is the relevant limit for the decay rate of a point-dipole. The imaginary part of the dyadic Green's function is then given as $\mathrm{Im}(\mathbf{G}_0(\mathbf{r}, \mathbf{r}_0; \omega)) = k/(6\pi)\mathbf{I}$, which results in a decay rate in a homogeneous environment using Eq. (2.5) and relating $\mu$ to $d$

$$\Gamma_0 = \frac{n\omega^3|d|^2}{3\pi\epsilon_0\hbar c^3}. \tag{2.20}$$

The decay rate of an emitter in a homogeneous environment thus scales with the cube of the frequency $\omega$ and with the refractive index $n$. Enhancement and suppression of the decay rate of an emitter, refers to deviations from the decay in a homogeneous medium, which as seen above is not a fixed quantity.

### 2.2.5 Decay rates in structured media

The decay rate of an emitter in a structured dielectric is determined by the dyadic Green's function for this. Generally, the dyadic Green's function can be split into a part for the homogeneous medium $\mathbf{G}_0(\mathbf{r}, \mathbf{r}_0; \omega)$ as given above, and a part resulting from the scattering on the environment $\mathbf{G}_s(\mathbf{r}, \mathbf{r}_0; \omega)$.

$$\mathbf{G}(\mathbf{r}, \mathbf{r}_0; \omega) = \mathbf{G}_0(\mathbf{r}, \mathbf{r}_0; \omega) + \mathbf{G}_s(\mathbf{r}, \mathbf{r}_0; \omega) \tag{2.21}$$

The scattering Green's function $\mathbf{G}_s(\mathbf{r}, \mathbf{r}_0; \omega)$ describes the effect of the scattering medium and is generally very difficult to obtain in complex structures. The normalized decay rate, i.e., the decay rate of an emitter in a structured medium divided by the decay rate in a suitable homogeneous medium is given by

$$\frac{\Gamma(\mathbf{r}_0, \omega)}{\Gamma_0(\omega)} = 1 + \frac{6\pi c}{\omega n}\mathrm{Im}(\mathbf{e}_\mu \cdot \mathbf{G}_s(\mathbf{r}_0, \mathbf{r}_0; \omega) \cdot \mathbf{e}_\mu), \tag{2.22}$$

where $\mathbf{e}_\mu$ denotes a unit vector pointing in the direction of the dipole moment. We note that the relative decay rate as given by the scattering part of the dyadic Green's function, is purely a property of the classical Maxwell's equations. An equivalent expression exists for the classical problem of the normalized rate for energy dissipation of a dipole-current [45]. Thus, a classical expression seemingly governs the decay dynamics of a quantum dipole emitter, but one should remember that the classical picture does not provide any explanation for the mechanism of spontaneous decay.

### 2.2.6 Characterization of decay dynamics

The decay of an emitter in a structured medium, can be split into a number of decay channels $\Gamma = \sum_i \gamma_i$, that characterize the emission. As an example we consider the case of an emitter in a cavity. Here, there are three relevant decay mechanisms: decay to the cavity mode $\gamma_{\mathrm{cav}}$, decay to radiation modes that leak out of the cavity $\gamma_{\mathrm{leak}}$, and an intrinsic non-radiative recombination rate of the emitter $\gamma_{\mathrm{nr}}$. To describe the rate of the decay into a specific channel $\gamma_j$ we introduce the Purcell factor [4]

$$F_j^P = \frac{\gamma_j}{\Gamma_0}, \tag{2.23}$$

where $\Gamma_0$ is the decay rate in a homogeneous medium. The Purcell factor characterizes the rate at which a specific decay process occur, and is as such a very important characteristic for applications where it is essential that the decay occurs before the system is destroyed, e.g. photon emission before decoherence for quantum communication.

Another important characteristic is the efficiency with which a specific decay process occurs as given by the $\beta$-factor,

$$\beta_j = \frac{\gamma_j}{\sum_i \gamma_i} = \frac{F_j^P \Gamma_0}{F_j^P \Gamma_0 + \sum_{i \neq j} \gamma_i} \tag{2.24}$$

which is also related to the Purcell factor. The $\beta$-factor gives the probability that the decay goes into the specific channel $j$, and is the most important factor for single-photon on-demand applications. High $\beta$-factors can be achieved by either enhancing the rate of decay into the preferred channel $j$ as given by $F_j^P$, by suppressing the rate of decay into all other channels $\sum_{i \neq j} \gamma_i$, or by a combination of the two. We will use both the Purcell and the $\beta$-factor throughout this thesis to characterize different decay mechanisms.

## 2.3 Surface plasmons

The optical properties of metals are very different from those of dielectrics and are characterized by a complex-valued permittivity $\epsilon_r(\omega)$. In the frequency range of interest to this study it exhibits a negative real part and a small imaginary part. The difference in the optical properties between dielectrics and metals can be understood from their microscopic electron configurations.

The electrons are bound to their host atoms in a dielectric, while there exists a gas of free electrons in a metal.

We begin this section with a short derivation of the optical properties of metals, since most of the physics of the interaction of light with metals is hidden in the frequency dependence of the metal's complex permittivity. We hereafter turn to the solution of Maxwell's equations for a bound mode propagating at the interface between a metal and a dielectric. For these, so-called surface plasmon polaritons, we give expressions for important physical quantities, such as dispersion, confinement-, and propagation length.

### 2.3.1 Optical properties of metals

The optical properties of metals, have been successfully described by Drude in 1900 [46]. This classical approach is sufficient in the present context. The Drude model (which is also known as the free-electron model) assumes a gas of free electrons that moves against a fixed background of positive ions. The electrons are accelerated by a driving electric field and damped by collisions, as given by the rate $\gamma$. The displacement of an electron $\mathbf{x}$ with an effective mass $m$ (resulting from the background potential) is then determined by

$$m\ddot{\mathbf{x}} + m\gamma\dot{\mathbf{x}} = -e\mathbf{E}, \tag{2.25}$$

where $e$ is the elementary charge. Assuming a harmonic time-dependence of the electric field ($\mathbf{E}(t) = \mathbf{E}_0 e^{-i\omega t}$) we can calculate the resulting displacement of the electron. This gives rise to a macroscopic polarization of the medium through $\mathbf{P} = -ne\mathbf{x}$, where $n$ is the density of electrons, that is proportional to the electric field

$$\mathbf{P} = -\frac{ne^2}{m(\omega^2 + i\gamma\omega)}\mathbf{E}. \tag{2.26}$$

Comparing the last expression to Eq. (2.8) we find that the relative permittivity of a metal is given by

$$\epsilon_r(\omega) = 1 - \frac{\omega_p^2}{\omega^2 + i\gamma\omega}. \tag{2.27}$$

We will work in the regime of $\omega < \omega_p$, with $\omega_p = ne^2/\epsilon_0 m$ being the plasma frequency. We will use gold and silver, which have $\gamma \ll \omega_p$. We note that the real part of $\epsilon_r(\omega)$ scales inversely with $\omega^2$ and furthermore that the imaginary part scales in the same way but is smaller by a factor $\gamma/\omega$. In Chapter 6 we will return to the effect of this scaling on the plasmonic mode properties.

### 2.3.2 Surface plasmon polaritons

Surface plasmon polaritons are found as the bound solutions of Helmholtz equation, i.e. Eq. (2.12), at the interface between a metal and a dielectric. We consider the geometry of two semi-infinite media that are connected at the $z = 0$ plane. We use the convention that $\epsilon_r(z > 0) = \epsilon_1$ and $\epsilon_r(z < 0) = \epsilon_2$. Due to the symmetry of the system we write up the following equations in terms of only the $z$-axis and a general in-plane $\rho$-axis. No s-polarized mode that is bound to the interface exists due to electromagnetic boundary conditions [17], we therefore only consider a general p-polarized mode, where the electric field only exists in the propagation direction and perpendicular to the interface

$$\mathbf{E}_j = \begin{pmatrix} E_{j,\parallel} \\ E_{j,z} \end{pmatrix} e^{i(k_\parallel \rho - \omega t)} e^{i k_{j,z} z}, \qquad j = 1, 2. \tag{2.28}$$

The wavevectors in the two half-spaces satisfy

$$k_\parallel^2 + k_{j,z}^2 = \epsilon_j k^2, \qquad j = 1, 2, \tag{2.29}$$

where $k = \omega/c$. Using Eq. (2.7a) in both half-spaces, and requiring continuity [44] of the parallel component of the electric field and the perpendicular component of the displacement field we arrive at

$$k_\parallel E_{j,\parallel} + k_{j,z} E_{j,z} = 0, \qquad j = 1, 2, \tag{2.30a}$$

$$E_{1,\parallel} - E_{2,\parallel} = 0, \tag{2.30b}$$

$$\epsilon_1 E_{1,z} - \epsilon_2 E_{2,z} = 0, \tag{2.30c}$$

which only have a common solution if $(k_\parallel = 0)$ or if $(\epsilon_2 k_{1,z} - \epsilon_1 k_{2,z} = 0)$. The first of these solutions is obviously not a mode propagation on the interface. From the second solution we then find that

$$k_\parallel^2 = \frac{\epsilon_1 \epsilon_2}{\epsilon_1 + \epsilon_2} \frac{\omega^2}{c^2}, \tag{2.31}$$

$$k_{j,z}^2 = \frac{\epsilon_j^2}{\epsilon_1 + \epsilon_2} \frac{\omega^2}{c^2}, \qquad j = 1, 2\ , \tag{2.32}$$

$$\mathbf{E}_j = E_\parallel \begin{pmatrix} 1 \\ -\sqrt{\epsilon_1 \epsilon_2 / \epsilon_j^2} \end{pmatrix} e^{i(k_\parallel \rho - \omega t)} e^{i k_{j,z} z}, \qquad j = 1, 2. \tag{2.33}$$

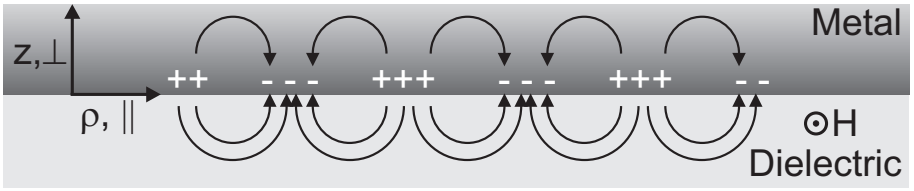


*Figure 2.5: The plasmonic field. For a plasmonic mode propagating from left to right, the electric field is in the plane of the page while the magnetic field $H$ is perpendicular to the page. The electromagnetic field is interacting with charge displacement-oscillations in the metal indicated by the $+$ and $-$ signs. The used coordinate system is defined.*

Using Eq. (2.31)-Eq. (2.33) we can discuss the requirements for the existence of a bound surface mode.

For simplicity we will assume that the imaginary part of the permittivities are negligible. We are looking for a mode that propagate in the plane, which requires that $k_{\|}$ is real. The dispersion for $k_{\|}$, i.e. Eq. (2.31), can be seen to be fulfilled when either, both the product and sum of $\epsilon_1$ and $\epsilon_2$, is negative or positive. Furthermore, we are looking for a bound solution, by which we mean that it should not propagate away from the interface. This is realized when $k_z$ is purely imaginary, which is only achieved when the sum $\epsilon_1 + \epsilon_2$ is negative. We must therefore fulfil both $\epsilon_1 \cdot \epsilon_2 < 0$ and $\epsilon_1 + \epsilon_2 < 0$, which requires that one of the permittivities is negative with an absolute value exceeding that of the other. As we have discussed in the previous section, metals exhibit negative permittivities with small imaginary parts, wherefore surface plasmon polaritons can exist at the interface of a metal and a dielectric as sketched in Fig. 2.5.

### 2.3.3 Properties of surface plasmon polaritons

We will now set the permittivity for the dielectric $\epsilon_1 = \epsilon_d > 0$ to be purely real, and set $\epsilon_2 = \epsilon_m = \epsilon'_m + i\epsilon''_m$ as the complex-valued permittivity for the metal with $\epsilon'_m < -\epsilon_d$ and $|\epsilon'_m| \gg |\epsilon''_m|$. This leads to a complex wavevector

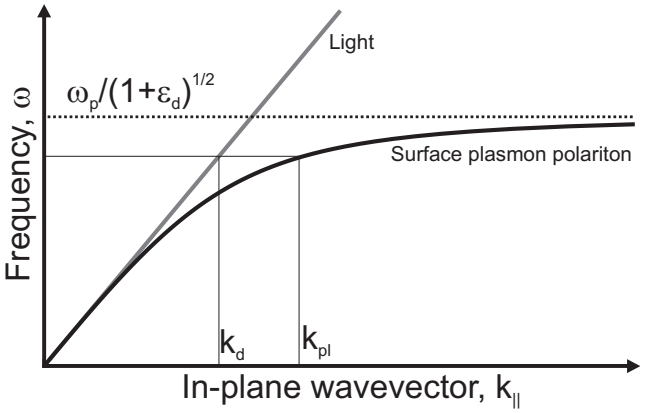


*Figure 2.6: Dispersion of surface plasmon polaritons. The surface plasmon polariton in-plane wavevector (black line) diverges as the frequency approach the resonance condition determined by the plasma frequency of the metal and the permittivity of the dielectric. For low frequencies the surface plasmon polariton approaches the light-line. For a frequency below the resonance, the surface plasmon polariton has a bigger momentum $k_{pl}$ than a photon with the same frequency.*

$k_{||} = k'_{||} + ik''_{||}$ that can be expressed in terms of

$$k'_{||} \approx \frac{\omega}{c}\sqrt{\frac{\epsilon_d \epsilon'_m}{\epsilon_d + \epsilon'_m}}, \tag{2.34}$$

$$k''_{||} \approx \frac{\omega}{c}\left(\frac{\epsilon_d \epsilon'_m}{\epsilon_d + \epsilon'_m}\right)^{3/2} \frac{\epsilon''_m}{2\epsilon'^2_m}, \tag{2.35}$$

where $k''_{||}$ determines the absorption that damps the surface plasmon polariton while it propagates along the interface. The corresponding propagation length, after which the intensity of the surface plasmon polariton field has decayed by a factor $1/e$, is defined as

$$L_{\text{prop.}} = \frac{1}{2k''_{||}}. \tag{2.36}$$

A propagating photon in the dielectric $\epsilon_d$ has a purely real wavevector $k_d = \sqrt{\epsilon_d}\omega/c$ which is smaller than the wavevector at the same frequency for the surface plasmon polariton $k_{\text{pl}} = k_{||}$, as given in Eq. (2.34) and shown in Fig. 2.6. We interpret the larger momentum of the surface plasmon polaritons

as being caused by the extra momentum from the co-oscillating electron wave in the metal. In Fig. 2.6 the full dispersion relation in a lossless metal (with the damping rate $\gamma = 0$) is shown compared to the light-cone for the dielectric. We see that the wavevector diverges as $\omega \to \omega_p/\sqrt{1+\epsilon_d}$, where $\omega_p$ is the bulk plasma frequency discussed above. The divergence is not present in real metals where the damping rate $\gamma \neq 0$.

The wavelength of the plasmonic mode is given by $\lambda_{\mathrm{pl}} = 2\pi/k'_{\parallel}$, and is therefore shorter than that of a free photon. The surface plasmon polariton is confined to propagate along $\rho$ in the $z = 0$ plane, but the electric field is decaying exponentially away from the interface giving rise to a penetration depth into the metal and dielectric, as shown in Fig. 2.5. The penetration depth determines the extension of the surface plasmon polariton. Here, we define the depth where the intensity of the surface plasmon polariton is reduced with a factor $1/e$, which is different for the two materials

$$L_{\mathrm{ext.}} = \frac{1}{2|k_{j,z}|}, \qquad j = 1, 2. \tag{2.37}$$

The extension of the surface plasmon polaritons is very interesting both due to the associated possibility of subwavelength guiding, and imaging of light but also due to the associated field enhancement. There is, however, a trade-off to be considered: The propagation distance decreases when the extension gets smaller. This trade-off is an intrinsic problem of the field of surface plasmon polaritons and will also pose challenges for the work presented later in this thesis.

### 2.3.4 Scalability of Maxwell's equations

Maxwell's equations describe the behavior of electromagnetic modes that span fifteen decades of wavelengths. Thus, an often exploited feature of Maxwell's equations is that a specific physical phenomenon can be studied at different wavelengths. However, the divergence of the surface plasmon polariton is tied to the plasma frequency of the metal, wherefore phenomena that rely on the plasma frequency do not scale with wavelength. In Chapter 5 and Chapter 6 the properties of plasmonic modes in complex geometries are considered, where we study emitters that operate at a frequency well below the plasma resonance condition. The scaling of important physical parameters in this frequency range will be the subject of Chapter 6.

## 2.4 Summary

In this chapter we have introduced the basic electronic and optical properties of quantum dots. In Chapter 3 we will return to these, where quantum dots are treated in great detail as extended asymmetric emitters, with special optical properties as a result. In the brief treatment of the light-matter interaction in this chapter we introduced the Helmholtz equation, dyadic Green's functions, and the general concepts of spontaneous emission and its change in structured environments. Lastly, we introduced surface plasmon polaritons in some detail as these will be a recurring subject throughout this thesis. For the ease of readability, we will use the less stringent notion of *plasmons* interchangeably with *surface plasmon polaritons* in the rest of this thesis.

# Chapter 3

# Quantum dot decay dynamics beyond the dipole approximation

It is the essence of the modern research disciplines plasmonics, photonic crystals, and light harvesting to control the interaction between light and matter in an all-solid-state environment. In contrast to atomic and molecular emitters, solid-state emitters can be positioned deterministically within nanophotonic structures where they remain stationary. The interaction between these stationary emitters and a light field has been sought improved by means of an altered optical environment, treating the emitters as point-sources of light. The exception to this rule is the recent studies of very large quantum dot emitters that are investigated for their prospective large oscillator strength [47].

Solid-state emitters are defined by a charge-confining potential that extends over many crystal lattice sites, while being small enough to yield quantized energy levels of the confined charges. We introduce the notion of *mesoscopic emitters* to describe this regime where the confining potential is spatially much larger than the usual atomic potentials but still small enough to yield quantized energy levels. The emission energies from quantum dots is determined by their size and constituent materials and can thus be engineered by controlling their growth. Consequently, the term *artificial atoms* has been coined to describe

quantum dots. Perhaps, this nomenclature was part of the inspiration that led solid-state physicist to adapt the interaction formalism from atomic physics which has also proven itself widely successful.

The classical problem of an atom interacting with a plane-wave light field, $\mathbf{A}_0 e^{i(\mathbf{k}\cdot\mathbf{r}-\omega t)}$, where $\mathbf{k}$ is the wavevector, can be simplified by evoking the dipole approximation, i.e., that the optical field does not change over the extent of the emitter $a$, so that the vector potential can be simplified as $\mathbf{A}(\mathbf{r},t) \rightarrow \mathbf{A}(t)$. This is equivalent to requiring that

$$|\mathbf{k}|a = \frac{2\pi n}{\lambda_0} a \ll 1, \tag{3.1}$$

where $n$ is the refractive index of the surrounding medium and $\lambda_0$ is the free-space wavelength of the emission. We find that this relation is easily satisfied for atomic emitters where: $n \sim 1$, $a \sim 0.5$ nm, and $\lambda_0 \sim 500$ nm. For mesoscopic emitters, e.g., quantum dots where: $n \sim 3.5$, $a \sim 20$ nm, and $\lambda_0 \sim 1000$ nm the equality evaluates to $\sim 0.4 \ll 1$, which is no longer satisfied. Note that the high index of refraction of the surrounding medium enhances the breakdown of the dipole approximation. Furthermore, in nanophotonic structures (e.g. near metals as in Fig. 3.1) there exists field modes which have components of the wavevector much larger than $\frac{2\pi n}{\lambda_0}$ leading to even $k_i a_i > 1$, where $a_i$ is the size of the emitter in the $i$'th direction. This is clearly a violation of the condition for the dipole approximation.

In this chapter we describe the interaction of mesoscopic quantum emitters with a light field beyond the dipole approximation, i.e., including the effect of variations in the optical field over the spatial extent of the emitter, as shown in Fig. 3.1. To this end we expand the interaction Hamiltonian to first order of a Taylor series, which leads to the mesoscopic moment $\Lambda$ that is determined by the spatial properties (size, symmetries) of the emitter. Importantly, we find that for quantum dots the contribution to the interaction from the mesoscopic moment $\Lambda$ and the dipole moment $\mu$ can interfere on the ground state transition, which gives rise to a modification of the decay rate that is sensitively dependent on the size and orientation of the emitter.

This chapter is organized as follows. In Section 3.1 we derive the general formalism for decay from a mesoscopic emitter and the expression for the decay rate is calculated. In Section 3.2 we specifically extract the form of the dipole and mesoscopic moment for a self-assembled quantum dot using symmetry

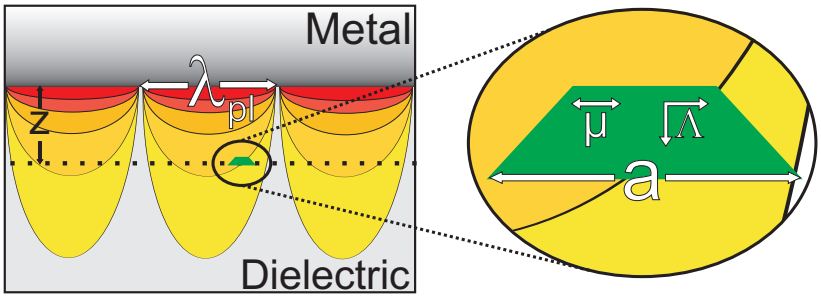


*Figure 3.1: Sketch of a mesoscopic quantum dot in an optical environment where the fields change over the spatial extent of the quantum dot. A quantum dot (green trapezoid) is placed a distance $z$ below a metal mirror. The lateral extension of a quantum dot emitting at* 1030 nm *is typically* $a = 20$ nm*. The plasmon wavelength is* $\lambda_{pl} = 262$ nm *(figure is not to scale). The arrow over* $\mu$ *indicates the orientation of the point-dipole moment and the arrows at* $\Lambda$ *the orientation of the first order mesoscopic moment, which is introduced in this chapter.*

considerations. In Section 3.3 the resulting decay rate for an emitter with only a dipole moment or only a mesoscopic moment placed near a silver mirror is calculated, which serves as a basis for understanding the decay dynamics where both moments contribute, which is the case for mesoscopic quantum dots. The resulting decay dynamics for such mesoscopic quantum dots is also shown in Section 3.3. In Section 3.4 the gauge-dependence of interaction Hamiltonians is discussed, and related to the formalism employed in this chapter. We relate the mesoscopic moments to the familiar multipolar moments of the multipolar interaction Hamiltonian in Section 3.4. Finally, the conclusions of the chapter are presented in Section 3.5.

## 3.1 Light-matter interaction beyond the dipole approximation

The interaction between light characterized by the vector and scalar potentials $\mathbf{A}$ and $\phi$, respectively, and a particle characterized by a mass $m$ and a charge

$q$ is described by the minimal coupling Hamiltonian [48]

$$H^{\min} = \frac{1}{2m}(\mathbf{p} - q\mathbf{A})^2 + V(\mathbf{r}) + q\phi + \frac{1}{2}\int \left(\epsilon_0\epsilon_r(\mathbf{r})E^2 + \frac{1}{\mu_0}B^2\right), \tag{3.2}$$

where $\mathbf{p}$ is the momentum operator, $V(\mathbf{r})$ is the potential felt by the particle, and the integral gives the energy of the unperturbed electromagnetic field. In the generalized Coulomb gauge, i.e., $\phi = 0$ and $\nabla \cdot [\epsilon_r(\mathbf{r})\mathbf{A}(\mathbf{r})] = 0$ as discussed in Appendix B, we can simplify the Hamiltonian to

$$H^{\min} = H_{\text{particle}} + H_{\text{field}} - \underbrace{\frac{q}{2m}(\mathbf{p}\cdot\mathbf{A} + \mathbf{A}\cdot\mathbf{p} - q\mathbf{A}\cdot\mathbf{A})}_{\mathrm{H_I^{min}}}. \tag{3.3}$$

The term proportional to $\mathbf{A}\cdot\mathbf{A}$ in the interaction part of the Hamiltonian is negligible for small fields and we will therefore neglect it in the following as we will study the interaction with vacuum fields. In the generalized Coulomb gauge, i.e. $\nabla \cdot [\epsilon_r(\mathbf{r})\mathbf{A}(\mathbf{r})] = 0$, the commutator $[\mathbf{A}, \mathbf{p}] = \nabla \cdot \mathbf{A}(\mathbf{r})$ is not in general equal to zero. However, throughout this thesis we consider structured dielectrics that have piecewise constant $\epsilon_r(\mathbf{r})$, ensuring that $[\mathbf{A}, \mathbf{p}] = 0$ when the commutator is not evaluated across the boundary between two materials. The resulting interaction Hamiltonian is then given by

$$H_I^{\min} = -\frac{q}{m}\mathbf{A}\cdot\mathbf{p}. \tag{3.4}$$

The quantized vector potential, represented in the interaction picture, is given by [49]:

$$\mathbf{A}(\mathbf{r}, t) = \sum_l \sqrt{\frac{\hbar}{2\epsilon_0\omega_l}}\left[\hat{a}_l e^{-i\omega_l t}\mathbf{f}_l(\mathbf{r}) + \hat{a}_l^\dagger e^{i\omega_l t}\mathbf{f}_l^*(\mathbf{r})\right], \tag{3.5}$$

where $\hat{a}_l$ and $\hat{a}_l^\dagger$ are the annihilation and the creation operators, respectively, for the optical field mode $\mathbf{f}_l(\mathbf{r})$, that oscillates with an angular frequency $\omega_l$ and fulfills the equations discussed in Appendix B.

We will describe the quantum dot as a two-level system as discussed in Chapter 2. We note that the solid-state nature of the quantum dot implies that these two levels are in reality many-particle states with the ground state being equal to an empty conduction band and a filled valence band, and the excited state defined from this but with a single electron from the valence band promoted to the conduction band, leaving a hole behind. We will here employ a single particle formalism where an electron can be either in the conduction

$|c\rangle$ or the valence band $|v\rangle$, corresponding to the excited and ground state respectively. In our experimental investigations, which will be presented in Chapter 4, we take care not to create multiple excitations in the quantum dot, which ensures that the two-level model is a good approximation to our experimental condition. We denote the energy difference between the excited and ground state $\Delta E = \hbar\omega_0$ and expand the interaction Hamiltonian on the complete set of electronic states $I = |v\rangle\langle v| + |c\rangle\langle c|$. We introduce the electronic raising and lowering operators $\hat{\sigma}_+ e^{+i\omega_0 t}$ and $\hat{\sigma}_- e^{-i\omega_0 t}$, respectively, as given in the interaction picture. The effect of the raising operator $\hat{\sigma}_+ = |c\rangle\langle v|$ is to promote the electron from the valence band to the conduction band and the effect of the lowering operator $\hat{\sigma}_- = |v\rangle\langle c|$ is the opposite.

The time dependence of the light-field creation and annihilation operators, $e^{\pm i\omega_l t}$, combined with the time dependence of the electronic raising and lowering operators, $e^{\pm i\omega_0 t}$, give rise to four different time dependencies, $e^{\pm i(\omega_l+\omega_0)t}$ and $e^{\pm i(\omega_l-\omega_0)t}$. In the rotating wave approximation, i.e., neglecting all terms oscillating as $e^{\pm i(\omega_l+\omega_0)t}$ as these contributions average to zero over the much slower oscillating $e^{\pm i(\omega_l-\omega_0)t}$ when $\omega_l \approx \omega_0$, we get

$$H_I(\mathbf{r},t) = -\frac{q}{m}\sum_l \sqrt{\frac{\hbar}{2\epsilon_0\omega_l}}\Big[e^{i\Delta_l t}\hat{\sigma}_-\hat{a}_l^\dagger\langle v|\mathbf{f}_l^*(\mathbf{r})\cdot\mathbf{p}|c\rangle + e^{-i\Delta_l t}\hat{\sigma}_+\hat{a}_l\langle c|\mathbf{f}_l(\mathbf{r})\cdot\mathbf{p}|v\rangle\Big], \quad (3.6)$$

where $\Delta_l = \omega_l - \omega_0$.

The wavefunctions that represent the electron in the conduction and valence band respectively are spatially extended with their extent determined by the size of the quantum dot. The usual next simplifying step is the dipole approximation, i.e., to assume that the field modes ($\mathbf{f}_l(\mathbf{r})$) do not change over the extent of the quantum dot whereby they can be pulled out of the matrix elements $\langle v|\mathbf{f}_l(\mathbf{r})\cdot\mathbf{p}|c\rangle \rightarrow \langle v|\mathbf{p}|c\rangle\cdot\mathbf{f}_l(\mathbf{r})$ and likewise for $\mathbf{f}_l^*(\mathbf{r})$. Here we wish to address the decay dynamics of mesoscopic quantum dots for which this approximation is not valid *a priori*.

Calculations of decay dynamics beyond the dipole approximation can be performed in two distinctively different ways:

Firstly, one could set out to calculate the matrix elements above taking the full spatial dependence of the wavefunctions and electromagnetic fields into

consideration

$$\langle v|\mathbf{f}_l(\mathbf{r})\cdot\mathbf{p}|c\rangle = \int \Psi_v^*(\mathbf{r})\mathbf{f}_l(\mathbf{r})\cdot\mathbf{p}\Psi_c(\mathbf{r}), \tag{3.7}$$

where $\Psi_v(\mathbf{r})$ and $\Psi_c(\mathbf{r})$ are the wavefunctions for the electron in the valence and conduction band, respectively. The wavefunctions are very complicated as they contain both the dependence of the crystal lattice as well as the confinement determined by the InAs distribution, both of which are very difficult to obtain for real quantum dots. Only a few theoretical works have been conducted where the dipole approximation has not been made [50, 51, 52, 53]. In these, the quantum dot is modeled with an uniform lattice structure and a highly symmetric confinement potential. While these approaches are interesting in their own right, they fail to capture some of the very exciting physics of mesoscopic emitters that we will discuss here.

Secondly, the matrix element can be calculated by Taylor expanding the field modes around the center of the quantum dot ($\mathbf{r} = \mathbf{r}_0$)

$$f_{l,j}(\mathbf{r}) \approx f_{l,j}(\mathbf{r}_0) + \sum_n (\mathbf{r}-\mathbf{r}_0)_n \left[\nabla_n f_{l,j}(\mathbf{r})\right]_{\mathbf{r}=\mathbf{r}_0} + \ldots, \tag{3.8}$$

where we have changed to a coordinate description with $j$ and $n$ both running over $\{x, y, z\}$, resulting in a set of matrix elements for each order of the Taylor expansion. Here we will perform the Taylor expansion to first order and introduce two moments that we will associate with point-dipole $\mu_j = \langle v|p_j|c\rangle$ and first order terms ($\Lambda_{j,n} = \langle v|(\mathbf{r}-\mathbf{r}_0)_n p_j|c\rangle$). We will in the following, not write the sum explicitly for repeated coordinate indices, which will help to simplify notation

$$H_I(\mathbf{r}_0,t) = -\frac{q}{m}\sum_l \sqrt{\frac{\hbar}{2\epsilon_0\omega_l}}\Big[e^{i\Delta_l t}\hat{\sigma}_-\hat{a}_l^\dagger(\mu_j + \Lambda_{n,j}\nabla_n)f_{l,j}^*(\mathbf{r}) + e^{-i\Delta_l t}\hat{\sigma}_+\hat{a}_l(\mu_j^* + \Lambda_{n,j}^*\nabla_n)f_{l,j}(\mathbf{r})\Big]_{\mathbf{r}=\mathbf{r}_0}. \tag{3.9}$$

This resulting Hamiltonian for a two-level system beyond the dipole approximation, contains the mesoscopic nature of the quantum dots through the mesoscopic moments $\Lambda_{n,j}$. The calculation of $\Lambda_{n,j}$ for a real quantum dot is not much easier than the full calculation of the matrix elements Eq. (3.7). The calculation of $\Lambda_{n,j}$ also relies on detailed knowledge of the quantum dot wavefunctions, but it allow us to attribute an intrinsic property to the emitter that contains its mesoscopic nature, whereas the approach of Eq. (3.7) intertwine the spatial dependence of the specific field and the emitter.

### 3.1.1 Time-evolution of a two-level quantum dot beyond the dipole approximation

The Schrödinger equation in the interaction picture

$$i\hbar\partial\Psi(t)/\partial t = H_I(\mathbf{r}_0, t)\Psi(t) \tag{3.10}$$

governs the time evolution of the general state of the system under investigation

$$|\Psi(t)\rangle = c_e(t)|i\rangle + \sum_{l'} c_{l'}(t)|f_{l'}\rangle. \tag{3.11}$$

Here, $|i\rangle$ and $|f_{l'}\rangle$ are the initial- and final states, and $c_e(t)$ and $c_{l'}(t)$ are the expansion coefficients for these. Only a single initial state $|i\rangle = |0\rangle \otimes |c\rangle$ exists by construction, corresponding to an empty light field $|0\rangle$ and a single electron promoted to the conduction band $|c\rangle$. There is, on the other hand, a multitude of final states $|f_{l'}\rangle = |1_{l'}\rangle \otimes |v\rangle$ with an electron in the valence band and a single photon in the field mode $\mathbf{f}_{l'}(\mathbf{r})$. We can now apply Eq. (3.10) with Eq. (3.9) to work on Eq. (3.11), and project the resulting expression onto $|i\rangle$ and $|f\rangle$, which gives

$$i\hbar\frac{\partial c_e(t)}{\partial t} = -\frac{q}{m}\sum_l \sqrt{\frac{\hbar}{2\epsilon_0\omega_l}} e^{-i\Delta_l t}(\mu_j^* + \Lambda_{n,j}^*\nabla_n) f_{l,j}(\mathbf{r}) c_l(t)\Big|_{\mathbf{r}=\mathbf{r}_0}, \tag{3.12}$$

$$i\hbar\frac{\partial c_l(t)}{\partial t} = -\frac{q}{m}\sqrt{\frac{\hbar}{2\epsilon_0\omega_l}} e^{i\Delta_l t}(\mu_{j'} + \Lambda_{n',j'}\nabla'_n) f^*_{l,j'}(\mathbf{r}') c_e(t)\Big|_{\mathbf{r}'=\mathbf{r}_0}, \tag{3.13}$$

respectively. Formally integrating Eq. (3.13) with respect to time and substituting the result into Eq. (3.12) we get

$$\begin{aligned}\frac{\partial c_e(t)}{\partial t} = -\frac{q^2}{2m^2\epsilon_0\hbar}\Big( &\left[\mu_j^* + \Lambda_{n,j}^*\nabla_n\right]\left[\mu_{j'} + \Lambda_{n',j'}\nabla'_{n'}\right] \\ &\times \sum_l \frac{1}{\omega_l} f_{l,j}(\mathbf{r}) f^*_{l,j'}(\mathbf{r}') \int_0^t dt' c_e(t') e^{-i\Delta_l(t-t')}\Big)\Big|_{\mathbf{r}=\mathbf{r}'=\mathbf{r}_0},\end{aligned} \tag{3.14}$$

which we can rewrite as an integral over $\omega$ when we introduce a $\delta$-function

$$\begin{aligned}\frac{\partial c_e(t)}{\partial t} = -\frac{q^2}{2m^2\epsilon_0\hbar}\Big( &\left[\mu_j^* + \Lambda_{n,j}^*\nabla_n\right]\left[\mu_{j'} + \Lambda_{n',j'}\nabla'_{n'}\right] \\ &\times \int_{-\infty}^{\infty} d\omega \sum_l \frac{1}{\omega_l} f_{l,j}(\mathbf{r}) f^*_{l,j'}(\mathbf{r}')\delta(\omega - \omega_l) \\ &\times \int_0^t dt' c_e(t') e^{-i(\omega-\omega_0)(t-t')}\Big)\Big|_{\mathbf{r}=\mathbf{r}'=\mathbf{r}_0}.\end{aligned} \tag{3.15}$$

The sum over the field modes can be related to the expression for the imaginary part of the dyadic Green's function calculated in Appendix B

$$\mathrm{Im}\left[\mathbf{G}(\mathbf{r},\mathbf{r}';\omega)\right] = \frac{\pi}{2}\sum_l \frac{1}{\omega_l}\mathbf{f}_l^*(\mathbf{r}';\omega_l)\mathbf{f}_l(\mathbf{r};\omega_l)\delta(\omega-\omega_l), \tag{3.16}$$

which allows us to rewrite the expression in terms of the dyadic Green's function. In the Wigner-Weisskopf approximation [54], i.e., assuming the dyadic Green's function is slowly varying over the linewidth of the emitter, we can evaluate the dyadic Green's function at the emission frequency $\omega = \omega_0$ and pull it outside the integral over time, resulting in

$$\frac{\partial c_e(t)}{\partial t} = -\frac{q^2}{\pi m^2\epsilon_0\hbar}\Big( \left[\mu_j^* + \Lambda_{n,j}^*\nabla_n\right]\left[\mu_{j'} + \Lambda_{n',j'}\nabla'_{n'}\right] \times \mathrm{Im}(G_{j,j'}(\mathbf{r},\mathbf{r}';\omega_0)) \int_{-\infty}^{\infty} d\omega \int_0^t dt' c_e(t') e^{-i(\omega-\omega_0)(t-t')}\Big)\Big|_{\mathbf{r}=\mathbf{r}'=\mathbf{r}_0}. \tag{3.17}$$

The integral over frequency evaluates as $\int_{-\infty}^{\infty} d\omega e^{-i(\omega-\omega_0)(t-t')} = 2\pi\delta(t-t')$, and the integral over time can subsequently be carried out to yield

$$\frac{\partial c_e(t)}{\partial t} = -\frac{q^2}{m^2\epsilon_0\hbar}\Big( \left[\mu_j^* + \Lambda_{n,j}^*\nabla_n\right]\left[\mu_{j'} + \Lambda_{n',j'}\nabla'_{n'}\right] \times \mathrm{Im}(G_{j,j'}(\mathbf{r},\mathbf{r}';\omega_0))c_e(t)\Big)\Big|_{\mathbf{r}=\mathbf{r}'=\mathbf{r}_0}, \tag{3.18}$$

which is an easily solvable differential equation in $c_e(t)$. The final expression for the experimentally relevant population decay rate $\Gamma(\mathbf{r}_0,\omega_0)$, defined through $|c_e(t)|^2 = \exp[-\Gamma(\mathbf{r}_0,\omega_0)t]$ is

$$\Gamma(\mathbf{r}_0,\omega_0) = \frac{2q^2}{m^2\epsilon_0\hbar}\Big( \left[\mu_j^* + \Lambda_{n,j}^*\nabla_n\right]\left[\mu_{j'} + \Lambda_{n',j'}\nabla'_{n'}\right] \times \mathrm{Im}(G_{j,j'}(\mathbf{r},\mathbf{r}';\omega_0))\Big)\Big|_{\mathbf{r}=\mathbf{r}'=\mathbf{r}_0}. \tag{3.19}$$

We note that the familiar expression within the dipole approximation is obtained for $\Lambda_{n,j} = \Lambda_{n',j'} = 0$ which is the expression introduced in Chapter 2. The first order moments $\Lambda_{n,j}$ in Eq. (3.19) describe the mesoscopic nature of the quantum dot, and together with the dipole moment $\mu_j$ determine, the decay rate of the excited quantum dot. There are three entries in the dipole moment, one for each coordinate axis, while the mesoscopic moment $\Lambda_{n,j}$ has nine entries; one for each gradient of each coordinate axis. As seen in Eq. (3.19), the

decay rate mediated by the mesoscopic moment is determined by the gradient of the imaginary part of the dyadic Green's function, while the contribution mediated by the dipole moment is determined by the value of the Green's function itself. Both $\mu_j$ and $\Lambda_{n,j}$ are intrinsic properties of the quantum dots and as such independent of the electromagnetic environment. This implies that once these moments are known it is straightforward to calculate the complicated interaction of an extended quantum dot and an arbitrary electromagnetic environment.

## 3.2 Quantum dot transition moments

The transition moments $\mu_j$ and $\Lambda_{n,j}$ for the quantum dot determine the decay dynamics. Here we investigate the form of these for a real quantum dot. Specifically, we consider the symmetry properties of the quantum dot wavefunctions, which lead to certain restrictions on which entries $\mu_j$ and $\Lambda_{n,j}$ that are non-zero. For this purpose we make the ansatz that the wavefunctions can be decomposed into a part that contains the dynamics on the length scale of a crystal unit cell, and a part that contains the dynamics on the length scale of the quantum dot confining potential, termed Bloch and envelope functions, respectively [37]. The wavefunctions can then be written as

$$\Psi_c(\mathbf{r}) = F_c(\mathbf{r})u_{c,0}(\mathbf{r}), \tag{3.20}$$

$$\Psi_v(\mathbf{r}) = F_v(\mathbf{r})u_{hh,0}(\mathbf{r}), \tag{3.21}$$

where we have used that the degeneracy of the valence band is lifted, resulting in the dominating Bloch function being the heavy hole Bloch function $u_{hh,0}(\mathbf{r})$, as discussed in Chapter 2. The subscript 0 denotes that the Bloch functions are evaluated at the $\Gamma$-point in the direct bandgap semiconductor where the electron momentum $\mathbf{k} = 0$. We will adapt the growth direction as the $z$-axis in our quantum dots, as we note that the dispersion for the Bloch states is non-uniform in real materials. The conduction band and heavy hole Bloch functions can be written as linear superpositions of functions with $s$- and $p$-orbital-like symmetries, known from atomic physics [33, 55]. We introduce $u_s$, which has even symmetry in all three spatial directions and $u_{x,y,z}$ where, e.g., $u_x$ has odd symmetry along $x$ and even symmetry in the two other directions, similar to a

$p$-like symmetry. Thus, the bulk Bloch functions are given as [37]:

$$u_{c,0}(\mathbf{r}) = u_s, \tag{3.22}$$

$$u^{\pm}_{hh,0}(\mathbf{r}) = \frac{1}{\sqrt{2}}(u_x \pm iu_y), \tag{3.23}$$

where the heavy-hole Bloch function is a superposition state. Real quantum dots are not in-plane rotationally symmetric as their in-plane shape is normally slightly elliptic, implying that the heavy-hole functions above are no longer good eigenstates. Two new hole eigenstates result in slightly different energies and have the Bloch part of one as $u_x$-like and the Bloch part of the other as $u_y$-like. Here, however, we describe the quantum dots as being in-plane rotationally symmetric.

The envelope functions, $F_c$ and $F_v$, are determined by the confining potential given by the shape of the quantum dot and its material distribution. We describe the quantum dots as rotationally symmetric, which implies that both envelope functions have even parity in the $x$-direction and the $y$-direction. The quantum dot is grown on top of a wetting layer and its shape has been described as resembling a truncated pyramid or lens. Common for both geometry descriptions is that these do not infer any symmetry to the confining potential along the $z$-direction and therefore not to the envelope functions along the $z$-direction. The wavefunctions for the electron and hole have a resulting overall symmetry determined by its constituent parts, i.e. the Bloch and envelope functions. The resulting symmetry for the part of the heavy-hole superposition that has $u_x$ character is summarized in Table 3.1. Where 1, $-1$, and 0 indicate even symmetry, odd symmetry, and asymmetry respectively, for each of the three cartesian directions. The results are shown for both envelope, Bloch, and complete wavefunctions for conduction and valence band states, independently.

The transition matrix elements are given as $\int \Psi_v^* \hat{O} \Psi_c$ where $\hat{O} = \hat{p}_j$ and $\hat{O} = \hat{r}_n \hat{p}_j$ for $\mu_j$ and $\Lambda_{n,j}$, respectively. The symmetry properties of a wavefunction that has been acted upon by operators, e.g., $\hat{p}_j \Psi$ or $\hat{r}_n \Psi$, are changed from those of the bare wavefunction $\Psi$. The result for either operator is that of reversing the symmetry so that an even symmetry becomes odd and *viceversa*. Such operator symmetry considerations on the wavefunction symmetries listed above, yields that only $\hat{p}_x$ gives a non-zero $\mu$-matrix element, which we will call $\mu_x$, furthermore, $\mu_y = \pm i\mu_x$, and $\mu_z = 0$. The two signs stem from the two different degenerate eigenstates of the quantum dot.

| | $F_c$ | $u_c$ | $\Psi_c$ | $F_v$ | $u_{hh}$ | $\Psi_v$ |
|---|---|---|---|---|---|---|
| x | 1 | 1 | 1 | 1 | -1 | -1 |
| y | 1 | 1 | 1 | 1 | 1 | 1 |
| z | 0 | 1 | 0 | 0 | 1 | 0 |

*Table 3.1: Symmetries of the quantum dot wavefunctions. The symmetry is categorized as either even (1), odd (-1), or asymmetric (0) along each of the three coordinate axis $x$, $y$, $z$. The results are shown for both envelope-, Bloch-, and wave-function. For the heavy hole part we show the result for a Bloch state with $u_x$-like symmetry.*

When we make the same considerations for the mesoscopic moment $\Lambda$ we find that either $\hat{r}$ or $\hat{p}$ has to be along $x$ or $y$, while the other has to be along $z$ in order to yield non-zero matrix elements. Thus, the resulting $\Lambda$ is $\Lambda_{xx} = \Lambda_{yy} = \Lambda_{xy} = \Lambda_{yx} = \Lambda_{zz} = 0$, $\Lambda_{xz} = \pm i\Lambda_{yz} = \Lambda_1$, and $\Lambda_{zx} = \pm i\Lambda_{zy} = \Lambda_2$. Where the plus or the minus sign should be chosen in accordance with the choice for $\mu$. With these considerations the amount of free parameters that go into describing the decay dynamics of mesoscopic quantum dots are greatly reduced.

We note that had we assumed the envelope function to have even symmetry also along the $z$-direction then $\Lambda_{n,j} = 0$. The non-zero mesoscopic moments is an important result that differs markedly from the atom-like picture often employed in the description of quantum dots. The asymmetry of the quantum dot wavefunctions is possible due to the extended size of these emitter. The inclusion of the mesoscopic moment alters the decay rate on the ground state transition through the gradient of the electromagnetic surroundings. In the next section the effect on the decay rate of the mesoscopic character of quantum dots will be studied in a simple electromagnetic environment.

## 3.3 Decay dynamics near a silver mirror

We will calculate the rate of decay for an emitter near a silver mirror characterized by the refractive index $n = 0.2 + 7i$. The medium surrounding the emitter is GaAs for which $n = 3.42$ and the emitter emits light at a free-space wave-

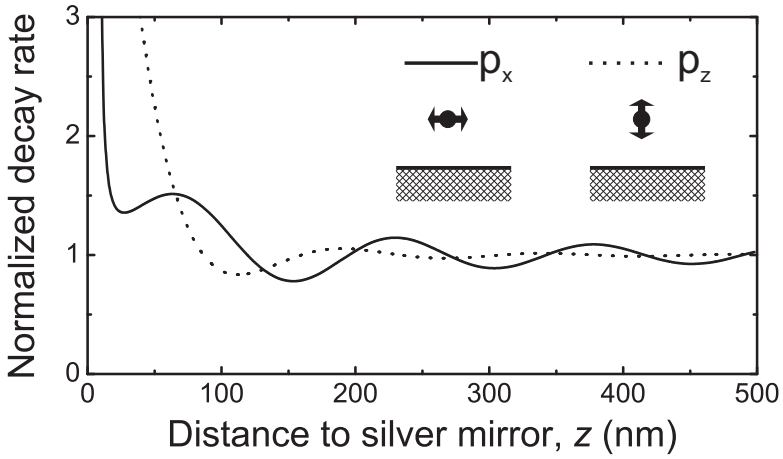


*Figure 3.2: Normalized decay rates for a dipole emitter near a silver mirror. The calculated normalized decay rates as function of distance to a silver mirror are shown for two different dipole orientations (see insets), parallel to the mirror (solid line) and perpendicular (dashed line).*

length of $\lambda_0 = 1000$ nm. The decay rate can be calculated with Eq. (3.19) using the corresponding dyadic Green's function that is presented in Appendix A.

The decay rate normalized to the decay rate in an homogeneous medium is given by $\Gamma_{\text{mirror}}(z_0, \omega_0)/\Gamma_0(\omega_0)$ where both the decay rate in the homogeneous medium and near the mirror include the contribution of $\mu_j$ and $\Lambda_{n,j}$. For a dipole emitter $\Lambda_{n,j} = 0$ the decay rates for $\mu_x$ and $\mu_y$ are equal, due to the symmetry of the environment. We will therefore only consider one excited state, i.e. along $x$, without any loss of generality. The decay rates of dipoles oriented along $x$ and $z$ is shown in Fig. 3.2. The resultant oscillations are due to interference between the direct and reflected field from the dipole emitter. Note that the two oscillations are out of phase, which provides an experimental method to easily distinguish the two dipole orientations. Close to the interface ($\sim 100$ nm) the decay rate is enhanced due to coupling to plasmons, and very close to the interface ($\sim 20$ nm) the decay rate is strongly enhanced as the dipole is coupling to ohmic losses in the metal. The plasmonic field is polarized such that a dipole along $z$ couples more efficiently to the plasmonic field, which is the reason for the observed difference in decay rate for $z < 100$ nm.

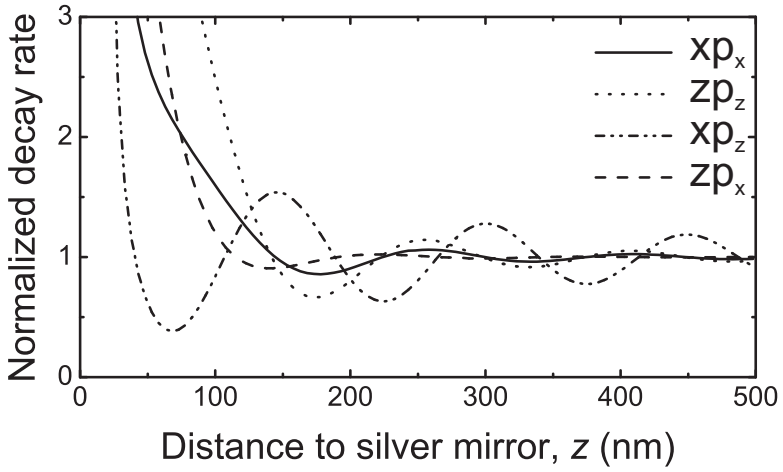


*Figure 3.3: Normalized decay rates for a purely mesoscopic emitter ($\mu = 0$) near a silver mirror. The calculated normalized decay rates as function of distance to the silver mirror are shown for four different mesoscopic moments, $\langle v|xp_x|c\rangle$ (solid line), $\langle v|zp_z|c\rangle$ (dotted line), $\langle v|xp_z|c\rangle$ (dash-dotted line), and $\langle v|zp_x|c\rangle$ (dashed line).*

Similarly we set $\mu = 0$ and study the effect of the four independent entries to $\Lambda$ in this geometry, namely $xp_x$, $zp_z$, $xp_z$, and $zp_x$, where the last two are important for quantum dots as discussed above. The results are shown in Fig. 3.3. The decay dynamics resemble those of a pure electric quadrupole or magnetic dipole where the interaction with light is given by the gradients of the optical field only. The relationship between the formalism presented here to a multipolar description of light-matter interaction will be addressed in Section 3.4. Importantly, the normalized decay dynamics for an emitter with purely dipolar or mesoscopic moments is not dependent on the size and sign of these moments but only on their orientation. The decay rates shown in Fig. 3.2 and Fig. 3.3 are thus limiting cases for those of a real quantum dot described by a combination of both moments as expressed in Eq. (3.19).

When both moments contribute to the decay dynamics the two different decay mechanisms can interfere, as shown in Fig. 3.4. The decay dynamics is now dependent on both the relative sign and size of the two moments. When either $\mu$ or $\Lambda$ are dominating the decay dynamics, the results shown in Fig. 3.2

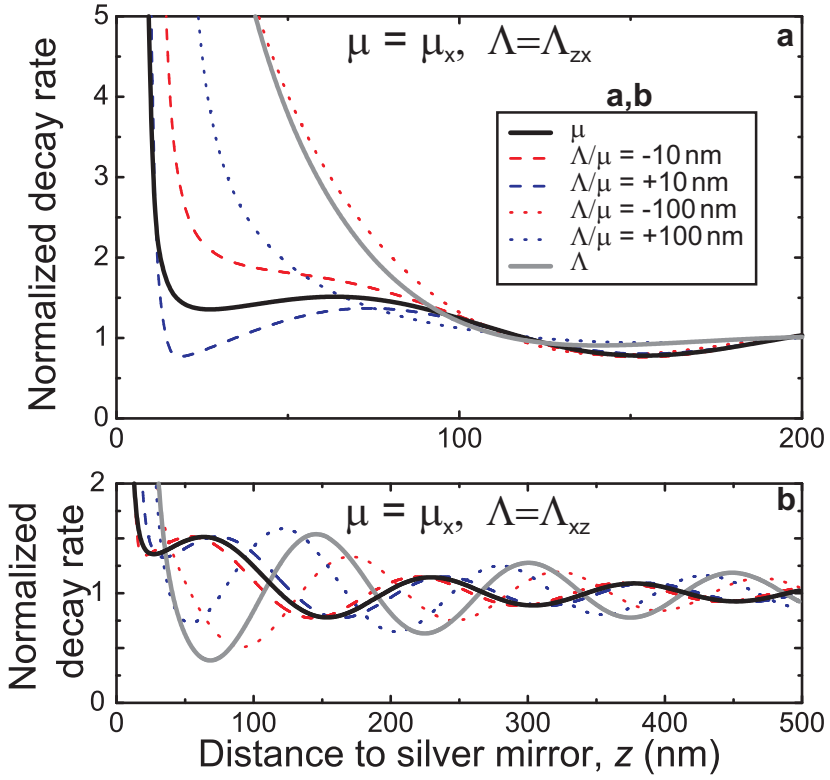


*Figure 3.4: Normalized decay rates of mesoscopic quantum dots near a silver mirror. The decay rates are determined by both $\mu$ and $\Lambda$, the result for $\Lambda/\mu = \pm 10$ nm and $\Lambda/\mu = \pm 100$ nm are shown as dashed and dotted lines respectively, with the (+) sign shown in blue and (-) in red. The black and grey lines are for a pure dipole and pure mesoscopic moment transitions, respectively. In* **a** *and* **b** *$\mu = \mu_x$.* **a** *$\Lambda = \Lambda_{z,x}$.* **b** *$\Lambda = \Lambda_{x,z}$. Note different distance scales in the two plots.*

and Fig. 3.3 are recovered, but when they are balanced in size they interfere differently depending on their relative sign. The physical quantity of the ratio $\Lambda/\mu$, e.g

$$\frac{\Lambda_{z,x}}{\mu_x} = \frac{\langle v|xp_z|c\rangle}{\langle v|p_x|c\rangle}, \tag{3.24}$$

is a length. In Fig. 3.4 we state the size of $\Lambda/\mu$ in nanometer, which is a convenient measure as the deviations from dipole theory start to occur for $\Lambda/\mu \sim 1$ nm. In Fig. 3.4 we show the resulting decay rates for the intermixing of $\mu_x$ with the two different mesoscopic moment relevant to quantum dots $\Lambda_{z,x}$ (Fig. 3.4a) and $\Lambda_{x,z}$ (Fig. 3.4b) for $\Lambda/\mu = \pm 10$ nm and $\Lambda/\mu = \pm 100$ nm as well as the two limiting cases $\Lambda = 0$ and $\mu = 0$. The sign of the moments only make sense in relation to a coordinate system, which is fixed by the environment in which the emitter is embedded. This has the consequence that the sign of the $\Lambda_{z,x}$ can be changed by mirroring the emitter along the $z$-axis. The same mirroring does not affect $\mu_x$, and thus the sign of the ratio $\Lambda_{z,x}/\mu_x$ is also changed. The resulting decay rates in these two cases are very different, cf. Fig. 3.4, which we will utilize in Chapter 4, to provide the proof for the mesoscopic nature of quantum dots. Note that the interference leads to both enhancement and suppression of the decay rate and that the effect is determined by the sign of $\Lambda/\mu$.

### 3.3.1 Decomposition of decay mechanisms

Near metals there exist bound modes that can be divided into plasmonic modes and, very near metals, lossy modes. The expression for the decay rate in structured dielectrics (Eq. (3.19)) can be decomposed into the different decay mechanisms by intervals of the in-plane wavevector $k_\parallel$ in the dyadic Green's function [56].

For $k_\parallel \in [0, k_d]$, the emitter couples to freely propagating photons, as the out of plane wavevector $k_z = \sqrt{k_d^2 - k_\parallel^2}$ is real-valued, where $k_d = 2\pi n/\lambda_0$ with $n$ being the refractive index of the dielectric. The interval $k_\parallel \in ]k_d, \infty[$ contains the plasmon resonance $k_{\mathrm{pl}} = k_0\sqrt{\epsilon_d\epsilon_m/(\epsilon_d + \epsilon_m)}$, and describes all modes that are bound to the interface, where $k_0$ is the wavevector in vacuum and $\epsilon_d$ and $\epsilon_m$ is the permittivity of the dielectric and the metal, respectively. We associate $k_\parallel \in ]k_d, 2k_{\mathrm{pl}} - k_d[$ with coupling to plasmons and larger $k_\parallel \geq 2k_{\mathrm{pl}} - k_d$ with coupling to lossy modes [56]. The dyadic Green's function for a simple

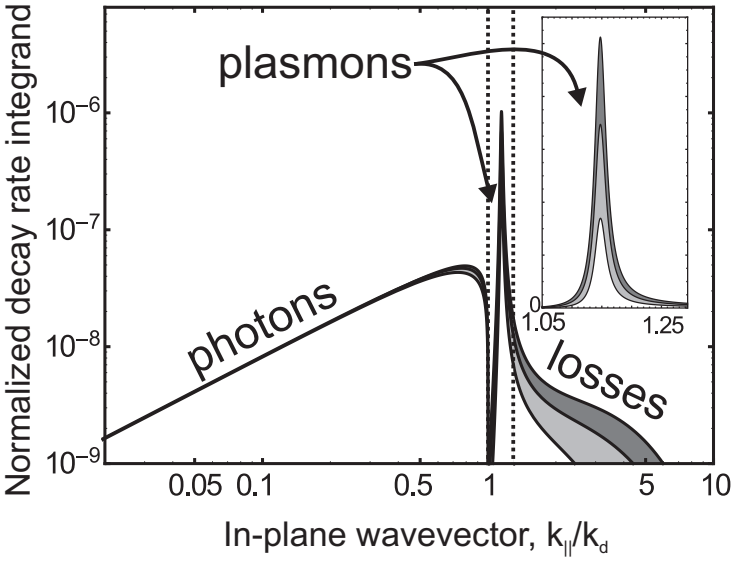


*Figure 3.5: Decomposition of decay rates for an emitter at a distance of* 20 nm *from a silver mirror. The normalized decay rate is constructed as an integral over the in-plane wavevector $k_{\|}$ and thus corresponds to the area under the integrand in this plot. The integrand is shown divided into photons, plasmons, and lossy modes (losses) by two vertical dotted lines. The result is shown for an in-plane dipole $\mu_x$ and a mesoscopic moment given by $\Lambda_{z,x}/\mu_x = +10, 0, -10$* nm *with white, light grey, and dark grey fill, respectively. The inset, shows the coupling to plasmons on a linear scale.*

slab structure can be expressed as an integral over the in-plane wavevector, as shown in Appendix A, which makes the subdivision into different decay mechanisms straightforward to implement. Figure 3.5 shows the decomposition for a distance $z = 20$ nm to a silver mirror, for an in-plane dipole $\mu_x$ and a mesoscopic moment given by $\Lambda_{z,x}/\mu_x = 0, +10$ nm, and -10 nm. The deviations from the result obtained within the dipole approximation, i.e. $\Lambda_{z,x}/\mu_x = 0$, is larger for coupling to modes with large $k_{\|}$. This is consistent with the simple notion that the dipole approximation is justified when $ka \ll 1$. The coupling to the plasmonic mode is strongly affected by the inclusion of the mesoscopic moment and can be either enhanced or suppressed from its dipole value, as shown in inset of Fig. 3.5.

## 3.4 Gauge transformations

In Section 3.1 we used the generalized Coulomb gauge to fix the electromagnetic potentials. The physical electric and magnetic fields are invariant under a gauge transformation of the potentials and therefore it is an often used and well-advised practice to choose the gauge that simplifies calculations, as we did in Section 3.1. In quantum-electro-dynamics the Schrödinger equation is not form invariant under a gauge transformation of the electromagnetic potentials unless also the wavefunctions are transformed. In this way quantum-electro-dynamics is a gauge invariant formalism under the following transformation determined by the arbitrary scalar function $\lambda(\mathbf{r}, t)$

$$\mathbf{A} \to \mathbf{A} + \nabla\lambda(\mathbf{r}, t) \tag{3.25}$$

$$\phi \to \phi - \frac{\partial\lambda(\mathbf{r}, t)}{\partial t} \tag{3.26}$$

$$\Psi \to e^{iq\lambda(\mathbf{r},t)/\hbar}\Psi. \tag{3.27}$$

It is easy to verify that the Schrödinger equation

$$\left(\frac{(\mathbf{p} - q\mathbf{A})^2}{2m} + q\phi + V\right)\Psi = i\hbar\frac{\partial}{\partial t}\Psi, \tag{3.28}$$

is form invariant under such a transformation. Thus, these equations tell us how we should transform the wavefunctions, when we shift from one gauge to another.

In perturbation theory, the interaction part of the Hamiltonian, $H_I$, is described as a perturbing term, and the wavefunctions are eigenfunctions of the unperturbed and gauge-independent Hamiltonian, $H_0$. Thus, the question of which gauge to choose for the interaction Hamiltonian to do meaningful perturbation theory on the eigenfunctions of $H_0$, arises. We will discuss this problem of gauge-dependent perturbation theory in more detail in Appendix C. Here, it suffices to cite the summary of Ref. [57]: *"Only for non-resonant transitions induced by a monochromatic field does the hybrid procedure yield contradictory results in different gauges."*, where *hybrid procedure* refers to transformation of the electromagnetic potentials only while leaving the wavefunctions unaltered. In our formalism we have explicitly invoked energy conservation through the rotating wave and Wigner-Weiskopff approximations, which ensures that the decay dynamics calculated in this chapter are consistent with results from a gauge-invariant formulation.

### 3.4.1 Relation to multipolar moments

A different approach to gauge dependent formalisms is to recast the entire Hamiltonian in a gauge-independent form. Such a form can be constructed by Taylor expanding the scalar and vector potentials of the minimal coupling Hamiltonian [58] or from a canonical transformation [59]. In this form the light-matter interaction Hamiltonian is given as a multipolar series (multipolar interaction Hamiltonian)

$$H_I^{\text{mult}}(\mathbf{r}_0,t) = q_{\text{tot}}\phi(\mathbf{r}_0,t) - \mathbf{d}\cdot\mathbf{E}(\mathbf{r}_0,t) - \mathbf{m}\cdot\mathbf{B}(\mathbf{r}_0,t) - (\mathbf{Q}\nabla)\cdot\mathbf{E}(\mathbf{r}_0,t) - \ldots, \tag{3.29}$$

with

$$q_{\text{tot}} = \sum_n q_n \tag{3.30a}$$

$$\mathbf{d} = \sum_n q_n \mathbf{r}_n \tag{3.30b}$$

$$\mathbf{m} = \sum_n (q_n/2m_n)\mathbf{r}_n \times \mathbf{p}_n \tag{3.30c}$$

$$\mathbf{Q} = \sum_n (q_n/2)\mathbf{r}_n\mathbf{r}_n. \tag{3.30d}$$

where $q_{\text{tot}}$ is the total charge, $\mathbf{d}$ is the electric dipole moment, $\mathbf{m}$ is the magnetic dipole moment, and $\mathbf{Q}$ is the electric quadrupole moment. The contribution from the scalar potential, $\phi$, at $\mathbf{r}_0$ vanish for a neutral charge configuration. The magnetic dipole- and electric quadrupole moment originate from the same expansion order of the interaction and their contribution to the Hamiltonian should be compared to the contribution from the mesoscopic moments in the formalism presented in this chapter.

To gain some physical insight, we compare the mesoscopic moments to the magnetic dipole and electric quadrupole moments by considering the tensor identity [60]

$$U_iV_j = \frac{\mathbf{U}\cdot\mathbf{V}}{3}\delta_{i,j} + \frac{U_iV_j - U_jV_i}{2} + \left(\frac{U_iV_j + U_jV_i}{2} - \frac{\mathbf{U}\cdot\mathbf{V}}{3}\delta_{i,j}\right), \tag{3.31}$$

which relates a cartesian dyadic tensor to components that transform like spherical harmonics. Along this line, we can transform a component of the $r_ip_j$-tensor that occur in our formalism, e.g., for the moment $xp_z$ we find

$$xp_z = \frac{(\mathbf{r}\times\mathbf{p})_y}{2} + \frac{xp_z + zp_x}{2}. \tag{3.32}$$

Where we have not isolated the part that gives rise to a scalar product as in Eq. (3.31). The first of these terms give rise to a cross-product between $\mathbf{p}$ and $\mathbf{r}$ just as for the magnetic dipole moment $\mathbf{m}$. The transition moment resulting from the second term $\langle v|xp_z + zp_x|c\rangle$, can be rewritten utilizing that $\mathbf{p} = -m\frac{i}{\hbar}[\mathbf{r}, H_0]$ and $[x_i, p_j] = i\hbar\delta_{i,j}$ as

$$\langle v|xp_z + zp_x|c\rangle = -i\frac{m\omega_0}{2}\langle v|xz + zx|c\rangle, \tag{3.33}$$

where $\hbar\omega_0 = E_c - E_v$ is the energy difference between the conduction and valence band states. The result is on the same form as the definition of the electric quadrupole tensor $\mathbf{Q}$. This shows that the mesoscopic moments contain contributions of both magnetic dipole and electric quadrupole character. Note that the same considerations for the moment $zp_x$ would change the sign of the magnetic dipole term and leave the quadrupole term unaffected. From this, we find that if $\langle v|xp_z|c\rangle = \pm\langle v|zp_x|c\rangle$ then the effect of including both moments correspond to purely electric quadrupole or magnetic dipole decay dynamics, for the plus and minus sign respectively. In summary, we have discussed the relation between the mesoscopic moments of the present formalism and the multipolar moments. Specifically, for the mesoscopic moments of quantum dots we find that these contain both magnetic dipolar and electric quadrupolar contributions.

## 3.5 Conclusion

We have developed a formalism for the interaction of extended mesoscopic emitters with a spatially varying optical field. This leads to additional moments (besides the dipole moment) in the description of the light-matter interaction. Simple symmetry considerations of quantum dots led to the conclusion that the introduced mesoscopic moments give non-zero contributions to the decay rate on the ground state transition, which is a clear departure of the description inherited from atomic physics where the absolute parities of the wavefunctions ensures that only operators with either even or odd parity yield non-zero results but never simultaneously. As an application of the model, we calculated the decay dynamics of an emitter with both a dipole moment and a mesoscopic moment near a silver mirror. When they are co-existing on the ground-state transition, the contributions can interfere leading to exciting new decay dy-

namics that change under a mirroring of the emitter.

The resulting decay rate of an emitter near a metallic structure can be decomposed into contributions to photons, plasmons, and losses. The decomposition revealed that particularly the coupling to optical modes with large wavevectors (plasmons, lossy modes) are affected by the breakdown, in correspondence with the notion of the dipole approximation being valid when $ka \ll 1$.

We have seen that the decay dynamics depend sensitively on the amount of intermixing of the dipolar and the mesoscopic moment. The decay dynamics are also very dependent on the sign of the ratio $\Lambda/\mu$, which can be used to control the coupling, especially to optical modes with large wavevectors. A calculation of the decay dynamics of a mesoscopic quantum dot near a silver mirror confirmed these effects in a simple structure. The effects are suspected to be much more pronounced in optical environments that are more complicated, where the inclusion of the mesoscopic moment could dominate the result. These results suggest that the engineering of nanophotonic structures for increased light-matter interaction should incorporate a model for extended emitters. Rephrased more generally: the co-engineering of the emitter and the structure could be adopted as a new design principle for pursuing enhanced light-matter interaction. The important experimental task of determining the mesoscopic moments for real quantum dots will be the subject of Chapter 4.

# Chapter 4

# Strongly modified plasmon-matter interaction with mesoscopic quantum emitters

In this chapter we present time-resolved spectroscopic measurements on quantum dots in three different but intricately related nanophotonic structures. Firstly, a study of quantum dots placed at controlled distances to a GaAs/air interface allows us to extract the intrinsic radiative and non-radiative rate of the quantum dots. Secondly and thirdly, we study the quantum dots at controlled distances to a GaAs/silver interfaces for two different orientations of the quantum dot. Near these silver mirrors, the resulting decay rates deviate from dipole theory in a manner that unambiguously provide the experimental proof of the mesoscopic nature of the quantum dot. The experimental data are compared to the model presented in Chapter 3 for decay dynamics of mesoscopic emitters and the mesoscopic moment, $\Lambda_{j,n}$, of the quantum dots is extracted.

The chapter is organized as follows. First, we motivate the experiments in Section 4.1, before we outline the sample fabrication in Section 4.2 and present the experimental method in Section 4.3. Then, in Section 4.4 the central results on the GaAs/silver interfaces are presented. In Section 4.5, they

are compared to the theoretical model introduced in Chapter 3, which allow us to extract the intrinsic mesoscopic moment of the quantum dots. In Section 4.6 we theoretically investigate the effect of the extracted mesoscopic moment on the coupling to plasmonic modes on a silver nanowire which have much larger field gradients resulting in strongly modified decay dynamics. Finally, we rule out a number of alternative mechanisms for the observed effects in Section 4.7 and present microscopic models for the mesoscopic moments in Section 4.8, before we present our conclusions in Section 4.9.

## 4.1 Motivation

Semiconductor quantum dots provide an essential link between light and matter in emerging fields such as light-harvesting [61, 62], all-solid-state quantum communication [63], and quantum computing [13]. Quantum dots are excellent single-photon sources [28] and can store quantum bits for extended periods [64] making them promising interconnects between light and matter in integrated quantum information networks [65]. To this end the light-matter interaction strength must be strongly enhanced using nanophotonic structures such as photonic crystal cavities [41] and waveguides [66] or plasmonic nanowires [20, 67, 68, 69]. So far it has been assumed that quantum dots can be treated just like atomic light emitters, where the spatial properties of the wavefunction can be safely ignored.

An essential advantage of all-solid-state emitters compared to, e.g., atomic emitters or molecules, is that they can be positioned deterministically and remain stationary [30]. This makes quantum-dot-based nanophotonic devices a promising technology for scalable many-qubit systems [70]. Presently, it becomes clear that quantum dots in nano-structures lead to a number of surprises distinguishing them from atomic systems, including the recent observations of very broadband radiative coupling in cavity quantum-electro-dynamics [41] and self-tuning of quantum dot nanolasers [71]. In this chapter we present the first experimental observation of a novel mechanism to enhance the interaction between light and matter induced by the mesoscopic size of quantum dots. It gives rise to a strongly modified radiative decay, that is tailored by the size and shape of the quantum dot electron-hole wavefunctions, and can be used as a resource to dramatically enhance the coupling of quantum dots to plas-

monic nano-structures. The efficient coupling of single emitters to plasmonic nano-structures is currently being investigated intensely for various applications within nanophotonics and quantum optics [72, 73] enabling highly efficient single-photon sources [19, 68, 74], single-photon transistors [20], and subwavelength plasmon lasers [75, 76]. In all these applications it is essential to understand and enhance the interaction between light and matter, which is the essence of the work presented in this chapter.

## 4.2 Sample fabrication

We have fabricated two samples which we name *the direct structure*, and *the inverted structure*. The nomenclature will be explained in the following. The inverted structure was also subjected to optical experiments before the final step of silver deposition (to be explained) was performed, hereby functioning as a third sample. The fabrication procedure described in this paragraph is outlined in Fig. 4.1 which can serve as a visual aid to the following text.

We use the same quantum-dot containing semiconductor wafer for both the direct and the inverted samples thus ensuring that there is no difference in the quantum-dot properties between the two samples. The semiconductor wafer was grown by molecular-beam epitaxy with the following layers from bottom to top: A GaAs substrate, a 50 nm AlAs sacrificial layer, a 623 nm GaAs buffer, 2.13 monolayers of InAs, and a 302 nm capping layer of GaAs. The InAs quantum dots are grown using the Stranski-Krastranov method on the (001) GaAs substrate, resulting in a quantum dot density of 250 $\mu m^{-2}$. Before evaporation of an optically thick (200 nm) silver mirror onto the sample we define a series of 32 terraces with a nominal spacing of 10 nm so that the distance to the silver mirror is varied from 0-310 nm.

For the direct sample the terraces are etched into the 302 nm GaAs capping layer, through a series of UV-lithography and wet-etching steps, using the method of Ref. [31]. For details see Appendix D. Optical access to the quantum dots is achieved by selective etching of the sacrificial AlAs layer and subsequential epitaxial lift-off of the layers above, which are then bonded to a transparent sapphire substrate.

The inverted sample is fabricated by first performing the epitaxial lift-off moving the top layers onto an intermediate PMMA-coated silicon substrate.

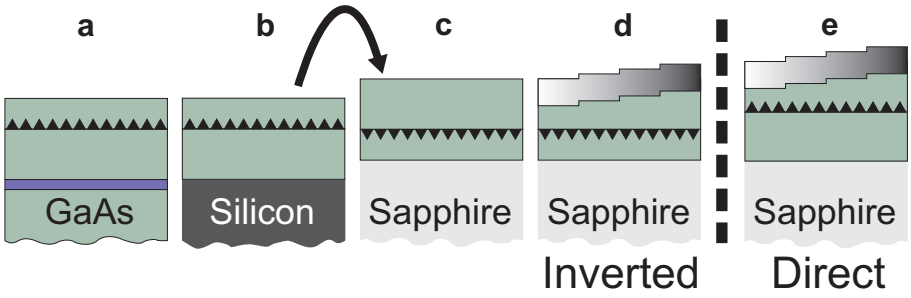


*Figure 4.1: Outline of the sample fabrication. The quantum dots are indicated with triangles, and the surrounding GaAs is indicated by the green color.* **a**, *The unprocessed wafer with a sacrificial AlAs layer (blue).* **b**, *The result of the epitaxial lift-off onto a intermediate silicon substrate.* **c**, *The wafer has been flipped upside down and transferred to a transparent sapphire substrate.* **d**, *The finished inverted sample with terraces and thick silver mirror.* **e**, *The finished direct sample for comparison.*

Hereafter, the top layers are transferred to a SU-8 coated sapphire substrate and bonded upside down, see Fig. 4.1 for a schematic presentation of the fabrication. After removal of the PMMA layer by oxygen plasma ashering, the terrace fabrication and silver evaporation continues as for the direct structure. The resulting distances to the quantum dots are measured using a combination of secondary ion mass spectroscopy of the initial wafer and surface profiling after terrace fabrication.

## 4.3 Experimental method

The decay dynamics of quantum dots are investigated by performing time-resolved single photon counting experiments on sub-ensembles of quantum dots emitting at the same wavelength. To this end the samples were placed in a closed-cycle cryostat and kept at a temperature of 16 K. The quantum dots were excited with a Ti:sapphire laser that emits picosecond pulses at a repetition rate of 76 MHz. The laser was tuned to 1.45 eV, which corresponds to absorption in the wetting layer. The power was adjusted so as to only populate the ground states of the quantum dots ($\sim$ 0.1 excitons/quantum dot/pulse). The spontaneously emitted light was collected with a lens and afterwards imaged

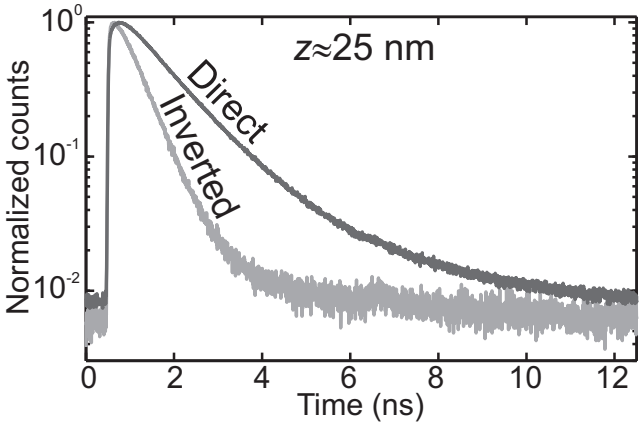


*Figure 4.2: Typical normalized decay curves. Both curves are for quantum dots positioned* $\sim$ 25 nm *from a silver mirror, but with two opposite orientations relative to the silver mirror as resulting from the direct and inverted structures.*

onto a monochromator in which the inhomogeneously broadened spontaneous-emission spectrum from the quantum dots was spatially dispersed. A narrow slit was used to select a narrow band (2.6 meV) of the spectrum centered at 1.204 eV (1030 nm). This corresponds to a low energy in the inhomogeneously broadened quantum dot spectrum (A typical spectrum is shown in Fig. 2.1), which together with the weak pumping conditions ($\sim$ 0.1 excitons/quantum dot/pulse) ensures that excited states from quantum dots with a lower ground-state energy do not contribute to the selected emission. The collected and spectrally seperated emission was then measured with a fast avalanche photo diode for time-resolved measurements. An outline of the experimental setup is shown in Appendix E.

Examples of the resulting decay curves are shown in Fig. 4.2. They can be fitted with a bi-exponential model and the fast decay rate can be extracted as discussed in Chapter 2. Note that we probe an ensemble of quantum dots, which are placed in the same optical environment and all emit photons at the same energy. This method averages out properties stemming from irregular single quantum dots, making it well-suited for investigations of general quantum dot properties.

The decay rates of quantum dots near a GaAs/air interface are well-described

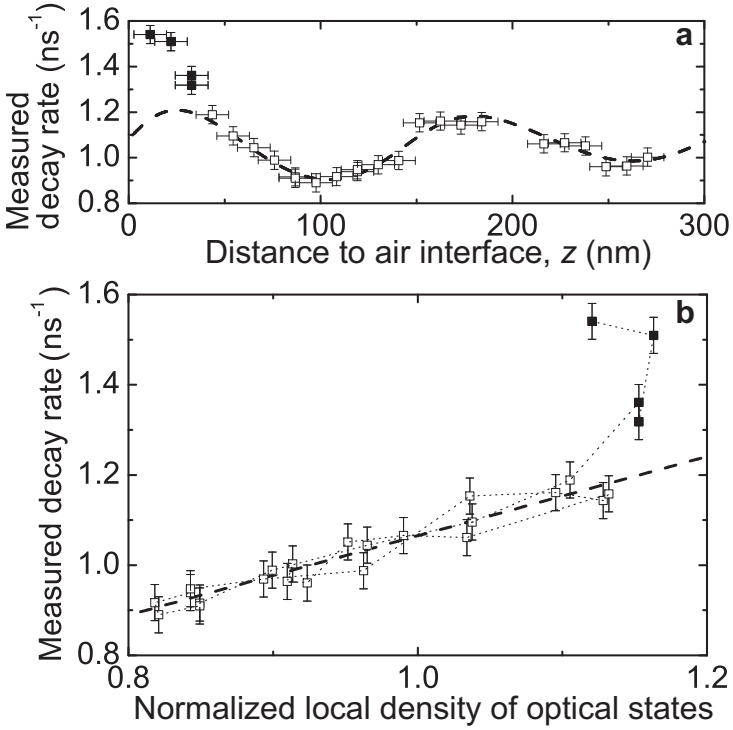


*Figure 4.3: Measured decay rates near a GaAs/air interface. The measured decay rates are plotted versus the distance to the interface (***a***) and versus the normalized density of optical states (***b***) for easy comparison with theory. In both plots the dashed line indicate the same fit to the data, the data points shown as solid squares ($z < 33$ nm) have been excluded from the fitting procedure.*

by dipole theory [29, 31]. In dipole theory the rate of decay is directly proportional to the density of optical states as described in Chapter 2. The decay rates of quantum dots was measured for a series of controlled distances to the GaAs/air interface, see Fig. 4.3a. The local density of optical states near the interface can be calculated exactly, whereby we can extract the intrinsic radiative $\Gamma_{\mathrm{rad}}$ and non-radiative $\Gamma_{\mathrm{nr}}$ decay rates of the quantum dots through a linear fit

$$\gamma_{\mathrm{QD}}(z) = \frac{\rho_{\mathrm{GaAs/air}}(z)}{\rho_{\mathrm{GaAs}}}\Gamma_{\mathrm{rad}} + \Gamma_{\mathrm{nr}}. \tag{4.1}$$

Here, $\rho_{\mathrm{GaAs/air}}(z)/\rho_{\mathrm{GaAs}}$ is the normalized density of optical states as introduced in Chapter 2, and $\gamma_{\mathrm{QD}}$ is the measured decay rate of the quantum dot. The experimental results are shown in Fig. 4.3 including the linear fit to the data. The resulting fitting parameters are $\Gamma_{\mathrm{rad}} = (0.88 \pm 0.06)$ ns$^{-1}$ and $\Gamma_{\mathrm{nr}} = (0.19 \pm 0.05)$ ns$^{-1}$. This corresponds to a quantum-dot quantum efficiency $\mathrm{QE} = \Gamma_{\mathrm{rad}}/(\Gamma_{\mathrm{rad}} + \Gamma_{\mathrm{nr}}) = (82 \pm 8)\%$.

Very close to the interface, i.e. for distances closer than 33 nm, we observe a faster decay rate than expected from dipole theory, see Fig. 4.3a. A similar deviation was also observed in Ref. [29] were it was described as being caused by a lossy layer at the surface. Like in Ref. [29] we have excluded these deviating data points in our fitting procedure.

From the fitted $\Gamma_{\mathrm{rad}}$ we can calculate the value of the dipole moment $\mu_x$ (defined in Chapter 3) using the method presented in Ref. [29] resulting in $\mu_x = 9.0 \times 10^{-25}$ kg m s$^{-1}$. With this knowledge of $\Gamma_{\mathrm{rad}}$ and $\Gamma_{\mathrm{nr}}$ we can calculate the expected dipole decay dynamics in other structures without any additional free parameters (see Eq. (4.1)), provided we can calculate the local density of optical states. This is crucial for the unambiguous interpretation of the following experiments.

## 4.4 Experimental proof for the breakdown of the dipole approximation

The breakdown of the dipole approximation is here demonstrated as deviations from dipole theory in the quantum dot decay rates when the quantum dots are placed near a silver mirror. Studying two samples with opposite quantum dot orientations lets us test the prediction from Chapter 3, which states that the decay dynamics depend on the quantum dot growth direction relative to the silver mirror.

Figure 4.4a illustrates the physical system under consideration: quantum dots are placed at a distance $z$ below a silver mirror and the electromagnetic field associated with the surface-plasmon polariton resonance at the metal surface is varying over the extension of the quantum dots. The quantum dots are standard-sized ($\sim 20 \times 20 \times 6$ nm$^3$) extended emitters. After excitation, the quantum dots trap single electrons and holes, see Fig. 4.4b, which recombine through different channels with the following rates: excitation of plasmons $\gamma_{\mathrm{pl}}$,

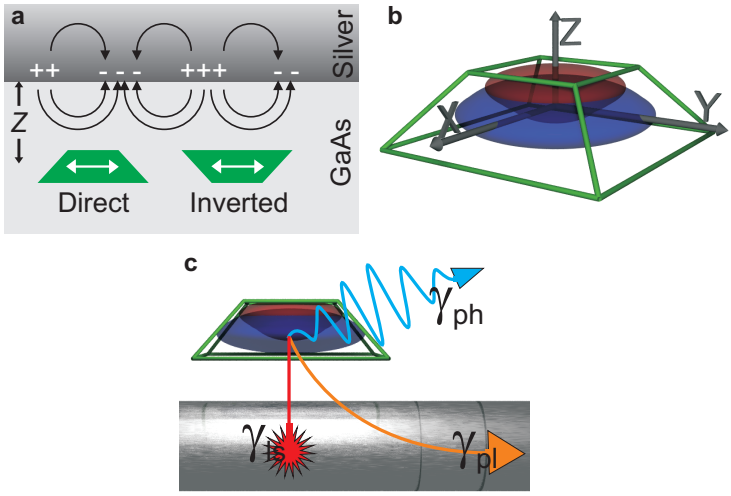


*Figure 4.4: Mesoscopic quantum dots in plasmonic nano-structures.* **a**, *Sketch of the studied systems (not to scale). Quantum dots (green trapezoids) are placed a distance $z$ below a silver mirror. The orientation of the in-plane dipole moment, indicated by the white double-arrow, is the same in the direct and inverted sample. The plasmon polariton mode is indicated by field arrows and surface charges (+ and −) as discussed in Chapter 2. The field amplitude of the plasmon decays exponentially away from the interface with a change in the electric field over the extension of the quantum dot.* **b**, *Boundaries of a quantum dot (green frame) with the spatially extended electron- (blue) and hole- (red) wavefunctions indicated inside.* **c**, *Sketch of a quantum dot placed near a metallic structure. The quantum dot can decay by emitting a photon ($\gamma_{\mathrm{ph}}$), by exciting a propagating plasmon ($\gamma_{\mathrm{pl}}$), by coupling to lossy modes in the metal ($\gamma_{\mathrm{ls}}$), or by intrinsic non-radiative recombination ($\Gamma_{\mathrm{nr}}$) (not shown).*

spontaneous emission of photons $\gamma_{\mathrm{ph}}$, non-radiative losses in the metal $\gamma_{\mathrm{ls}}$, or intrinsic non-radiative recombination in the quantum dots $\Gamma_{\mathrm{nr}}$, see Fig. 4.4c. The impact of the mesoscopic quantum dot size on the radiative coupling to plasmonic nano-structures can be precisely assessed by employing a nanophotonic structure with well-understood optical properties. Here we employ a silver mirror with quantum dots positioned at precise distances from the surface,

whereby the effects of emitter and environment can be unambiguously separated. This approach is, presently, not possible in more complex structures like photonic crystals [42] or near plasmonic nanowires [68].

The optical environment at the quantum dot positions can be precisely assessed near the silver mirror, as it does not depend on the in-plane position of the quantum dots but only on the distance to the interface. Quantum dots have been described as having a truncated pyramid shape [77] with the apex pointing in the growth direction, see Fig. 4.4b. Our first sample (the direct structure) is fabricated such that the quantum dot apices are pointing towards the silver mirror, and the second sample (the inverted structure) is fabricated such that the quantum dot apecis are pointing away from the silver mirror, as shown in Fig. 4.4a. Investigating the two different orientations of the quantum dots relative to the silver mirror, allows us to prove the breakdown of the point-emitter description.

For each orientation of the quantum dots we have measured the decay rates, $\gamma_{\mathrm{QD}}$, versus distance to the silver mirror, see Fig. 4.5. We are thus repeating the famous Drexhage experiment from 1970 [40], with the addition of the two different orientations of the emitter and the modification that here we are studying quantum dots. A point-dipole source would radiate identically in the direct and inverted structures, as indicated in Fig. 4.4a, and the expected decay rate for such an emitter is shown in Fig. 4.5 utilizing our findings from above, i.e., $\Gamma_{\mathrm{rad}}$ and $\Gamma_{\mathrm{nr}}$.

We observe that for short distances ($z < 100$ nm) to the silver mirror the measured decay rates deviate significantly from the point-dipole theory, i.e., significantly slower and faster quantum dot decay dynamics are observed for the direct and inverted structures, respectively, compared to the expectations for a dipole emitter. We will in the following argue that these deviations originate from the mesoscopic nature of quantum dots as discussed in Chapter 3.

The deviations from dipole theory are observed only for quantum dots positioned closer than $\sim 100$ nm to the silver mirror, which equals the length scale of the plasmonic penetration depth into the GaAs substrate. The observed variations in decay rate directly illustrate that the mesoscopic character of the quantum dots strongly influences the coupling to plasmons and can be employed as a resource to either suppress (direct structure) or promote (inverted structure) the excitation of plasmons.

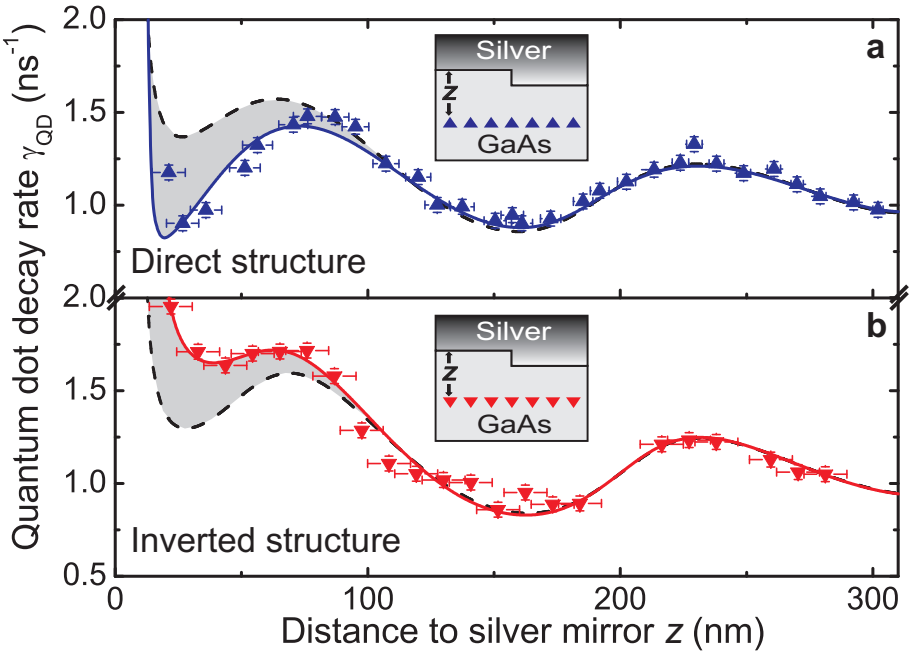


*Figure 4.5: Observation of the breakdown of the dipole approximation. Measured decay rates of quantum dots as a function of distance to the silver mirror for the direct (**a**) and inverted (**b**) structure at a wavelength of $\lambda = 1030$ nm. The dashed curves are the predicted variation for a point-dipole emitter. The solid curves show the theory for a mesoscopic emitter, which are found to match the experimental data very well. The insets show the orientation of the quantum dots relative to the silver mirrors for the two structures. The error bars on both rates and positions represent one standard deviation and are deduced from repeated measurements.*

## 4.5 Comparison to theory beyond the dipole approximation

The measured decay dynamics can be understood by comparing them to the theory developed in Chapter 3 for the decay of mesoscopic emitters. As we will see the comparison allows us to extract the mesoscopic moment of the quantum dots, and to identify the coupling to the plasmonic modes as the cause for the breakdown of the dipole approximation.

The model developed in Chapter 3 states that the decay rate of a mesoscopic emitter can be put on the simple form

$$\gamma_{\mathrm{QD}}(z) = \gamma_{\mathrm{pd}}(z) + \gamma_{\mathrm{me}}(z), \tag{4.2}$$

where $\gamma_{\mathrm{pd}}(z)$ is the familiar point-dipole contribution which depends on the transition dipole moment proportional to $\mu_x = \langle \Psi_{\mathrm{h}} | \hat{p}_x | \Psi_{\mathrm{e}} \rangle$, and $\gamma_{\mathrm{me}}(z)$ is the first-order mesoscopic contribution, which is also characterized by the mesoscopic moment $\Lambda_{z,x} = \langle \Psi_{\mathrm{h}} | \hat{p}_z \hat{x} | \Psi_{\mathrm{e}} \rangle$, in the following denoted $\mu$ and $\Lambda$, respectively.

In Chapter 3 we argued that both $\Lambda_{z,x}$ and $\Lambda_{x,z}$ gave non-zero results for quantum dots, wherefore both should be used in describing the measured decay dynamics. In the studied geometry of quantum dots near a silver mirror, we find that the coupling to plasmonic modes is the main reason for the breakdown of the dipole approximation. This leads to $\Lambda_{z,x} = \Lambda$ giving the dominating contribution to the modification of dipole decay dynamics, wherefore only this term is considered in the following. This argument is presented in detail in Appendix G.

The mesoscopic decay rate $\gamma_{\mathrm{me}}(z)$ depends not only on $\Lambda$ but also on the optical field gradient, which is large for plasmonic modes (in Appendix G we elaborate on the effect of the gradient on the breakdown of the dipole approximation). The two contributions to the decay rate in Eq. (4.2) combine coherently and can therefore either add or subtract depending on the specific nanophotonic structure surrounding the quantum dot, as was observed for the direct and inverted mirror structures in the data of Fig. 4.5. This novel effect has no counterpart in atomic systems, where the higher-order interactions between light and atoms are restricted by selection rules, i.e., co-existence of the first higher-order- and dipole transitions is prohibited by the symmetry of the

atomic potential. Here, we experimentally observe that for quantum dot emitters the higher-order processes can modify the ground state transition due to the mesoscopic nature of the wavefunctions thereby enhancing the light-matter interaction strength significantly.

The theory developed in Chapter 3 models the experimental data of Fig. 4.5 very well for both the direct and inverted structure. From our comparison with theory we can extract the intrinsic values $\Lambda/\mu = (10.9 \pm 1.6)$ nm for the direct structure and $\Lambda/\mu = (-7.2 \pm 0.9)$ nm for the inverted structure through a fit where the ratio $\Lambda/\mu$ is the only free parameter. From these we can extract the experimental values $\Lambda = (9.8 \pm 1.4) \times 10^{-33}$ kg m$^2$ s$^{-1}$ and $\Lambda = (-6.5 \pm 0.8) \times 10^{-33}$ kg m$^2$ s$^{-1}$ for the direct and inverted structures, respectively, from the experimental value of $\mu_x$ obtained in Section 4.3. The extracted values do not grow for quantum dots closer to the interface, where the plasmonic field is larger, but is an intrinsic property of the emitter. The result of excluding the innermost points in the fitting procedure is shown in Appendix G. The observed change of the sign of the fitted $\Lambda$'s, stems from the opposite orientation of the quantum dots relative to the plasmonic field and constitutes the tell-tale of the mesoscopic effects.

From our comparison with theory, we can also extract the rate of decay into the specific decay channels allowing us to precisely dissect the cause for the breakdown of the dipole approximation. We use the measured decay rates $\gamma_{\mathrm{QD}}(z)$, $\Gamma_{\mathrm{rad}}$, and $\Gamma_{\mathrm{nr}}$, and the calculated decay rates $\gamma_{\mathrm{pl}}(z)$, $\gamma_{\mathrm{ph}}(z)$, and $\gamma_{\mathrm{ls}}(z)$, as found by the decomposition explained in Chapter 3, for a mesoscopic quantum dot with $\Lambda/\mu$ as given by our fitting values. The rate of decay into a specific channel, e.g. into plasmons, is then extracted as

$$\gamma_{\mathrm{pl}}^{\mathrm{ex}}(z) = \gamma_{\mathrm{QD}}(z) - \Gamma_{\mathrm{rad}} \times (\gamma_{\mathrm{ph}}(z) + \gamma_{\mathrm{ls}}(z)) - \Gamma_{\mathrm{nr}}. \tag{4.3}$$

That is, by subtracting from the measured total decay rate, the intrinsic non-radiative recombination rate and the calculated normalized decay into photons and lossy modes multiplied by the intrinsic radiative recombination rate.

In Fig. 4.6a, the extracted $\gamma_{\mathrm{pl}}^{\mathrm{ex}}(z)$ is plotted versus distance to the mirror for both the direct and inverted structures. A pronounced difference in the plasmon excitation rate by a factor of eight is observed between the two structures. In contrast, the spontaneous-emission rate of photons $\gamma_{\mathrm{ph}}^{\mathrm{ex}}(z)$ (Fig. 4.6b) is similar for the two structures. These observations can be explained from the fact that plasmon modes give rise to strong electric field gradients near the silver

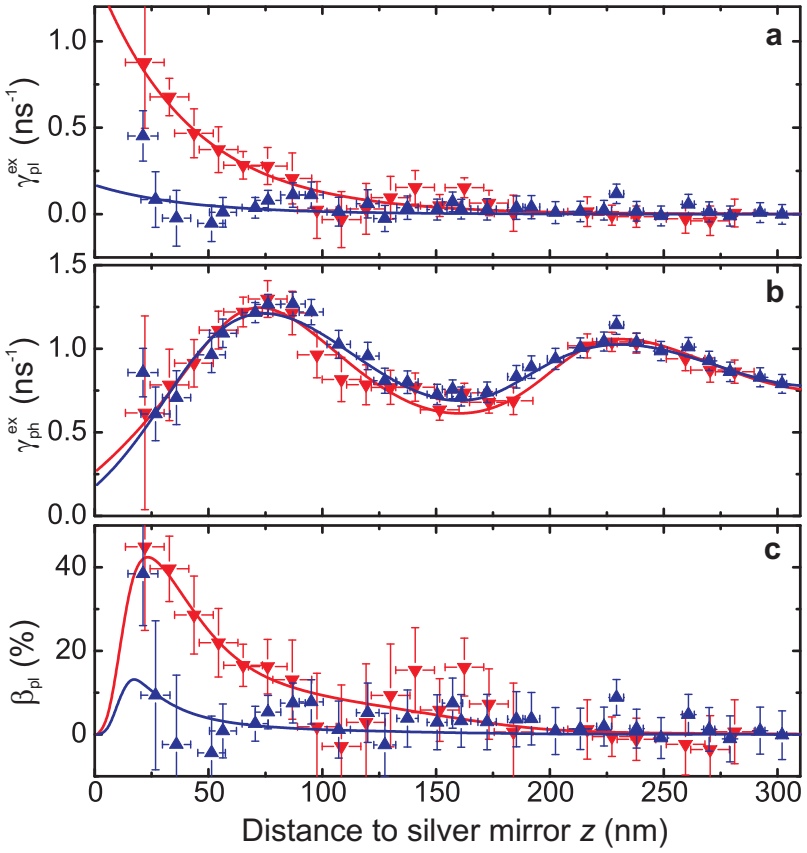


*Figure 4.6: Influence of mesoscopic effects on different decay mechanisms. The decay rate of quantum dots to plasmons $\gamma_{\mathrm{pl}}^{\mathrm{ex}}$ (**a**) and photons $\gamma_{\mathrm{ph}}^{\mathrm{ex}}$ (**b**), and the plasmon generation efficiency $\beta_{\mathrm{pl}}$ (**c**) as a function of distance to the silver mirror. Red ▼ and red curves are experimental data and theory for the inverted structure, respectively, while the blue ▲ and blue curves are the equivalent for the direct structure. The error bars on both rates and positions represent one standard deviation, as deduced from repeated measurements.*

mirror, thereby enhancing the influence of the mesoscopic quantum dot effects. We note that the extracted mesoscopic and point-dipole contributions to the plasmon excitation rate are of equal magnitude. As a result the mesoscopic contribution is so pronounced that the applied first-order perturbation theory is pushed to the limit of validity, which could account for the slight difference in the magnitudes of the fitted $\Lambda$'s between the two datasets. The figure-of-merit of a quantum plasmonic device is the $\beta$-factor expressing the probability that a quantum dot excites a single plasmon: $\beta_{\mathrm{pl}}(z) = \gamma_{\mathrm{pl}}^{\mathrm{ex}}(z)/\gamma_{\mathrm{QD}}(z)$, which is plotted in Fig. 4.6c. The $\beta$-factor is strongly enhanced due to the mesoscopic effects reaching 40 % for the inverted sample as opposed to 13 % for the direct sample where it is suppressed. The result for a pure dipole is 34 %. We emphasize that the modified decay rates discussed here are obtained in a very simple nano-photonic structure. These observations, thus, illustrate the potential of using the intrinsic mesoscopic properties of quantum dots in combination with careful engineering of the electromagnetic environment to strongly enhance the coupling to plasmons.

Due to the different thicknesses of the buffer and capping layers, the resulting distances to the sapphire substrate are different for the direct and inverted samples, see Fig. 4.1(d,e). This gives rise to a small difference between the decay rates as a function of distance to the silver mirror in the two samples, which can be seen by comparing the dashed curves in Fig. 4.5, or more easily in Fig. 4.6b. The result of the distance to the backside sapphire on the decay dynamic is shown in detail in Appendix F.

## 4.6 Mesoscopic quantum dots coupled to a metallic nanowire

The plasmonic modes on metallic nanowires are tightly bound to the structure, which results in plasmonic modes with very large field gradients. The coupling of dipole emitters to these have been proposed as an efficient method to harvest the decay of a quantum emitter for use in single-photon sources and transistors [19, 20, 68, 69]. Here we theoretically investigate the potential of mesoscopic quantum dots for improving plasmon-nanowire-based single-photon sources, as we study the decay dynamics of mesoscopic quantum dots placed close to a nanowire as shown in Fig. 4.7b.

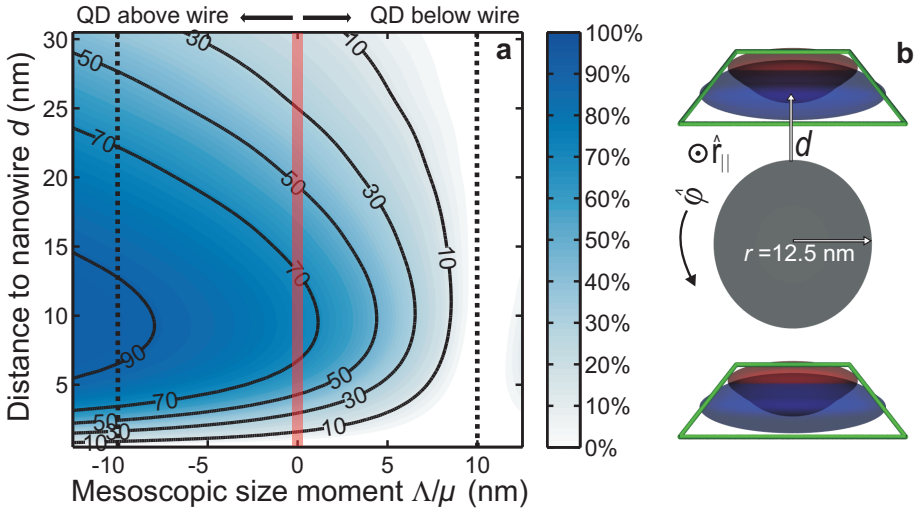


*Figure 4.7: Calculated efficiency of a nano-plasmonic single-photon source employing mesoscopic emitters.* **a**, *Plasmon generation efficiency* $\beta_{\mathrm{pl}}$ *for a quantum dot in GaAs near a silver nanowire with radius* $r = 12.5$ nm *for varying distance* $d$ *and* $\Lambda/\mu$. *We have used a constant* $\gamma_{\mathrm{ph}}$ *and included* $\gamma_{\mathrm{ls}}$ *for a point dipole. The dotted lines indicate* $\Lambda/\mu = \pm 10$ nm, *corresponding roughly to the values extracted for real quantum dots in this chapter.* **b**, *Sketch of a nanowire with* $r = 12.5$ nm *and mesoscopic quantum dots positioned a distance* $d$ *from the surface. The dipole moment of the modeled quantum dot is oriented at* $45°$ *to both the parallel* ($\hat{r}_{\parallel}$) *and azimuthal* ($\hat{\phi}$) *directions. Negative or positive* $\Lambda/\mu$ *corresponds to a quantum dot positioned above or below the nanowire, respectively.*

For a small wire radius (here $r = 12.5$ nm) only a single strongly confined plasmon exists inducing very strong field gradients, i.e., mesoscopic quantum dot effects are expected to be very pronounced. We note that structures of this size can be fabricated by electron beam lithography [78] or chemical synthesis [79]. We calculate $\gamma_{\mathrm{pl}}(z)$ versus distance to the nanowire for varying ratios of $\Lambda/\mu$, corresponding to quantum dots with various amount of mesoscopic character, and for two different orientations of the quantum dot relative to the nanowire.

The coupling efficiency of the quantum dot to the plasmonic mode is cal-

culated for an emitter with a quantum efficiency of unity, i.e., $\Gamma_{\mathrm{nr}} = 0$. The decay rate into photons $\gamma_{\mathrm{ph}}$ is assumed to be constant and equal to the value in homogenous GaAs. The plasmon mode was calculated by a finite-element method [80] implemented in COMSOL, and the corresponding Green's function constructed, according to the relation developed in Appendix B as used in Appendix G. This is a feasible approach since only a single plasmon mode exists for the studied wire of radius $r = 12.5$ nm. Based on these simulations, $\gamma_{\mathrm{pl}}$ is extracted including the effect of a spatially extended quantum dot with $\Lambda \neq 0$. The decay rate into lossy modes $\gamma_{\mathrm{ls}}$ is calculated from an analytical expression for a point dipole near a nanowire [67, 81]. We note that we have multiplied the expression stated in these works with a factor of two, as there is an error in the calculations. This is confirmed through comparison to calculations using dyadic Green's functions and work by Barnett and Loudon [82].

The decay dynamics is different for the in-plane dipole moment oriented parallel to the wire and along the azimuthal direction. In an experimental setting where a superposition state of the two linear dipole orientations is created in the quantum dot, multi-exponential decay would result. Here we have modeled a single dipole-moment that is oriented at 45 degrees to both the azimuthal and parallel direction of the wire, and a corresponding mesoscopic moment, (see Fig. 4.7b), to give an average effect on the modified decay efficiencies.

The resulting plasmonic coupling efficiency $\beta_{\mathrm{pl}}$ is shown in Fig. 4.7a. Very strong dependencies on both distance and $\Lambda/\mu$ are observed. For a fixed distance of $d = 10$ nm we find that the efficiency for a point-dipole source (i.e. $\Lambda = 0$) is $\beta_{\mathrm{pl}} = 75\%$. This number can be enhanced substantially to $\beta_{\mathrm{pl}} = 92\%$ assuming the experimentally extracted value of $\Lambda/\mu \approx$ -10 nm for a quantum dot placed near the nanowire, see Fig. 4.7b. On the other hand the same quantum dot oriented upside-down relative to the nanowire ($\Lambda/\mu \approx +10$ nm) would only couple weakly to the nanowire with $\beta_{\mathrm{pl}} < 1\%$. Even stronger (weaker) modifications of the decay rate result for quantum dot dipole moments oriented parallelly (azimuthally) to the nanowire, these results are presented in Appendix H. For the case presented here, i.e., with the quantum dot positioned directly underneath or above the wire, the azimuthal component of the excited state do not couple to the nanowire, but as soon as the quantum dot is shifted to the side, coupling becomes possible, the result is shown in Appendix H. All the calculations are performed at $\lambda_0 = 1030$ nm similar to the

wavelength studied in the experiments presented in this chapter. These results demonstrate the very pronounced effects of including the naturally occurring mesoscopic contribution to the quantum dot decay and that it can be employed for improving the efficiency of plasmonic nanophotonic devices.

## 4.7 Ruling out alternative mechanisms for the observed effect

When observing a new physical effect it is essential to be able to rule out that the observations could be dominated by alternative mechanisms. The key tell-tale for the mesoscopic effects signifying the breakdown of the dipole approximation on a dipole allowed transition, is the change from enhancement to suppression of the rate when reversing the quantum dot orientation. In the following we explicitly explain why alternative mechanisms can be ruled out.

The excitation in a quantum dot can be lost by tunneling of either the trapped electron or hole out of the quantum dot. Such non-radiative processes may be enhanced near surfaces [29], but can only increase the measured total decay rate. Therefore, non-radiative processes cannot explain the measured suppression of the decay rate observed for the direct sample and can be ruled out.

It has been predicted that the hole wavefunction partly resides in the light hole band [83], which results in an out-of-plane component of the dipole-moment. However, also a dipole oriented out-of-plane would radiate identically in the direct and inverted structure, and thus would not explain our observations.

The decay rate of a quantum dot treated in the dipole approximation is proportional to the square of the overlap of the envelope functions for the confined electron and hole. By applying an electric field over the quantum dot along the growth direction, it is possible to change the aforementioned overlap and thereby the decay rate of the quantum dot, which is a direct consequence of the quantum-confined Stark shift [84]. An unavoidable impurity background doping of the semiconductor along with the silver mirror forms a Schottky barrier with such a build-in electrical field. The background ion impurity density of the used wafer has been measured to be $N = 4.3 \times 10^{21}$ m$^{-3}$ from mobility measurements on a two-dimensional electron gas grown in the

molecular beam epitaxy chamber. From this number we can calculate the typical length scale of the surface-induced electric field into the GaAs as [85] $d = \sqrt{2V_b\epsilon_0\epsilon_d/(e^2N)} = 462-580$ nm , where $V_b = 0.71-1.12$ eV is the barrier height [86], $e$ is the elementary charge, and $\epsilon_d$ is the permittivity of GaAs. Thus any resulting surface electric field would extend 5-6 times further than the length over which we observe deviations from dipole theory, and we can therefore rule out the Stark effect as explanation of our data. The conclusion is confirmed by calculating the resultant electric field ($0-24$ kV/cm) in our structure [85]. Previous experiments with applied electric fields have shown that no significant change in the decay rate occurs in this range [87]. Notably no enhancement of the decay rate is observed, which is the case for the inverted structure in our experiment. Finally, the typical dominant impurities in GaAs are carbon defects giving rise to a p-doped GaAs. From measurements of the static dipole moment of quantum dots [84] it is found that the hole is situated above the electron for zero applied electric field, which together with a Schottky barrier with p-doped GaAs results in a reduction of the decay rate in the inverted structure in conflict with our measurements.

## 4.8 Microscopic models for the mesoscopic moments

In Chapter 3 we argued for the existence of the mesoscopic moments through symmetry considerations, and in Section 4.5 we found that we could extract the size of the mesoscopic moment through comparison to the experimental data. Until now, a discussion on a microscopic model that can explain the size and origin of the mesoscopic moments have been lacking. In this section we will outline our efforts in constructing two microscopic models for $\mu$ and $\Lambda$ to account for the quantum dot properties that we extracted through the fitting procedure detailed above. A full account is given in Appendix I.

We are investigating the properties of the mesoscopic moment

$$\Lambda_{z,x} = \langle\Psi_h|\hat{x}\hat{p}_z|\Psi_e\rangle = -i\hbar\langle\Psi_h|x\nabla_z|\Psi_e\rangle, \tag{4.4}$$

which is dependent on the gradient of the electron and hole wavefunctions in the $z$-direction (growth direction). The wavefunctions can be decomposed in

envelope and Bloch functions $|\Psi\rangle = |F(\mathbf{r})\rangle|u(\mathbf{r})\rangle$ which contain the structure on the length scale of the quantum dots and crystal unit-cell, respectively [37].

The first microscopic approach studies the effect of gradients in the envelope functions $\langle F_h|\nabla_z|F_e\rangle$, where the envelope functions are given as solutions to an effective mass equation [31]. The material composition throughout the quantum dot is assumed uniform in the model, which results in electron and hole wavefunctions that are not offset relative to each other, and are fairly symmetric along the growth axis. Such envelope functions are not representative of real quantum dots [84] and do not yield large mesoscopic moments. We therefore artificially introduce an offset to increase the effect on $\langle F_h|\nabla_z|F_e\rangle$. Even so, the resulting mesoscopic moments are found to be multiple orders of magnitude smaller than the values extracted from the comparison to the experimental data in this chapter.

The second microscopic approach studies the effect of a sharp transition in the periodicity of the Bloch functions. Such transitions are occurring in real quantum dots as the two constituting semiconductors, InAs and GaAs, have different lattice constants. The resulting mesoscopic moment is in this case much larger than found in the first approach, and is found to scale with the height and width of the quantum dots such that flat and wide quantum dots have large mesoscopic moments. Numerically, the resulting moments are within one order of magnitude from the extracted mesoscopic moments.

The simple microscopic models suggest that the mesoscopic moment is linked to the size and shape of the quantum dots, and that it is dependent on the crystalline structure - i.e., not just determined by the envelope functions. More modeling should be done, incorporating the material composition and crystalline structure throughout the quantum dots, before a microscopic understanding of the measured mesoscopic moments can be fully realized.

## 4.9 Conclusion

We have experimentally demonstrated that the interaction between quantum dots and plasmonic nano-structures can be understood only by taking the mesoscopic size of the quantum dots into account. Furthermore, we demonstrated an excellent agreement with the theory presented in Chapter 3 allowing us to extract the mesoscopic moment and in turn make predictions of strongly

modified decay dynamics of quantum dots near metallic nanowires.

From our comparison with theory we observed that the quantum dots can excite plasmons eight times more efficiently depending on their orientation due to their mesoscopic character. Either enhancement or suppression of the rate of plasmon excitation is observed depending on the geometry of the plasmonic nano-structure in full agreement with the theory presented in Chapter 3. This discovery has no equivalence in atomic systems and paves the way for novel nano-plasmonic devices that exploit the extended size of quantum dots as a resource for increasing the plasmon-matter interaction strength.

Our findings are expected to be of relevance also for dielectric nano-strucures, where mesoscopic quantum dot effects are anticipated to be of importance for spontaneous-emission control in photonic crystals [42], dielectric-waveguide single-photon sources [66], and in cavity quantum-electro-dynamics [41] in particular when employing large quantum dot emitters that currently are investigated for their prospective large oscillator strength [47, 88]. Our conclusions are surprising since the point-dipole approximation has been uncritically adopted in the literature to describe light-matter interaction between quantum dots and nano-photonic structures. Importantly, the mesoscopic effects are very pronounced, and may be employed as a resource to enhance light-matter interaction, which is required in a diverse range of scientific fields ranging from quantum information science and quantum computing to energy harvesting devices.

# Chapter 5

# Fabrication and characterization of plasmonic gap waveguides

Plasmonic waveguides combine the data speed and bandwidth available with light and the miniaturization possible with electronic circuits, to form a new regime where light signals are guided below the diffraction limit. Thus the potential of plasmonic waveguiding is enormous and the unfolding of the implications will be exciting to watch. Recently new light has been shed on plasmonic waveguiding, illuminating their potential for coupling to quantum emitters. The field enhancement and dispersion of plasmonic modes on metallic nanowires allow for strong plasmon-matter interaction [19, 81], which can be used to make efficient single-photon sources [19] and single-photon transistors [20]. Thus, plasmonic waveguides provide a novel route towards quantum computing, and importantly, a route that does not rely on the tuning of emitters and structures to sharp resonance conditions.

The coupling of a quantum emitter to a plasmonic nanowire was demonstrated by Akimov *et al.* in 2007 [68]. In this work colloidal quantum dots were coupled to chemically synthesized nanowires. Plasmonics modes on single crystalline chemically synthesized nanowires have longer propagation distances than those on nanowires produced by electron-beam lithography and metal

evaporation, which are polycrystalline. This was shown in a study were short nanowires of both types were employed as plasmon resonators [89]. Chemically synthesized nanowires are easy to fabricate [90], but they are suspended in liquid and spun onto the substrate of use, with no control over position and orientation as a result. The synthesization process result in a distribution of radii and lengths of the nanowires. At the present stage of synthesization technique it is therefore unfeasible to scale such a technology towards more complicated networks of emitters and waveguides, and it is therefore, to this end, required to use a more well-controlled fabrication method.

In this chapter we will present our progress on producing nano-scale plasmonic waveguides by electron-beam lithography on top of a wafer containing stationary quantum dots. There have been substantial progress in position-controlled growth of self-assembled quantum dots [30], which after growth remain stationary within their host semiconductor wafer. Furthermore, the resolution of modern electron-beam-lithography systems is constantly increasing, extending the validity of Moore's "law". Thus, a technology combining position controlled growth of stationary quantum emitters with electron-beam-defined metallic structures is therefore readily scalable to complex emitter and waveguide networks. The smoothness of metallic structures defined by metal-evaporation, which is the common method used in connection with electron-beam lithography, is not presently as good as that of synthesized metallic structures. However, recent progress with template stripping, reactive ion etching and focussed ion beams [91] have improved the smoothness of controllably fabricated metal structures tremendously. Another approach is to synthesize large single crystalline flakes of silver [92] or gold [93], and then subsequently define structures in these by using focussed ion-beam writing. With these methods the smoothness of fabricated metallic structures is approaching the theoretical limit for a perfectly flat surface, thereby closing the propagation length gap to chemically synthesized metallic structures. The obstacles for coupling emitters to lithographically produced nanowires therefore seems surmountable. The control over size, shape, and position of plasmonic waveguides combined with the scalability of waveguide-networks and position-control of solid-state emitters makes it feasible to pursue strongly coupled plasmon-matter systems as a scalable technology.

The chapter is organized as follows: First the physical principle enabling a

strong coupling of an emitter to one-dimensional metallic wires is discussed in Section 5.1. For efficient coupling to quantum dots utilizing a planar fabrication technology, the polarization of the guided mode must match the orientation of the quantum dot dipole moment. This point leads to the proposal of a plasmonic gap waveguides as a favorable plasmonic waveguide geometry. In Section 5.2 we present the fabrication procedure for plasmonic gap waveguides, along with the challenges encountered in the development of this. Finally, in Section 5.3, measurements of single quantum dots coupled to the fabricated plasmonic gap-waveguides are presented, before we in Section 5.4 give our conclusions for this chapter.

## 5.1 One-dimensional plasmonic structures for increased plasmon-matter interaction

The available coupling strength of a dipole emitter to a guided mode on an one-dimensional structure can be described by Fermi's golden rule [21], which originates from first order perturbation theory. The rule states that the decay rate of an emitter can be given as

$$\gamma = 2\pi g^2(\mathbf{r},\omega)D(\omega), \tag{5.1}$$

where $g$ is the light-matter interaction strength which depends on position $g = \mathbf{d}\cdot\boldsymbol{\xi}(\mathbf{r})/\hbar$ with $\mathbf{d} = \langle e|e\mathbf{r}|g\rangle$ being the transition dipole moment between the ground state $|g\rangle$ and the excited state $|e\rangle$. Furthermore, the normalized field strength $\boldsymbol{\xi}(\mathbf{r}) = \sqrt{\hbar\omega/(\epsilon_0 V_{\text{eff}})}\mathbf{E}(\mathbf{r})/E_{\max}$ describes the field enhancement through the effective mode volume $V_{\text{eff}}$, and the electric field vector $\mathbf{E}(\mathbf{r})$ which is normalized to the maximum value $E_{\max} = \max(\mathbf{E}(\mathbf{r}))$. Finally, $D(\omega)$ is the density of states. In the following we will describe a subsets of states associated with the guided modes in one-dimensional systems, as this describes the physical systems that we will investigate.

### 5.1.1 One-dimensional density of states

For one-dimensional systems the density of states is given by $D(\omega) \propto (L/(2\pi))v_g^{-1}$ [34], i.e, it is proportional to the inverse of the group velocity $v_g$, where $L$ is a quantization length. This is a general property of coupling to one-dimensional

structures. To achieve strong interaction, the dispersion of the guided mode should, thus, be tailored to yield a slow group velocity. This would result in a large density of states, and with this, strong interaction with an emitter.

We briefly discuss the dispersion relations of guided modes in two other one-dimensional systems, before exclusively concentrating on the plasmonic systems:

1. Dielectric cylinder: The wavenumber $k$ of the fundamental guided mode of a dielectric cylinder drop towards zero as the radius of the cylinder shrinks [81]. Dielectric cylinders therefore do not support modes which allow for efficient coupling to an emitter, as the group velocity is related to the wavenumber through $v_g^{-1} = \partial k/\partial\omega$.

2. Linedefects in photonic crystals. Waveguides defined as linedefects in a photonic crystal can be engineered to support a propagating mode with very low group velocity [94] by careful control over hole pitch and radii. Photonic crystal waveguides are thus promising candidates for the efficient coupling of a single emitter to a propagating mode [66, 95].

As we shall see the advantage of the plasmonic structures is a very broadband working range, and an amplification of the coupling mechanism by the subwavelength confinement of light, a property unique to metallic structures.

### 5.1.2 Group velocity of plasmonic modes on metallic nanowires

For a small nanowire radius only a single mode exists. The group index of this fundamental plasmonic mode scales inversely with the radius of the nanowire, diverging for very small wire radii [19, 81]. The resulting group velocity can thus be very low with a strong interaction to a single quantum emitter as a consequence.

The group-velocity scaling with wire radius can be described in simple terms by considering the inductance of a thin wire [96]. A current running through a wire results in a certain energy per unit length induced by the magnetic field, this is given by $u_{\mathrm{mag}} = lI^2/2$, where $I$ is the current and $l$ is the inductance per unit length. On the other hand, the kinetic energy of the electrons per unit

length is

$$u_{\mathrm{kin}} = (\frac{1}{2}mv^2)n\pi R^2 = \frac{1}{2}\frac{m}{e^2 n\pi R^2}I^2 = \frac{1}{2}l_{kin}I^2, \tag{5.2}$$

where $m$ is the electron mass, $n$ the electron density per unit length $\pi R^2$ the cross-section area with $R$ the radius of the wire and $v$ the velocity of the electrons. We have introduced $l_{\mathrm{kin}} = m/(e^2 n\pi R^2)$ to relate the associated energy to the current $I = (\pi R^2 n)ev$. For sufficiently small wires $R \to 0$ the kinetic inductance $l_{\mathrm{kin}}$ will dominate the effective inductance $l_{\mathrm{eff}} = l + l_{\mathrm{kin}}$. This means that the energy in a very thin wire no longer is determined by the magnetic field, but by the kinetic energy associated with movement of electrons. The group velocity of the mode on a wire can be calculated from the inductance by using the theory of transmission lines. Here the group velocity is given by $v_g \propto (l_{\mathrm{eff}}C)^{-1/2}$, where $C$ is the capacitance per unit length which only depends weakly on the wire radius [96]. In the limit of small wires, the kinetic inductance dominates the total inductance and we can therefore conclude that the group velocity is proportional to the radius of the wire ($v_g \propto R$).

### 5.1.3 Coupling rate to plasmonic nano-structures

The rate of decay to a guided one-dimensional mode is determined by both the group velocity and the field enhancement, as given by Eq. (5.1). The field confinement in dielectrics is in general limited by diffraction, therefore the associated enhancement of the decay rate is small. In contrast to modes on dielectric waveguides, the plasmonic modes are bound to the metal interface and the mode-size shrinks along with the supporting structure. This yields a scaling of the modevolume given by $V_{\mathrm{eff}} \propto R^2$, where $R$ is the radius of the wire.

The scaling of the decay rate into the plasmonic mode on a cylindrical nanowire is, as consequence of the above arguments, given by $\gamma_{\mathrm{pl}} \propto R^{-2} \times R^{-1} = R^{-3}$ per insertion in Eq. (5.1). The arguments presented here also show that the group velocity and mode-size scaling is largely determined by the size of the waveguide, and thus give similar result for a small cylinder or a small rectangle [97].

We note that the associated coupling to plasmonic modes diverges for $R \to 0$. This scaling does not break down for small wires, but there are competing effects that constrain real devices. The scaling of the mode-confinement with

the wire radius implies that the emitter needs to be placed close to the nanowire in order to harvest the effect of the smaller wire size. The finite size of real emitters thus defines a practical limit on the coupling obtainable by reducing the wire radius [51]. Furthermore, the emitter can also couple to lossy modes that do not propagate. The coupling to lossy modes, in the limit of the emitter being very close to the wire, scales inversely with the distance to the wire surface cubed $\gamma_{\mathrm{ls}} \propto (\rho - R)^{-3}$ [82], where $\rho$ is the radial distance to the emitter from the center of the wire. This implies that the plasmon generation efficiency is optimal for a certain distance to the wire. Furthermore, the presence of metals and material interfaces provide additional routes for non-radiative loss of the excited state in the emitter, which could inhibit the practical implementations of strongly coupled emitter nanowire systems.

From Eq. (5.1) we see that the available decay rate also depends on the orientation of the dipole moment of the emitter, $\mathbf{d}$. A nanowire has cylindrical symmetry, therefore we consider the orientation of the dipole along the three fundamental directions, ($\hat{\rho}$, $\hat{z}$, and $\hat{\phi}$). For a dipole moment oriented along the azimuthal direction ($\hat{\phi}$) there is no coupling to the plasmonic mode, as determined by the symmetry of the wire. While there is a contribution from a dipole moment oriented parallel to the wire ($\hat{z}$), the dominant contribution is from a radially oriented ($\hat{\rho}$) dipole moment. The quantum dot electric-dipole moments are parallel to the surface of their host wafer. Deposition of nanowires on top of such a wafer therefore results in dipole moment orientation along $\hat{\phi}$ and $\hat{z}$ in the nanowire coordinate system. This orientation is not ideal for strong interaction, we will therefore pursue a different route towards achieving an efficient coupling by considering a different plasmonic waveguide design. We will here name these structures plasmonic gap waveguides, but they are also referred to as slot waveguides [98] in the literature. In these structures two thin slab waveguides are placed close to each other, thus defining a gap between these that supports a plasmonic mode, see Fig. 5.1. The polarization of this mode is such that it couples well to the available dipole moment orientation in quantum dots given the restrictions of planar fabrication technology, i.e. that the quantum dots are positioned below the waveguiding structures that are at the surface of the wafer. The modes on plasmonic gap waveguides have the added benefit, that they are confined more in the dielectric gap rather than in the metal, which improves the plasmon propagation length [99].

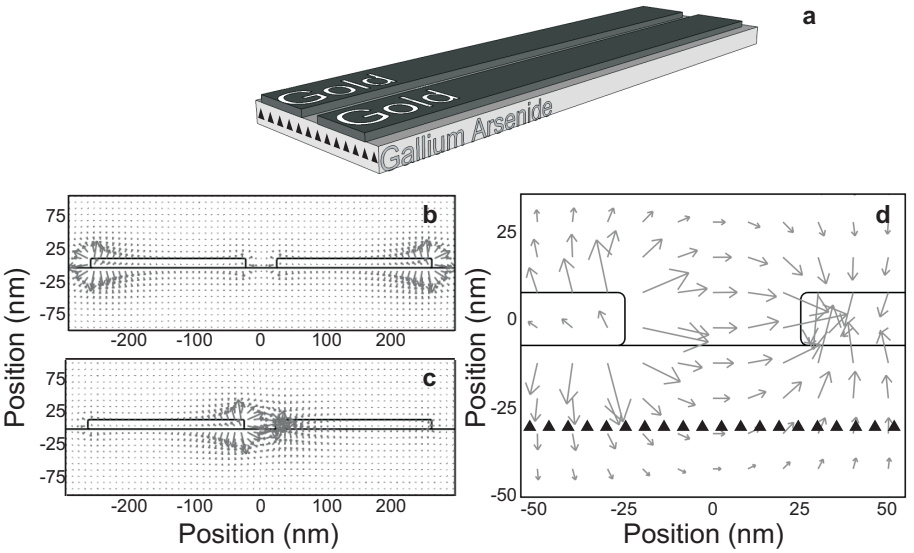


*Figure 5.1: The two fundamental field modes of a gap waveguide.* **a**, *Gold waveguides on GaAs with air as the top medium. The arrows in (***b**, **c**, **d***) indicate the strength and direction of the electric field.* **b**, *The separated mode, where the field predominantly is at the outer edges of the structure.* **c**, *The center mode where the field is predominantly in the center.* **d**, *Enlarged plot of the central region of* **c** *where the electric field is seen to be oriented horizontally under the center of the gap. The black triangles show the position of the quantum dots, which have their dipole moment in the wafer plane.*

For a cylindrical nanowire only a single mode exist for a small wire radius. However, for plasmon gap waveguides the number of guided modes is at least two and depends on the width of the two slabs of metal defining the gap. For small slabs the two supported modes are either localized in the gap or on the outer edge of the structure, see Fig. 5.1. In this chapter, we concentrate on the fundamental mode that is localized in the gap, as the coupling to this mode can be enhanced by reducing the mode volume. The mode volume scales with the area defined by the height of the metal slabs and the width of the gap, which means that small gaps allow for a very efficient coupling to nearby emitters. In Chapter 6 we will study the effect of varying different geometry parameters on the achievable coupling to a quantum emitter.

## 5.2 Fabrication of plasmonic gap waveguides

The subject of this section is the fabrication of plasmonic gap waveguides, emphasis is on producing gap waveguides with narrow gaps as these can provide the strongest coupling to emitters. Furthermore, consistency of the fabricated structures is important, as the ultimate goal is to be able to scale the procedure towards larger networks of photonic and plasmonic components.

The fabrication procedure consists of the following basic steps, see Fig. 5.2: growing the quantum dot wafer (a), spinning a thin layer of electron-beam resist (b), exposing a pattern in the resist with electron-beam (c), developing the exposed pattern (d), evaporating gold (e), and lift-off of unexposed resist and residual gold (f). This leaves a pattern of gold defined by the electron beam on the quantum dot containing GaAs wafer. In this section we will outline the process carried out to fabricate plasmon gap waveguides, and emphasize surprises and solutions along the way. A detailed fabrication recipe is given in Appendix D.

We aim at measuring the coupling of quantum dots to plasmonic gap waveguides for a range of emitter to wire distances, as well as for a range of wire geometries. To this end we prepared a quantum dot wafer with a series of terraces defining different distances to the underlying quantum dots. The terraces were formed by etching holes of controlled depths (tens of nanometers) into the wafer. The holes have the size $200 \times 500$ $\mu m^2$. The deepest of the 32 holes was $\sim 310$ nm with the underlying quantum dots residing 302 nm under the surface before the etch. We will denote this first sample S1. Series of waveguides are fabricated on each of the terraces. The first step in the waveguide process is to spin a thin layer of resist ($\sim$ 100 nm) on the wafer. The thickness of the resist is critical as the success of the electron beam writing relies on a balance between resist thickness and electron beam current. Additionally, we need the resist to be thin to facilitate the definition of small structures. We had therefore carefully calibrated the electron beam and resist spinning parameters.

### 5.2.1 Resist thickness on structured surfaces

When we measured the thickness of the spin coated resist on the terrace structured quantum dot wafer, we found that the resist had not formed an evenly thick layer. The resist was found to be too thick over the terraces, and had the

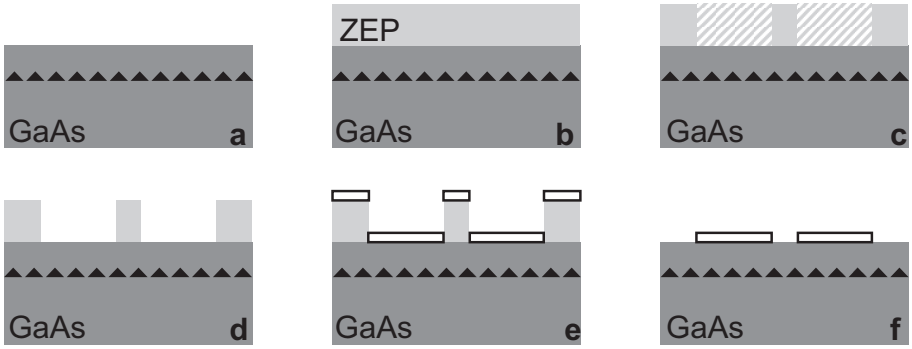


*Figure 5.2: Sketch of the basic process for defining nanoscale gold structures on a wafer containing quantum dots. Dark gray denotes GaAs and black triangles the embedded InAs quantum dots. The light grey is the electron beam resist (here we used ZEP), and patterned light grey indicates resist that has been exposed. Finally, white rectangles with black outlines are used for the evaporated gold.*

correct thickness over the rest of the wafer. To circumvent this problem, we etched away the wafer everywhere around the terrace structures. The result of which was that the holes defining the terraces were turned into terrace-pillars. The procedure was successful as the resulting thickness of a new layer of spin coated resist on top of the terraces now had the correct height for electron beam exposure. The exposure was then performed and the exposed resist developed.

The next step of the process is that metal is evaporated onto the entire structure in a low pressure evaporation chamber. Structures formed by metallic vapor deposition with a resulting height below ten nanometer, have been found to form connected clusters of gold, rather than a uniform surface. We therefore deposited 15 nm of gold which defines the height of the structures. This height was chosen as the smallest height that would yield nicely connected gold structures. We choose to form our structures with gold (as opposed to silver) as gold does not react fast with air, the trade-off with this choice is worse propagation properties due to the larger absorption in gold, as will be discussed in Chapter 6.

### 5.2.2 Wafer surface degradation

After gold deposition, we prepared a bath of solvent (AZ1165) which dissolves the resist allowing for a lift-off of unwanted gold from the sample. The efficiency of the solvent grows when it is placed in a heat bath. Thus we placed our sample in a heated bath of AZ1165 and found to our surprise that the solvent also attacked GaAs. The root-mean-square roughness of the GaAs after lift-off was found to be 5 nm, which should be compared to the roughness of the deposited metal which was 0.5 nm. The roughness of the deposited metal inherits the roughness of the underlying substrate, which shows that the roughness must have been introduced after metal deposition and therefore by the solvent. To further test this claim, we performed a test with two identical samples left overnight in heated and unheated baths of AZ1165. The results confirmed that, indeed, AZ1165 does attack GaAs. Consequently, all subsequent fabrication runs avoided heated AZ1165 completely and minimized exposure time to AZ1165 in general.

During our initial test of the electron beam dose, we found that the resulting exposure was very dependent on the dose. Backscattering from the substrate of the electron beam makes it difficult to fully expose two structures placed very close to each other without exposing the region in between. In order to have a higher yield of the process we therefore used four closely spaced electron beam doses for our samples. The resulting structures are shown in Fig. 5.3, excluding the lowest dose (Dose 1) which was so low that no metal was evaporated onto the substrate. The shown structures are all designed to have a gap width of 50 nm and the two sides should be 200 nm wide each. For Dose 2 the gap is 117 nm and the sides are 140 nm which is a result of the dose being too small. For Dose 3, which is the optimal dose in this study in terms of reproducing the design, we find the sides to be 188 nm and the gap to be 61 nm. Dose 4 results in 180 nm sides with a 70 nm gap. Note the small tapering of the gap near the end of the wire for Dose 4, see Fig. 5.3. Here, the gap shrinks to 20 nm, the tapering is found in most structures made with dose 4, and is most likely a proximity artifact of the electron beam writing.

The roughness of the first sample (S1) which is clearly visible in Fig. 5.3, unfortunately made the measurement of photoluminescence from the quantum dots unfeasible. We suspect that increased scattering from the surface is so pronounced that it is difficult to pump the underlying quantum dots, and fur-

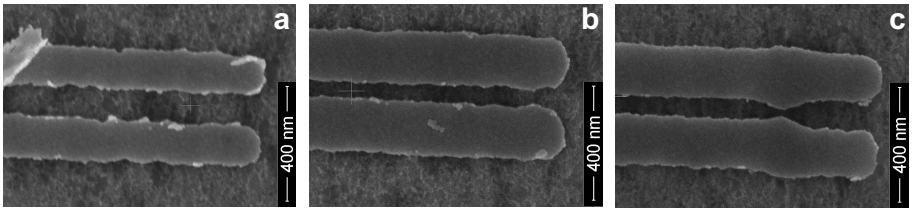


*Figure 5.3: Scanning electron beam micrograph of typical structures for 3 different doses of electron beam writer current. The surrounding GaAs is very rough as a result of leaving the sample in heated AZ1165. The structures are all designed to have a gap of* 50 nm *and wire width of* 200 nm. **a**, *Dose 2.* **b**, *Dose 3.* **c**, *Dose 4.*

thermore, that the emitted photons from the underlying quantum dots are scattered before they can reach our detector systems.

### 5.2.3 Sample with fewer and larger terraces

We decided to proceed with a simpler terrace design which incorporated 8 large $2 \times 2$ mm$^2$ terraces where the distance to the quantum dots is only varied over the interesting region for plasmonic coupling $0-80$ nm. Using a combination of UV-lithography and wet etching, two of these terrace samples were produced. We will denote these samples (S2). All process steps were thoroughly tested on dummy GaAs pieces before implementation on the final samples. Unfortunately, the metal deposition and subsequent lift-off was still found to vary from sample to sample resulting in unusable structures (S2).

### 5.2.4 Final sample design

We made a new sample design (S3), which had a lot of redundancy, allowing us to try the metal deposition and lift-off eight times. In this sample the distance to the quantum dots was kept at a single fixed distance of 25 nm.

The critical electron-beam writing can be assessed by atomic force microscopy and the resulting pattern written in the electron beam resist on S3 is shown in Fig. 5.4. We find that due to proximity effects the resist defining the gap degrades when the designed gap becomes small. In this sample there is still 57% of the resist height in the gap left for a designed gapwidth of 25 nm. The

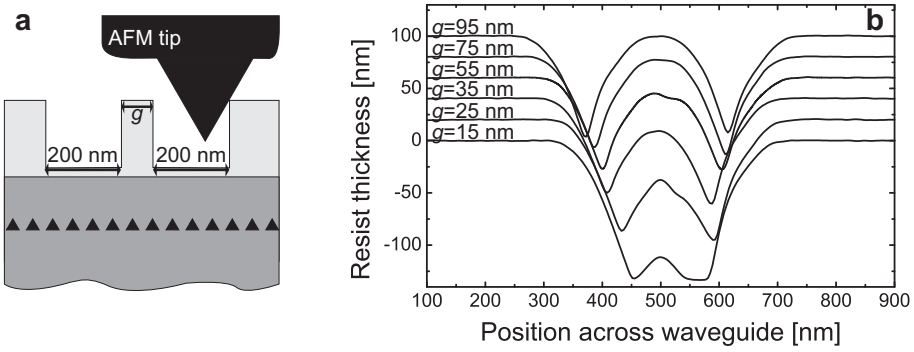


*Figure 5.4:* **a**, *Sketch of the designed resist profile and an AFM tip used to measure the profile. Gap structures with a gap-width of g are examined, and the side stripes are* 200 nm *wide.* **b**, *Measured resist profiles for a series of designed gapwidths, g. The height measurements are convoluted with the shape of the AFM tip which make the interpretation difficult. The height of the resist in the gap can, however, readily be obtained. Furthermore, the total resist thickness can be measured from* $g = 15$ nm *where the tip reaches a bottom plateau, which is the wafer surface.*

full resist thickness is 133 nm, as seen where the tip of the atomic force microscope reach the bottom plateau defined by the wafer for a designed gap width of 15 nm. After establishing that the resist had been properly exposed and developed, the sample was cleaved into eight pieces each containing four doses and a range of structural parameters. In this way we could attempt the metal deposition and lift-off eight times without changing any sample parameters.

To obtain consistent results for the metal deposition and subsequent lift-off, we prepared the surface of the sample immediately before metal evaporation. The surface was subjected to a short ashering and a deoxidation. The ashering removes any residue resist from the development, and as a biproduct forms an oxide layer which is afterwards removed by a deoxidation process. We have done tests with different rates of metal deposition and chose to work with 0.5 nm/s as this provided reasonable control over the deposition thickness and produced a good quality surface. The time that the sample is in the resist-solvent AZ1165, has been reduced to two hours, which give good results for our structures.

### 5.2.5 Fabrication results

The resulting sample (S3) was characterized with an atomic force microscope and a scanning electron microscope. Firstly, the roughness of the gold and GaAs was measured, resulting in root-mean-square roughness of 3.0 nm and 1.3 nm, respectively. The roughness of the metal can be seen in Fig. 5.6c. We note that these numbers are larger than the best values we have seen, which are around 0.7 nm for both metal and GaAs. Then we measured the actual height of the deposited gold which was found to be 16 nm - consistent with the designed height of 15 nm. We hereafter carefully investigated the structures using a scanning electron microscope, and found that we are able to successfully fabricate structures with a designed gap width of 35 nm, and that we obtain consistent results for designed gap widths of $> 65$ nm, e.g. as shown in Fig. 5.5.

The presented fabrication procedure (detailed in Appendix D), successfully yields plasmonic gap waveguides. The length of the waveguides can be controlled: We have fabricated waveguides of 2, 5, 10, 20, 30 μm lengths without changing any fabrication parameters to compensate for differences in the lengths. In Fig. 5.3 there is a tapering of the gap $\sim 300$ nm from the end of the waveguide. We believe that this is a proximity effect of the electron beam writing, suggesting that for structures of this length or shorter, the recipe should be altered. We note that this observed tapering also suggest a potential for using proximity effects to produce structures with very narrow gaps. In our work we have realized plasmonic gap waveguides with the following parameters:

| Height | Gap width | Strip widths | Roughness | Lengths |
|---|---|---|---|---|
| 16 nm | $50 - 100$ nm | $150 - 250$ nm | 3 nm | $2 - 30$ μm |

*Table 5.1: Parameters of successfully fabricated plasmonic gap waveguides.*

We have also tried to produce plasmonic gap waveguides with very wide side widths (few μm), as such structures would form an aperture only letting luminescence from quantum dots sitting below the gap emit photons into the detection path. For these structures the resist defining the gap was degraded too much to allow for a successful lift-off. We suspect that proximity corrections need to be employed to successfully expose such structures. For the slab waveguide widths of 150, 200, 250 nm we have achieved good results, as shown

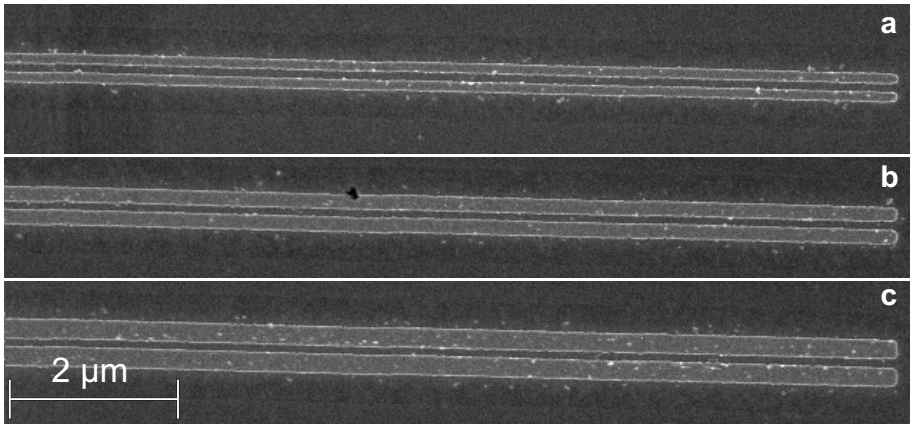


*Figure 5.5: Scanning electron micrographs of three gap structures that all have a designed gapwidth of* 65 nm. *We can consistently fabricate waveguides with such gap dimensions, and here we vary the width of the metal strips, which influences the number of guided modes as well as their properties. The shown structures have the width of the strips set to* 150, 200, *and* 250 nm, *in* **a**, **b**, *and* **c**, *respectively.*

in Fig. 5.5.

The width of the gap is found to be difficult to control as it is very sensitive to the proximity effects of the electron beam. Here we typically found the gap to be $\sim 10$ nm wider than the designed width. The structures with the smallest gap that we have successfully fabricated have a designed width of 35 nm as shown in Fig. 5.6b. When the gap becomes too small it is impossible to lift-off the metal over the gap. Such a partial lift-off is shown in Fig. 5.6a.

The height of the plasmonic structures is limited by the height of the resist which, in turn, needs to be low for producing narrow gaps, thus there is a trade-off between height and gap width. For our purposes we need a small waveguide height to increase the coupling, so we need not worry about this relation. With the presented fabrication procedure, a large variety of metallic structures can be made, allowing for a multitude of research studies. Here we focused on plasmonic gap waveguides, but the same fabrication procedure could readily produce grating structures, plasmonic waveguide taperings, or plasmonic antennas.

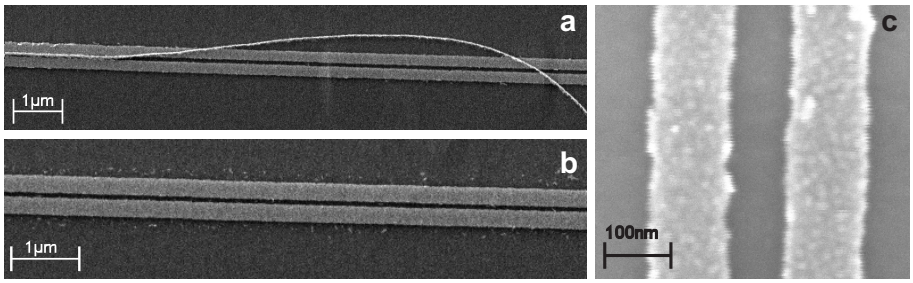


*Figure 5.6: Scanning electron micrographs of plasmonic gap waveguides.* **a**, *A partially successful metal lift-off.* **b**, *Very narrow plasmonic gap width measured to be* 50 nm. **c**, *Zoom in on the end of a plasmonic waveguide where the roughness of the metallic structures is clearly visible.*

## 5.3 Optical characterization of single quantum dots coupled to plasmonic gap waveguides

The aim of the fabrication was to produce waveguides for controlling the decay dynamics of quantum dots. In this section we present our results from the experimental investigations of single quantum dots coupled to a fabricated plasmonic gap waveguide.

The measurement system consists of a flow cryostat and a confocal microscope. An outline of the measurement system is given in Appendix E while we describe the basic experimental method here. A diffraction limited spot on the sample wafer is excited through a microscope objective by a pulsed Ti:sapphire laser. The density of quantum dots is high, $\sim 250\ \mu m^{-2}$, resulting in the excitation of a number of dots with each pulse. We can not control our detection position better than the excitation spot size, but we can study a single quantum dot by spectrally selecting the emission stemming from individual dots as shown in Fig. 5.7a. To this end, the spontaneous emission is collected with the same microscope objective and guided onto a monochromater, which is used to isolate the emission of single quantum dots. The spectrally filtered light is recorded with an avalanche photo diode to perform time-resolved measurements. In the experimental investigation presented in this section we measure on quantum dots that emit light near 920 nm.

Time-correlated single-photon counting experiments are firstly performed

on four different quantum dots positioned far away from the plasmonic gap waveguides. The quantum dots are thus positioned near a GaAs/air interface roughly 25 nm under the surface. The four resulting, and very similar, decay curves are shown in Fig. 5.7b. From these we extract a reference decay rate of $\gamma_{\mathrm{ref}} = (1.76 \pm 0.02)$ ns$^{-1}$. We note that the intrinsic $\Gamma_{\mathrm{rad}}$ and $\Gamma_{\mathrm{nr}}$ of these quantum dots are unknown. Instead we can assume the quantum efficiency to be similar to our finding from Chapter 4, i.e. $QE = 82\%$, and from the reference measurement, where the optical environment is well-known, extract the absolute rates. This approach is, however, compromised as the quantum dots are placed so close to the surface that we would expect coupling to lossy surface modes, as seen in Chapter 4.

After this initial characterization of the quantum dots, we turn our attention towards the coupled system. We have measured decay curves from a number of quantum dots near a plasmonic gap waveguide, i.e., the excitation spot is placed directly across the waveguide to measure on quantum dots placed either directly below the gap or near the waveguides. In Fig. 5.7c four representative decay curves are shown, two fast and two slow. The resulting decay rates are found to be 3.0, 2.8, 1.1 and 1.2 ns$^{-1}$ which is faster, faster, slower, and slower, than the reference decay rate, respectively.

Naively, we would expect the presence of the plasmonic gap waveguide to result only in faster decay rates. This is reasoned by the consideration that the plasmonic structures give rise to additional decay rates, i.e. coupling to guided modes and coupling to lossy modes. However, the presence of metals also give rise to a modification of the coupling to photons, which consequently could be weaker near a metal than near the GaAs/air interface thereby resulting in slower decay rates. Comparing the measured reference decay rates to our findings in Chapter 4, we observe that these are similar to the results for the studied GaAs/air interface at 25 nm from the interface, corresponding to the quantum dot to wafer surface distance. Furthermore, the slow decay rates observed near the waveguides correspond well to the slow decay rates near the silver mirror in the direct structure, where there is very weak coupling to plasmons.

In order to analyze the faster decay rates, we have calculated the coupling to the guided plasmonic modes for the specific structure. The results are shown in Fig. 5.8.

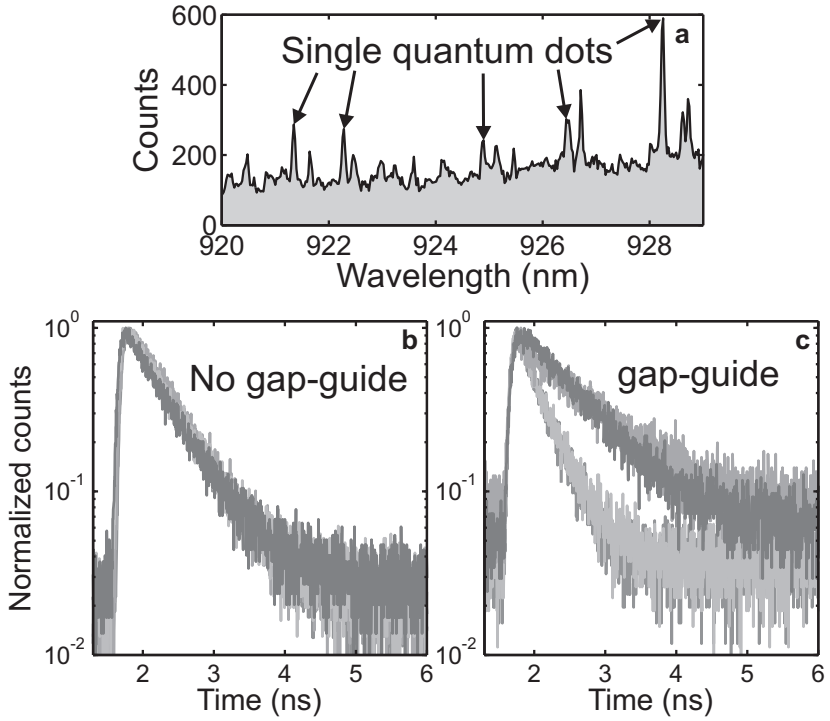


*Figure 5.7: Experimental results on the coupling of single quantum dots to plasmonic gap waveguides.* **a**, *Spectrum with clearly visible single quantum dot peaks, which can be investigated individually.* **b**, *Decay curves from four quantum dots far away from the waveguide. The curves are found to be very similar and serve as reference for the study of quantum dots coupled to the plasmonic structure.* **c**, *Decay curves from four quantum dots near the plasmonic waveguide. Quantum dots with faster and slower decay rates than observed in* **a** *are measured.*

The studied plasmonic gap waveguide consists of gold and has a height of $\sim 15$ nm and a gap width of $\sim 95$ nm as well as the width of the two strips being $\sim 250$ nm, see Fig. 5.8a. The quantum dots are situated 25 nm below the surface, and the two principal excited states are oriented along either $x$ or $y$. We have calculated the rate of decay into the guided plasmonic modes divided by the decay rate in a homogeneous medium for both dipole orientations and for different positions along the $x$-axis, from the center of the gap to underneath

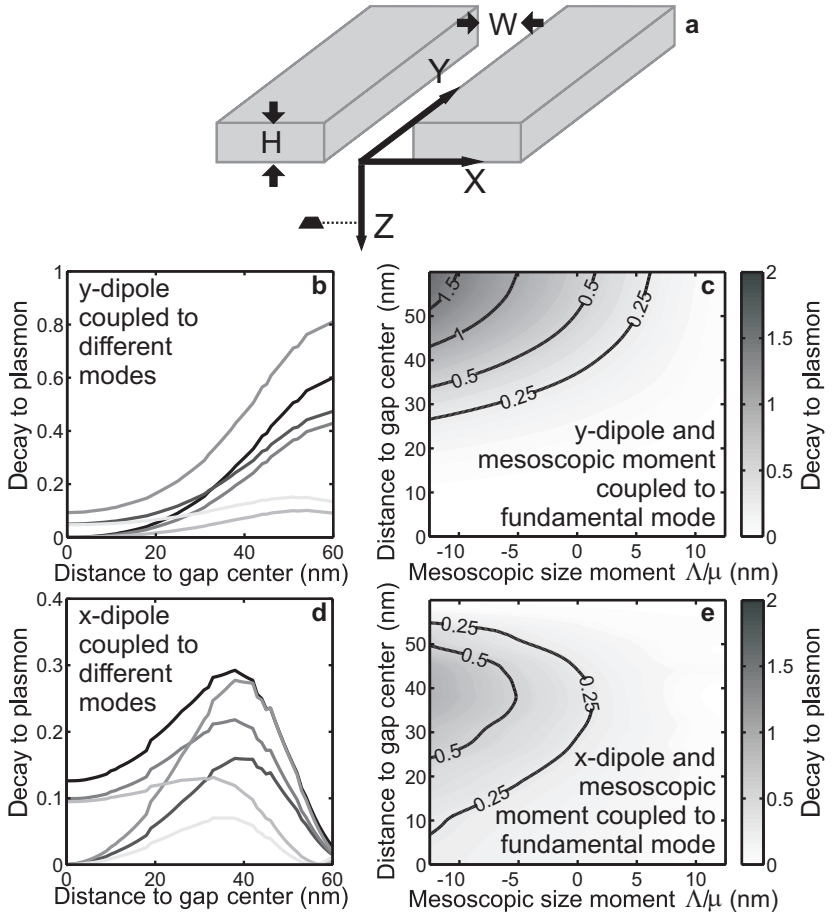


*Figure 5.8: Modeling of decay dynamics of mesoscopic quantum dots near a plasmonic gap waveguide. The two different dipole orientations give rise to different coupling rates to the guided modes.* **a**, *Sketch of the system with a quantum dot placed 25 nm below the bottom of the waveguide and shifted away from the center of the waveguide.* **b**, *Coupling of a dipole oriented along the $z$-axis to each of the six guided modes and for different position shifts (black line is the fundamental mode).* **c**, *Coupling of an excited state oriented along the $z$-axis to the fundamental mode for different position shifts and for different amount of mesoscopic character $\Lambda/\mu$.* **d,e**, *Same as* **b,c** *but for an $x$-oriented dipole and mesoscopic moment. For* **b**, **c**, **d**, *and* **e** *the coupling is given in units of $\Gamma_{\mathrm{rad}}$.*

one of the two sides. There are six different guided plasmonic modes in this structure. The result for a dipole emitter oriented along either axis is shown in Fig. 5.8(b,d), explicitly for the coupling to each of the six modes as function of position across the waveguide. We see that especially if the emitter is placed nearer the metallic strips then the coupling is substantially enhanced. For an excited state oriented along either axis, we also show the result for the coupling to the fundamental mode including the effect of a mesoscopic moment. The decay rate into the guided mode is substantially modified due to the mesoscopic moment, as shown in Fig. 5.8(c,e). Assuming a similar mesoscopic moment as extracted in Chapter 4 ($\Lambda/\mu \approx +10$ nm) we see that the effect is that of a diminished coupling to the fundamental plasmonic mode. In summary, the uncontrolled in-plane position of the quantum dots combined with their mesoscopic moments, and many different guided modes, make a range of measured decay rates consistent with theoretical predictions.

Furthermore, the coupling to lossy modes can be estimated by considering two limiting cases. Firstly, for an emitter 25 nm from a gold nanowire with a diameter of 15 nm, corresponding to the thickness of the waveguide, the coupling is calculated to be $\gamma_{\rm ls}/\Gamma_{\rm rad} = 0.35$. Secondly, for an emitter 25 nm from a gold mirror the coupling is found to be $\gamma_{\rm ls}/\Gamma_{\rm rad} = 0.15$. We therefore estimate that the coupling to lossy modes is responsible for no more than $0.35\ \Gamma_{\rm rad}$.

The fast decay can thus easily be explained by associating the coupling to the guided and/or lossy modes with it. Thus, we conclude that the presented measurements are consistent with our understanding of the system. These findings illustrate the problem of performing detailed experiments near complicated nano-structures. It is very difficult to separate the different decay mechanisms, as they are sensitively dependent on the in-plane position of the quantum dot, which is difficult to control. The modifications of the decay rate are small in the experimentally studied structure, which has a gap width of $\sim 95$ nm. In Appendix H we show the effect of including the mesoscopic moment and varying the position of a quantum dot near a gap waveguide with a gap width of 25 nm, resulting in much larger decay rate modifications.

An unambiguous proof of the coupling to plasmons would rely on the detection of light after it has propagated as a plasmon, and performing cross-correlation measurements between this and the direct emission from the cou-

pled emitter, as was done in Ref. [68, 74]. Such an approach is not feasible in the present system as the propagation length of the plasmons is on the order of the excitation spot size, which makes the spatial distinction between the direct and propagated light impossible. We will in Chapter 6 calculate, among other parameters, the propagation length for various plasmonic gap guide geometries and materials.

## 5.4 Conclusion

The efficient coupling of single quantum emitters to plasmonic waveguides relies on the scaling of the group velocity and modesize with the size of the structure. It is therefore a necessity to fabricate plasmonic waveguides with very small dimensions, to realize efficient coupling. In this chapter we have presented the fabrication process developed to this end. We found that we are able to fabricate plasmonic gap waveguides on GaAs with gap widths down to 50 nm.

We also presented experimental data on the coupling of single quantum dots to a plasmonic gap waveguide with a gap width of $\sim 95$ nm. The decay rates of nearby quantum dots were found to be modified by the presence of the waveguide. A comparison with theory revealed that the measured results are within the expected range of decay rates. In order to conclude further on the coupling dynamics of single quantum dots to plasmonic waveguides, either statistically analysis of a large ensemble of single dot measurements should be performed or the direct demonstration of a single coupled quantum dot, e.g. by means of cross-correlation measurements between direct and propagated emission must be demonstrated. The comparison thus highlighted the difficulty in interpreting the decay dynamics of nano-structured systems where the position of the emitter is unknown.

# Chapter 6

# Plasmonic modes in low-dimensional systems

Plasmonic modes are bound to their supporting metallic structures which enables the shaping of the optical mode directly by the dielectric and metallic structures. Thus, the plasmonic mode is defined not only by optical properties of the supporting materials, but also by the geometry of these. The study of plasmonic modes in low-dimensional systems and emitters coupled to these involves interesting physical phenomena as well as engineering challenges. Importantly, the coupling to one-dimensional systems provides a novel route towards single-photon sources [19]. An excitation of an emitter is converted to a plasmon mode that propagates in a predefined direction through a fast and efficient coupling. In this way the challenging task of harvesting the excitation of an emitter is overcome in a efficient and fast way. After the capture of the excitation by a propagating plasmon, the plasmon can be converted to a single photon. The coupling to plasmon polariton modes does not rely on tuning to resonance conditions like in cavity quantum-electro-dynamics [41], and to a lesser extent in photonic crystal waveguides [66]. Due to the losses in the plasmonic modes it is, however, required that the propagating plasmon is quickly transformed to a mode that does not decay as fast. There are many different ways to transfer the propagating plasmon to a lossless mode, e.g., evanescent transformation of the mode, evanescent transfer to a dielectric waveguide, or coupling via periodic gratings. All of these mechanisms present challenges of

their own, that need to be met in order to realize a plasmon-based single-photon source. Here we will mainly address the initial coupling to the plasmonic mode of various structures, and only briefly discuss the transformation of this to a photon in the outlook of this chapter.

The rate of coupling of a single emitter to round [81], rectangular [97], and gap [69] plasmonic waveguides have previously been discussed in the literature. In these studies there has been very little focus on the effect of the surrounding dielectric ($\epsilon_{\mathrm{GaAs}} \approx 12$), which changes the propagation of-, and coupling to- the plasmonic mode significantly. In this chapter we therefore study the scaling of these essential parameters (coupling rate, propagation length) with the geometry of the waveguides, and the permittivity of the surrounding dielectric. The aim is both to make general observations regarding material systems as well as to study the specific structure discussed in Chapter 5.

This chapter is organized as follows. First we discuss the material properties of gold and silver, which are the metals relevant for this thesis. Then we introduce the model framework for this chapter, and discuss the effect of high-index dielectric materials on the properties of plasmonic modes at a simple dielectric-metal interface in Section 6.1. Then in Section 6.2, we discuss the effect of confinement of the plasmonic mode to a two dimensional metal-dielectric-metal slab structure, which serve as an intermediate platform for studying plasmonic modes in metallic gap waveguides in Section 6.3. Lastly, we discuss the outlook for plasmon-assisted single-photon sources, in Section 6.4, both using gap waveguides and also using alternative plasmonic structures. Finally, the conclusions are presented in Section 6.5.

## Material properties

Plasmonic modes are dependent on both the properties of the supporting metal and the surrounding dielectric. Here, we will briefly discuss the optical properties of the two metals important to this work, namely silver and gold. We will use the optical constants of noble metals measured by Johnson and Christy [100] in 1972. Their measurements cover a broad range of wavelengths ($\lambda = 400 - 2000$ nm), and their results are shown in Fig. 6.1. The region relevant for the quantum dots discussed throughout this thesis is $\lambda = 900 - 1100$ nm. There is strong drive towards producing quantum dots that emit at longer wavelengths, hereunder the telecommunication wavelength

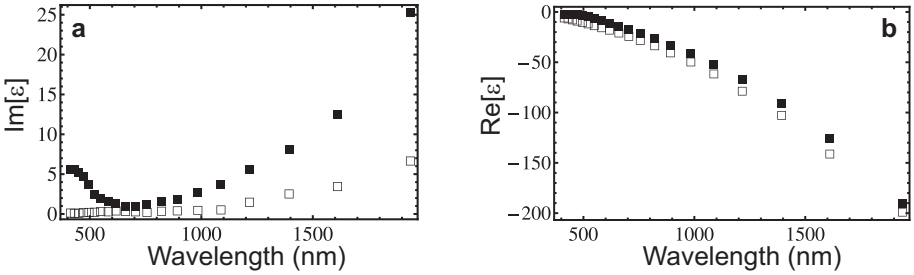


*Figure 6.1: Real (**b**) and imaginary (**a**) part of the permittivity of gold (filled squares) and silver (open squares) from Johnson and Christy [100].*

$\lambda = 1550$ nm, and recently substantial progress has been made to meet this goal [101]. We will therefore in this chapter discuss a wider range of wavelengths than that being emitted by an inhomogenously broadened InAs quantum dot ensemble.

In Fig. 6.1 the permittivities of silver and gold are decomposed into their real and imaginary parts. We note that the real part of the permittivities of silver and gold are very similar. As we will see later, this implies that a range of properties are similar for plasmonic modes on gold and silver structures. Furthermore, the imaginary part of the permittivities of silver and gold are quite different, which implies that particularly the propagation distance of plasmonic modes on silver and gold differ. The imaginary part of the permittivity determines the absorbtion in the metal, which means that plasmons on silver will propagate further than their gold counterparts. Thus, silver has better optical properties than gold, but the fast rate of oxidation of silver surfaces [102] imposes challenges to the fabrication. There is therefore a trade-off to be considered when fabricating plasmonic structures of silver or gold, between short propagation distances and degradation of the structures due to oxidation.

In this chapter we will include the optical properties of the metals for different wavelength as given in Fig. 6.1. We will, however, use the permittivity of the dielectric as a model parameter, without considering the dispersion of these, even though this can be considerable, e.g., for GaAs [103, 104].

## 6.1 Surface plasmon polariton properties in high-index dielectrics

In this section we will calculate the properties (dispersion, confinement and propagation length) of surface plasmon polaritons on a metal-dielectric interface. We will use gold and silver as the metal, and calculate the properties of the plasmonic mode as function of the permittivity of the dielectric.

We extract the properties of the plasmonic modes by constructing the Green's function for the metal-dielectric interface as an integral over in-plane wavevector $k_{\|}$, see Appendix A and Appendix B. The integrand in the Green's function has a singularity associated with the plasmonic mode in the region $k_{\|} > k_d$ where the subscript $d$ denotes that this is the wavevector in a homogenous dielectric with permittivity $\epsilon_d$. The plasmonic-mode pole in the integrand is proportional to $(k_{\|} - k_{\mathrm{pl}})^{-1}$ where $k_{\mathrm{pl}}$ is a complex-valued number with a relatively small imaginary part, as given by

$$\mathbf{G}_{\mathrm{pl}}(\mathbf{r}_0, \mathbf{r}_0; \omega) \propto \int_{k_{\|} \approx k_{\mathrm{pl}}} dk_{\|} \frac{1}{k_{\|} - k_{\mathrm{pl}}}. \tag{6.1}$$

By fitting a pole of this form to the integrand of the Green's function (see Appendix A), we can extract the plasmonic wavevector, $k_{\mathrm{pl}}$, and with this the properties of the plasmonic mode. We will use the same method to extract the plasmonic mode in more complex structures later in this chapter.

For a plasmon on a metal-dielectric interface the plasmonic wavevector can also be given by a simple analytical expression $k_{\mathrm{pl}} = \omega/c\sqrt{\epsilon_m \epsilon_d/(\epsilon_m + \epsilon_d)}$, with $\epsilon_m$ being the permittivity of the metal, as discussed in Chapter 2. We will use this to verify that the resulting plasmonic properties obtained with both this analytical expression and the numerical model presented above give similar results. The results in Fig. 6.2 and Fig. 6.3 stems from both, the numerical model (squares) and the analytical model (lines) is shown for comparison.

The real part of the plasmonic wavevector $\mathrm{Re}[k_{\mathrm{pl}}]$ gives the propagation constant for the plasmonic mode. We plot the propagation constant for various frequencies resulting in the dispersion relation shown in Fig. 6.2. The dispersion of the plasmonic mode is plotted for gold and silver for two different permittivities of the dielectric $\epsilon_d = 4.3$ (left plot) and $\epsilon_d = 12.7$ (right plot). For low frequencies we see that the plasmonic dispersion approaches the light-line, indicating that the polariton is light-like. On the other hand, for fre-

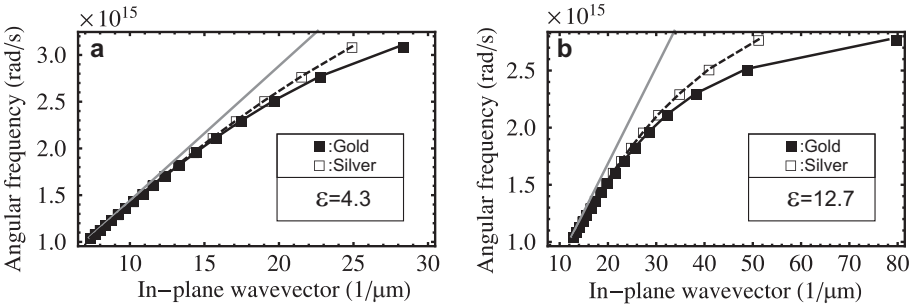


*Figure 6.2: Dispersion of surface plasmon polariton. The grey lines in the two plots indicate the light cone for the dielectrics, which are $\epsilon_d = 4.3$ (left plot) and $\epsilon_d = 12.7$ (right plot). The plasmonic mode is obtained for both gold (filled squares and solid line) and silver (open squares and dashed line), either by the numerical method (squares) or by the analytical expression (lines). Note that the wavevector scales are different.*

quencies near the plasmonic resonance the plasmonic wavevector increases, and the polariton becomes electron-plasma-like. We generally see that the group velocity, defined as the slope $v_g = \partial\omega_{\mathrm{pl}}/\partial k$ [44], for the plasmonic mode at a given frequency is lower for gold than silver. As the interaction of a plasmonic mode with an emitter scales inversely with the group velocity, this suggest that the interaction with gold structures are stronger. We note that this difference is very small around $\omega = 1.9 \times 10^{15}$ rad/s which corresponds to the emission frequency of the quantum dots described throughout this thesis.

While the real part of $k_{\mathrm{pl}}$ gives the propagation wavevector, the imaginary part determines the propagation length, which we now discuss for various material combinations. Here we calculate the propagation length as the distance traveled before the intensity of the field has fallen off with $1/e$ as discussed in Chapter 2. We also calculate the extension of the plasmonic mode into the dielectric, also given in Chapter 2, as this determines the distances between metal and emitter, where plasmon-matter interaction can take place.

The extension of the plasmonic modes, shown in Fig. 6.3a, spans more than a decade as the dielectric permittivity is changed from $\epsilon_d = 1 - 16$ but is very similar for gold and silver. The propagation distance also spans two decades for both gold and silver, cf. Fig. 6.3b, but we note that the modes on the silver

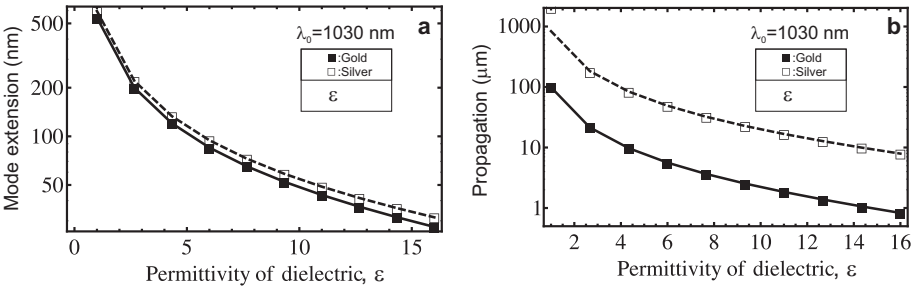


*Figure 6.3: Extension- (**a**) and propagation length (**b**) of surface plasmon polaritons at $\lambda_0 = 1030$ nm. The properties are obtained for both gold (filled squares and solid line) and silver (open squares and dashed line), either by the described numerical method (squares) or by the analytical expression (lines).*

interface propagate a factor $\sim 10$ longer than those on the gold interface. For a low-index material ($\epsilon_d = 2.7$), this yields propagation distances of 22 μm (gold) and 175 μm (silver), respectively. For GaAs ($\epsilon_d = 12.25$), the corresponding propagation length is 1.5 μm (gold) and 13.7 μm (silver), respectively.

In Fig. 6.2 and Fig. 6.3 we find a good agreement between the two approaches used to extract the plasmonic properties, thus validating the numerical model. We find that plasmons on silver and gold are very similar in regard to dispersion and confinement, but differ by approximately a decade in their propagation length. Furthermore, we find that the high-index dielectrics, e.g. GaAs, yield plasmonic modes with very different characteristics than plasmonic modes in low-index systems. The calculations presented in this section will serve as a reference to the next sections, where we will impose geometrical constraints on the plasmonic mode confining it to two dimensions, and later to one dimension.

## 6.2 Confinement to two dimensions

As an intermediate step towards one-dimensional plasmonic structures, we study the effect of confining the field to two dimensions. We study a slab of dielectric sandwiched between two semi-infinite metallic substrates. We will in the remainder of this chapter only use silver as the metal, and remember that the optical properties are very similar for gold, except for the resulting

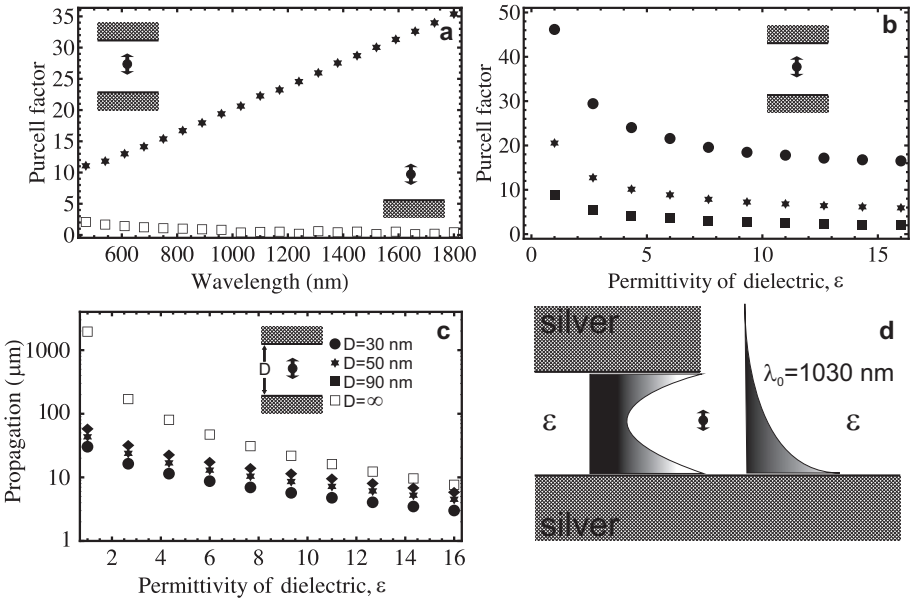


*Figure 6.4: Properties of plasmonic modes in metal-dielectric-metal slabs.* **a**, *Purcell factor for a dipole emitter oriented perpendicular to the interfaces at a distance of* 25 nm. *The dielectric has a permittivity of* $\epsilon_d = 1$ *and the Purcell factor is calculated for an interface (open squares) and a slab structure (stars).* **b**, *Purcell factor as a function of the permittivity of a dielectric slab between two silver half-spaces. The wavelength of the emitter is* $\lambda_0 = 1030$ nm *and it is placed in the middle of the dielectric slab. The Purcell factor is plotted for three different thicknesses, see inset of* **c**. **c**, *Propagation distance for three different thicknesses of the dielectric slab and for a simple interface. The inset explains the symbol convention.* **d**, *Sketch of the enhancement effect: When the metal half-spaces are brought closer to each other than the extend of the plasmonic modes at a simple interface, then geometrical enhancement of the plasmonic field is possible.*

propagation lengths. The plasmonic modes now also depend on the geometry of the structure (thickness of dielectric) and not only on the material parameters as for the metal-dielectric interface. We expect the plasmonic mode to be influenced by the confinement when the gap between the mirrors becomes smaller than the extension of the plasmonic mode at the bare interface, see.

Fig. 6.3 and Fig. 6.4d. We calculate the plasmonic mode in the same manner as above using the Green's function for a metal-dielectric-metal slab, as given in Appendix A.

Firstly, we note that the propagation distance, c.f. Fig. 6.4c, reveals that, as the plasmons become confined due to the second mirror, a larger part of the mode is forced into the metal whereby bigger losses are induced. Thus resulting in shorter propagation lengths with stronger confinement.

Furthermore, as for the simple interface, the propagation distance becomes shorter as the permittivity of the dielectric rises. In Fig. 6.4 we also see that, as the dielectric index increases, the difference between modes at the interface and in the slab decreases. This is a consequence of the shortening of the mode extension, whereby the effect of the confinement becomes less severe.

We calculate the interaction of the plasmonic modes with a simple dipole emitter, which we place in the center of the dielectric slab. The plasmonic modes are polarized such that a dipole oriented perpendicular to the metallic surfaces couples most effectively to the plasmonic modes. There is a pronounced difference in the Purcell factor between an emitter placed 25 nm above a simple interface and in the middle of a 50 nm slab structure, c.f. Fig. 6.4a. An emitter in air near a simple interface couples most efficiently close to the bulk plasmon resonance, which for silver is at $\lambda_0 \approx 400$ nm. For an emitter in a metal-dielectric-metal slab the Purcell factor, given as the ratio of decay into the plasmonic mode, $\gamma_{\mathrm{pl}}$, over the decay in homogeneous dielectric, $\gamma_d$, scales as in Ref. [69]:

$$F_{\mathrm{pl}}^{P} = \frac{\gamma_{\mathrm{pl}}}{\gamma_d} = \frac{3}{4}\frac{c/n}{v_g}\frac{c/n}{v_p}\frac{\lambda_0/n}{L_{\mathrm{eff}}}, \tag{6.2}$$

where $n = \sqrt{\epsilon_d}$ is the refractive index of the dielectric, $v_g$ ($v_p$) is the group (phase) velocity, and $L_{\mathrm{eff}}$ is the effective mode-length as described in Ref. [69]. Figure 6.4a shows that the Purcell factor increases linearly with wavelength, in agreement with Eq. (6.2), reaching $F_P = 35$ at $\lambda_0 = 1800$ nm for an emitter placed in the middle of a dielectric slab ($\epsilon_d = 1$) with a thickness of 50 nm surrounded by silver. The scaling of the Purcell factor as function of the dielectric permittivity for three different thicknesses of the dielectric slab in shown in Fig. 6.4b for a fixed wavelength. We find that as the permittivity of the dielectric increases the Purcell enhancement is diminished. The non-resonant enhancement of the Purcell factor scales roughly as $\gamma_{\mathrm{pl}}/\gamma_d \propto n^{-1}$, as given by Eq. (6.2).

We find that confining the plasmonic mode to two dimensions enables strong non-resonant coupling to the plasmonic modes, where the rate of coupling scales as $\gamma_{\mathrm{pl}}/\gamma_d \propto \lambda_0 n_d^{-1}$. The physical reason for this scaling behavior stems from the fact that the sub-wavelength geometry of the structure, rather than the wavelength of the light in the media, defines the extension of the mode. Futhermore, the confinement results in plasmonic modes that are less light-like and thus have shorter propagation distances than the modes at a simple interface. Finally, we find that raising the permittivity of the dielectric yields shorter propagation distances of the plasmonic modes, as well as weaker coupling to quantum emitters.

## 6.3 Modes of plasmonic gap waveguides

After having investigated interface- and slab structures in the previous sections, we now turn to gap waveguides. The structures discussed in this section are analyzed using a finite-element method [80]. The model assumes translational invariant structures, and computes the guided modes along the invariant direction. The model returns the electromagnetic field associated with the modes as well as the wavevectors of these. Here, we model the properties of plasmonic gap waveguides, which were also discussed in Chapter 5. We will study the effect of the geometry of the structures keeping the permittivity of the surrounding media fixed at $\epsilon = 12$ for guided modes corresponding to a free-space wavelength $\lambda_0 = 1030$ nm.

We calculate the Purcell enhancement of the decay rate for a quantum dot placed in the center of the gap with the dipole moment oriented in the $x$-direction for optimal coupling to the fundamental gap waveguide mode. See inset of Fig. 6.5b for coordinate axis convention. For the dipole moment oriented in the $y$-direction the coupling to the mode is approximately two orders of magnitude weaker, thus we will restrict this study to a dipole oriented along $x$. Throughout this section we keep the width of the the two metal stripes constant (200 nm comparable to fabricated widths) and note that the properties of the mode guided in the gap is also influenced by this width. The number of guided modes is determined by this width, but the two fundamental modes (gap-mode and side-mode introduced in Chapter 5) are always present. In this section we only study the coupling to the fundamental gap mode.

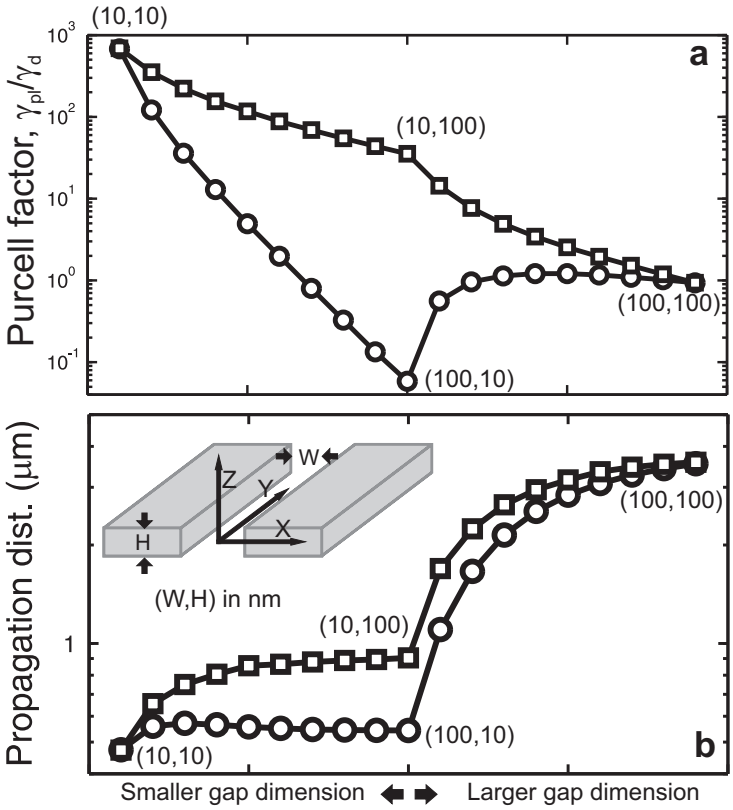


*Figure 6.5: The Purcell enhancement for the decay into- and propagation distance of the fundamental gap-mode for various plasmonic gap waveguides. We study modes corresponding to a free-space wavelength of $\lambda_0 = 1030$ nm. The metal is silver and the surrounding dielectric has $\epsilon = 12$. The width and height of the gap is varied linearly from $10-100$ nm where the numbers in parentheses denote these in nanometer, $(W, H)$.* **a**, *The Purcell factor is calculated for a dipole emitter placed in the middle of the gap with dipole moment along $x$, see inset in* **b**. **b**, *Propagation distance for the fundamental gap-mode for varying waveguide geometries (same convention as in* **a**).

The plasmonic modes in the slab structure, studied in the previous section, were shown to strongly alter the decay dynamics of a nearby emitter. Now, we confine the plasmonic mode further, restricting it to propagate in one dimension. This results in additional modifications of the properties of the modes as well as to the decay of a nearby emitter. In Fig. 6.5a the Purcell factor is shown for an emitter in the center of the gap waveguide mode when the waveguide gap dimensions are varied from $10 \times 10$ nm$^2$ to $100 \times 100$ nm$^2$. We change the geometry of the gap along two different routes: by first letting the width grow and then the height, or oppositely, first the height and then the width. We see that the dependence of the Purcell factor on the width of the gap is much stronger than on the height of the gap: the Purcell factor decreases four orders of magnitude with increasing width in comparison to a bit more than one order of magnitude for increasing height. We also see that the effect of increasing the height of the gap depends on how wide the gap is: the Purcell factor rises for a 100 nm wide gap when the height is increased from 10 nm and all the way to 50 nm whereafter is starts to fall off again. In contrast to a 10 nm wide gap were the Purcell factor monotonically falls with increasing height.

In Fig. 6.5b the propagation distance for the plasmonic mode guided in the gap is shown for the same series of plasmonic gap waveguides. For a gap width of 10 nm the resulting propagation distance is below 1 μm and only weakly dependent on the height. The same is true for a height of 10 nm where the propagation distance is only weakly dependent on the width. Generally for these two plots we note that in the limit of $H \to \infty$ we recover the results from the slab section. As expected [17], we find that generally the propagation length is longer for less confined modes, though there is a strong influence from the specific geometry of the gap.

Plasmonic gap waveguides fabricated by lithography and metal evaporation, have a build in asymmetry of the surrounding dielectric. This asymmetry can be removed if the structure is coated with a dielectric matching the substrate material. When the substrate is GaAs no simple index matching coating material exists, which makes a study of asymmetric surroundings relevant. Such structures with asymmetric dielectric surroundings are the subject of Fig. 6.6, where the bottom material is kept fixed at $\epsilon = 12$, and the index of the top material is varied. The Purcell factor is given as the decay rate into the plasmonic mode normalized to the decay rate in a homogeneous dielectric. We

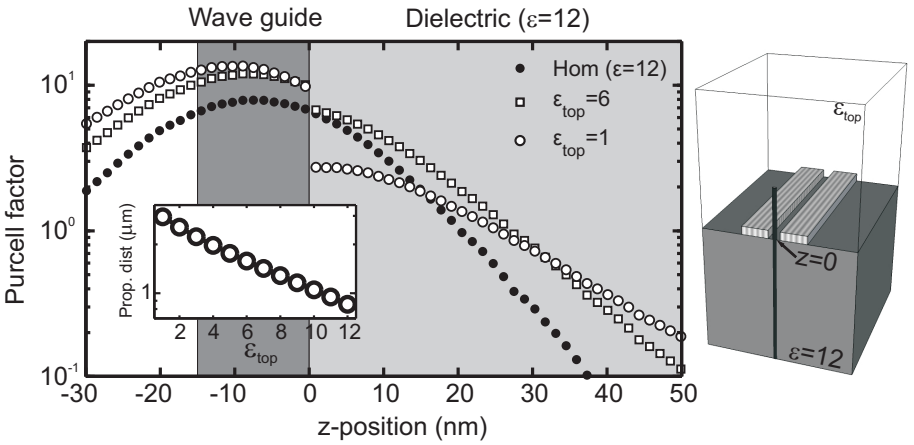


*Figure 6.6: Influence of position and dielectric coating index on the Purcell factor. A plasmonic gap-waveguide with a gap width of $W = 50$ nm and a metal height of $H = 15$ nm, is placed atop a high-index dielectric with $\epsilon = 12$. The Purcell factor is calculated for an emitter placed along the $z$-axis passing through the center of the gap, for three different coating dielectrics. The dark gray shading shows the position of the waveguide, and the light gray denotes the high-index dielectric. The inset shows the propagation distance for various coating dielectrics.*

study the effect for an emitter placed along a vertical line passing through the center of the waveguide and into the substrate, see illustration in Fig. 6.6. The dielectric medium is different on top and bottom of the structure giving rise to two different decay rate normalizations, thus causing the discontinuity in the Purcell factors across the interface between the two media. The achievable Purcell enhancement outside the substrate dielectric scales with the top index, with stronger enhancement for lower permittivities.

Inside the substrate the behavior is more complex as there are two competing effects:

1. The rate of decay into plasmons $\gamma_{\mathrm{pl}}$ is proportional to the square of the in-plane electric field which is continuous across the dielectric interface, thus, the discontinuity at the interface is solely determined by the normalization difference set by the decay rates in the homogeneous media. The result is that the Purcell factor is reduced with a factor $\sqrt{\epsilon_{\mathrm{bottom}}/\epsilon_{\mathrm{top}}}$

when the emitter enters the substrate.

2. The extend of the mode scales inversely with the top-index $\epsilon_{\text{top}}$, thus extending further into the bottom material for a lower top-index.

The result of these two effects is that there, for a given emitter position in the substrate, is an optimal top-index for the Purcell enhancement, as seen in Fig. 6.6. The resulting propagation distances are longer for lower top-indexes, as shown in the inset in Fig. 6.6. We therefore conclude that the asymmetry is beneficial for coupling emitters situated within the bottom substrate, which is the case for quantum dots to the plasmonic gap mode.

The coupling to plasmonic gap waveguides can be enhanced substantially from the values achievable in a metal-dielectric-metal slab, due to the extra confinement defined by the finite height of the gap waveguide. The fundamental mode supported by the gap is polarized such that the in-plane dipole-moment of quantum dots couple efficiently to this, thus providing a feasible way to couple quantum dots and one-dimensional plasmonic waveguides. The asymmetry introduced around plasmonic gap waveguides by the fabrication procedure can be employed as a resource, i.e., by engineering the top-dielectric index for optimal coupling and propagation length for the guided plasmonic mode. All of these scaling behaviors can be employed to optimize the coupling.

We also find that if we restrict ourselves to the experimental condition of Chapter 5, i.e., emitters in high-index materials ($\epsilon_{\text{GaAs}} \approx 12$) placed $\sim$ 25 nm into the material, then the resulting Purcell factors are of the order of unity for readily fabricatable plasmonic gap-waveguide geometries (gap size = 50 nm). Furthermore, the propagation lengths are of the order of 3 μm for silver structures which imposes severe challenges for outcoupling mechanisms. Note, that we in Chapter 5 used gold, for which the propagation length is even shorter.

## 6.4 Outlook on plasmon-based single-photon sources

In this section we will discuss the possibilities for plasmon-based single-photon sources in the light of our findings above. We found that if we impose the restriction that the quantum dot is placed within the substrate $z \sim 25$ nm, then

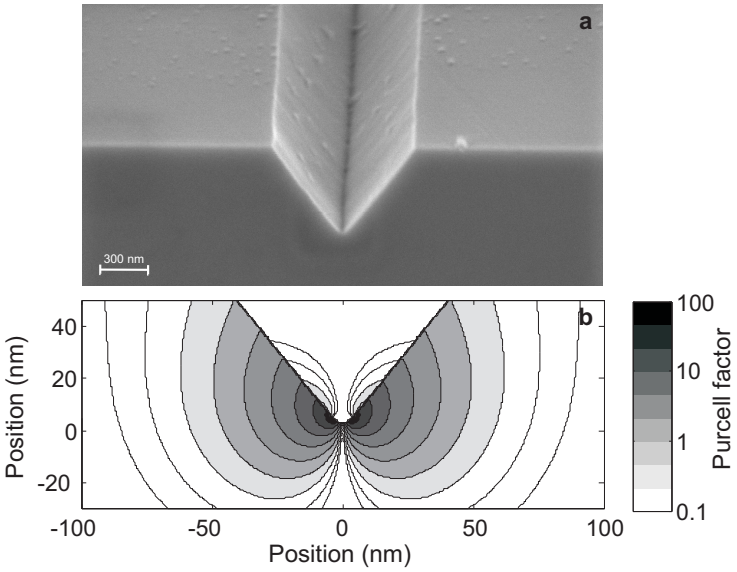


*Figure 6.7: Coupling to a plasmonic wedge waveguide.* **a**, *SEM picture of an etched groove into the GaAs substrate before metal evaporation.* **b**, *Purcell enhancement calculations for a dipole emitter coupled to the plasmonic wedge waveguide. The dipole is oriented horizontally and the metallic wedge which is surrounded by GaAs.*

the achievable Purcell factors are very limited, as the metallic structures are evaporated on top of the substrate. Here, we will briefly discuss the possibility of bringing the metallic structures into the substrate to allow for a stronger coupling to the quantum dots. A sharp metallic wedge supports guided plasmonic modes [105] at the tip of the wedge. By defining a groove into the GaAs substrate and subsequently filling this by evaporating metal such a wedge tip can be brought very close to the quantum dots. This approach has the benefit that the distance between the dots and the substrate surface is still large. A sharp groove into the GaAs substrate can be realized by utilizing selective etching along certain crystal planes. In resemblance to plasmonic structures defined via template stripping [91], metal evaporated onto such grooves inherits the smoothness at the interface between substrate and metal. This fabrication method results in smooth grooves etched into GaAs, as shown in Fig. 6.7a.

Finite-element calculations has been carried out for groove structures with

dimensions identical to a test sample. The groove supports a number of modes, one of which is confined to the tip of the groove. The resulting Purcell enhancement for an in-plane dipole moment coupled to this mode is shown in Fig. 6.7b. Purcell factors on the order of ten is achievable in this geometry. Thus offering coupling an order of magnitude better than what is possible with plasmonic gap-waveguides, given the constraint that the interface is more than 25 nm away from the dots. The mode is supported by the edge of the groove and is, thus, very sensitive to the radius of curvature of the edge. Here, a 5 nm radius of curvature is used. The radius of curvature also strongly affects the propagation length, which for this choice is $\sim 270$ nm using the optical constant from Ref. [106]. Thus the groove structure offers a possibility to achieve efficient coupling to InAs quantum dots in GaAs, but the propagation distance of the guided mode is very short.

In the previous sections we discussed plasmonic modes in terms of their ability to efficiently capture and guide single excitations of quantum emitters. Plasmonic modes do not propagate far, thus, the out-coupling to free photons is a topic that must be adressed in any discussion of realistic plasmon-based single-photon sources. The plasmonic modes have wavevectors that are larger than the wavevectors for a photonic mode with the same energy in a homogenous dielectric. This imposes an intrinsic problem for plasmon-based single-photon sources, namely the conversion from a plasmonic mode to a photon. Both phase-matching and spatial mode-matching need to be considered, depending on the out-coupling scheme. Here, we will briefly discuss the coupling to free photons either by tapering the plasmonic mode until there is a substantial overlap with a free-space photon, by evanescent coupling to a dielectric waveguide, or by grating coupling, where a periodic structure can absorb the additional momentum carried by the plasmonic mode.

Plasmonic waveguides can be tapered to a different geometry where the field mode is less confined and propagates further [107]. This has the additional advantage that it moves the plasmonic mode dispersion closer to the light-cone, making the phase-matching to free-space photons easier to accomplish. Furthermore, due to the polarization of the fundamental gap waveguided mode, it would couple to a normal polarized Gaussian light beam.

An efficient tapering should rely on an adiabatic change of the mode (by changing the supporting structure), from the tightly confined and strongly in-

teracting mode to a mode that is only weakly confined that can couple easily to photons, see Fig. 6.8a. Changing the mode too fast leads to reflections of the propagating mode, and changing it too slow leads to decay of the mode due to damping. Given the sub-micrometer propagation distances in the structures discussed in this chapter, the adiabatic change must be implemented over very short distances. We note that the tapering of the in-plane dimensions of plasmonic waveguides is straightforward to implement in the current fabrication process. However, a simple scaling of the width of the gap as shown in Fig. 6.8a does not increase the propagation distance significantly as shown in Fig. 6.5b. Thus, detailed calculations of tapering geometries are needed in order to characterize any specific structure.

The dispersion of dielectric fibers can be tailored to support a large range of wavevectors. By phase-matching the fiber dispersion to that of the plasmonic waveguide mode, evanescent transfer of the plasmon mode to the fiber can be realized if the two are brought sufficiently close to each other, as shown in Fig. 6.8b. The mode population oscillates between the fiber and the nanowire in the interaction region, whereby efficient transfer of the mode to the fiber can be achieved by tailoring the length of the interaction region [19]. In order to achieve phase-matching, special dielectric fibers are needed. For plasmonic modes in low-index dielectrics, high-index fibers can be used to phase-match and outcouple. On the other hand, we find that in order to match the wavevector of the plasmonic modes in high-index dielectrics, specialized fibers, e.g. photonic crystal fibers/waveguides, may be needed to obtain large enough wavevectors.

An alternative outcoupling method is to terminate the waveguide in a grating structure, which can provide or absorb specific quantas of momentum from the plasmonic mode. Thus, a grating can be engineered to scatter the guided plasmon into a freely propagating photon, as shown in Fig. 6.8c. The scattering angle is determined by the grating periodicity and the size of the interacting grating area. Introducing a grating in a nanowire provides an efficient way to convert the plasmonic mode to a photon. However, due to the small transverse extent of the nanowire - and thereby the grating structure, the emission direction (beyond the scattering angle) is not well controlled. Such an approach is therefore not feasible for an efficient plasmon-based single photon source.

As an alternative to having the plasmonic mode propagating in a fixed

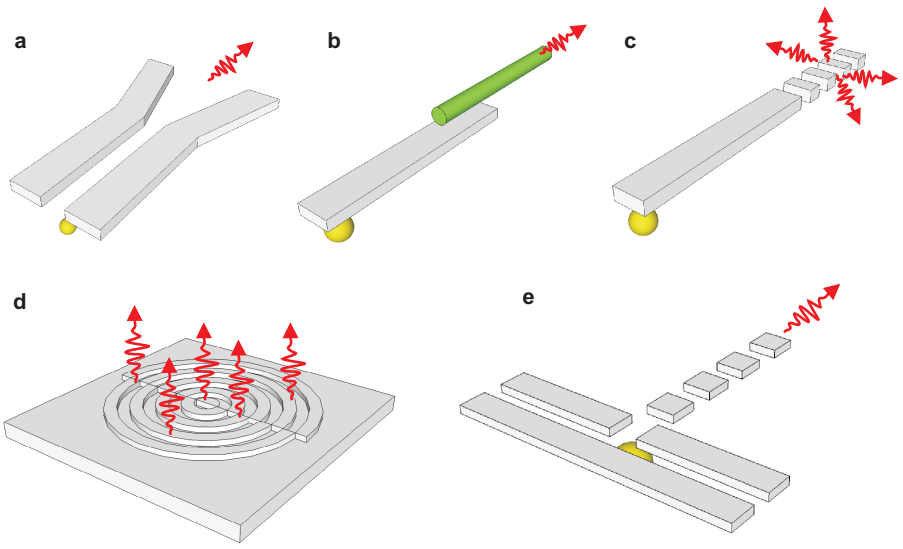


*Figure 6.8: Plasmon-based single-photon sources. Grey materials indicate metal and the yellow spheres quantum dots.* **a**, *By tapering the shape of the gap, the supported plasmonic mode can be brought close to phase matching with the wavevector of a free photon at the wide end of the waveguide.* **b**, *Evanescent coupling of the plasmon to a phase-matched dielectric fiber over a controlled length.* **c**, *Terminating the plasmonic waveguide with a grating can efficiently couple the plasmon to a photon traveling perpendicular to the waveguide, but control over the specific direction is not possible due to the sub-wavelength dimensions of the waveguide.* **d**, *Plasmonic modes on a metal film propagate many micrometers, which enables a large grating to be employed to yield a collimated beam of single photons.* **e**, *Plasmonic nanoantennas can be used to couple an excited quantum dot directly to a free-space photon propagating in a predefined direction, thus bypassing propagation in the lossy metals.*

direction and subsequently outcoupling to photons, we will briefly discuss two alternative routes towards plasmon-based single-photon sources.

In Chapter 4, we studied the coupling of quantum dots to surface plasmons at a metallic interface. These modes are much less confined and propagate tens of micrometer before they are lost due to damping. By introducing a ring grating with broken symmetry the plasmonic mode can be coupled to a freely propagating photon, as shown in Fig. 6.8d. The ring grating is chosen as it matches the circular symmetric plasmonic mode excited by a quantum dot, and the asymmetry is induced to make spatial mode matching to a polarized free-space photon. Due to the long propagation distances at a simple interface the direction of the resulting scattering from the grating can be well controlled [108]. This approach does not rely on a very efficient coupling to the plasmonic mode, but provide a way to efficiently transfer the excitation to a directional free-space photon.

Lastly, metallic nano-particles support non-propagating localized plasmonic modes which can be used to form nano-antennas that can shape the emission profile of a nearby emitter [109, 110, 111, 112], as shown in Fig. 6.8e. This approach bypasses the propagation losses by directly coupling the emitter to a freely propagating photon. Thus, nano-antenna single-photon sources could provide a way to achieve fast, efficient single-photon emission from quantum dots - but detailed calculation for realistic implementations need to be performed before such predictions are accepted.

## 6.5 Conclusion

We have studied the properties of plasmonic modes for gold and silver and, importantly, for various dielectric materials. In order to utilize the excellent single-photon properties of InAs quantum dots, the plasmonic waveguides must be placed near these, and will therefore have some hybrid dielectric surrounding made up of GaAs and other dielectrics. Generally, the extent and propagation length of the plasmonic modes reduce with increasing permittivity of the surrounding dielectric. This was found to imply, for a metal-dielectric-metal slab, that the Purcell-enhancing effect of the confinement reduces for higher dielectric permittivities. This conclusion also applies to plasmonic gap waveguides, which we have studied for various gap-geometries. We found that neither prop-

agation length nor achievable Purcell factor scaled simply with the area of the gap, but showed complicated dependence on the specific structure. We also studied the experimentally important effect of an inhomogenous dielectric surrounding, and found that for an emitter positioned in the high-index medium, it is possible to choose a top dielectric to maximize the Purcell effect, and that the optimal top-index does not correspond to homogeneous surroundings.

For InAs quantum dots ($\lambda_0 = 1030$ nm, $y \approx 25$ nm) in GaAs ($n = 3.42$) with air as top material coupled to a gap waveguide with a 50 nm gap, we found that the propagation length is $\sim 3$ μm for silver, and the Purcell enhancement is on the order of unity . This implied that the structures fabricated in Chapter 5 are not good candidates for efficient plasmon-based single-photon sources. Lastly, we have discussed out-coupling mechanisms and two alternative plasmonic systems (ring gratings, nano-antennas) that might be better solutions for plasmon-based single-photon sources.

# Chapter 7

# Conclusion

This thesis reported results on enhanced light-matter interaction between self-assembled quantum dots and semiconductor-metallic nano-structures. The quantum theory of spontaneous emission was derived, the nano-structure fabrication was discussed, and measurements and data analysis of spectrally- and time-resolved photoluminescence from single- and ensembles of quantum dots were presented.

The fabrication of simple semiconductor/air and semiconductor/metal interfaces, used as spectroscopic tools to investigate the fundamental light-matter interaction, was presented. The optical fields can in these structures be calculated directly, and are only dependent on the interface-emitter distance which can be well-controlled. Time-resolved measurements on quantum dots in these, simplest imaginable nano-structures, revealed an underlying physics that is surprisingly rich. By studying a set of three such structures (reference, direct, and inverted) we were able to experimentally demonstrate that the dipole-approximation is not fulfilled for quantum dots in general. We found from time-resolved measurements on ensembles of quantum dots that the decay rate differs markedly from the dipole-expectancy even in these simple structures. This led us to conclude that great care should be exercised when interpreting decay dynamics in more advanced structures, and also to suggest that this novel mechanism is utilized as a resource to control light-matter interaction in nano-structures in general.

A theoretical model for the spontaneous decay of extended emitters in nano-

structured media was presented. The spatial variation of the light-field modes over the extension of the emitters was included as the fields are approximated by their Taylor expansion, where the gradient contributions to first order were retained. This naturally led to an additional intrinsic transition moment of extended emitters, namely the mesoscopic moment. Simple symmetry considerations on the quantum dot wavefunctions let us impose geometrical constraints on the mesoscopic moment for quantum dots, and particularly revealed that the decay mechanism associated with these moments contributes on the quantum dot ground state transition. The contributions from the dipole- and mesoscopic moments interfere to modify the decay rate. The interference can be changed from destructive to constructive and *viceversa* by turning the quantum dot upside-down.

We compared the theoretical model to our measurements of decay dynamics that deviate from dipole theory and found very good agreement. We extracted the mesoscopic moment from the comparison and used this to predict strongly modified decay dynamics of mesoscopic quantum dots when placed in the vicinity of a silver nanowire.

Our conclusions on the decay dynamics of mesoscopic quantum dots are also expected to be of relevance for purely dielectric nano-strucures. Mesoscopic quantum dot effects are, thus, anticipated to be of importance for spontaneous-emission control in, e.g., photonic crystals, photonic crystal waveguide single-photon sources, and cavity quantum-electro-dynamics. Particularly, when employing very large quantum dot emitters due to their prospective large oscillator strength.

Our findings are surprising since the point-dipole approximation has been uncritically adopted in the literature to describe light-matter interaction between quantum dots and nanophotonic structures. Importantly, the measured mesoscopic effects are very pronounced, and may be employed as a resource to enhance light-matter interaction, which is required in a diverse range of scientific fields ranging from quantum information science, and quantum computing to energy harvesting devices.

A fabrication method to produce plasmonic gap waveguides was developed, and the gap waveguides were shown to support guided modes that are suitable for coupling to quantum dots in a planar technology. The coupling efficiency scales with the dimensions of the structure, and it is thus desirable to fabricate

very small structures. We successfully fabricated plasmonic gap waveguides with a gap width down to 50 nm and demonstrated that we can control a number of geometry parameters, which is required to scale the fabrication process to more advanced networks.

Time-resolved measurements of single quantum dots placed 25 nm below a plasmonic gap-waveguide were performed. We found quantum dots that decayed both faster or slower than reference quantum dots placed away from the waveguides. From a comparison with the position dependent theory we conclude two things: Firstly, that a wide range of decay rates are consistent with theory. This makes quantitative analysis of decay dynamics very difficult and possible only through a statistical approach. Secondly, that in order to distinguish the coupling to lossy modes from coupling to guided modes the propagation of guided plasmons should be observed. This was not possible in the measured structure as the propagation length is on the order of the excitation/detection area.

By theoretically studying the coupling mechanism of a dipole emitter to various plasmonic structures with various material combinations, we were able to conclude that the extent and propagation length of the plasmonic modes decrease rapidly with the refractive index of the surrounding material. This poses challenges both on the part of fabrication, i.e., to place the quantum dots close enough to the structure to achieve an efficient coupling, and on experiments, i.e., to distinguish the coupling to a guided mode from that to a lossy mode. In addition, we found that neither propagation length nor achievable Purcell factor scaled simply with the area of the gap, but showed a complicated dependence on the specific structure. Furthermore, for the experimentally relevant case of inhomogenous dielectric surroundings, the top-material can be chosen to maximize the coupling to an underlying quantum dot. The optimal material choice is determined by the waveguide-emitter distance. Finally, we concludes that for realistic waveguide parameters, achievable Purcell enhancements are of the order of unity, and the resultant propagation distances are on the order of few micrometer. Thus, plasmon-based single-photon sources in high-index material systems ($n_{\mathrm{GaAs}} \approx 3.5$) should incorporate either a very fast out-coupling mechanism or - preferably - not rely on the propagation in strongly confined modes at all.

# Appendices

# Appendix A

# Dyadic Green's function for a slab structure

A closed expression for the Green's function of a multi-layer slab structure is given in Ref. [113], but we have adapted the notation of Ref. [114] where only three layers are considered. The dyadic Green's function is defined as an integral over the in-plane wavevectors,

$$\mathbf{G}(\mathbf{r},\mathbf{r}';\omega) = \int \frac{d^2\mathbf{k}}{(2\pi)^2} e^{i\mathbf{k}(\boldsymbol{\rho}-\boldsymbol{\rho}')} \mathbf{G}(\mathbf{k},z,z';\omega). \tag{A.1}$$

Here $\mathbf{k} = (k_x, k_y)$ is the in-plane wavevector set and $\boldsymbol{\rho} = (x, y)$ is the in-plane position. The geometry of the studied system is shown in Fig. A.1: An emitter is placed in the middle material which has the relative permittivity $\epsilon_1$. The middle material borders materials with permittivity $\epsilon_2$ above and $\epsilon_3$ below. The height of the sandwiched material is $L$ and the emitter is situated $z_0$ from the bottom material.

In Eq. (A.1) the following expression appears:

$$\mathbf{G}(\mathbf{k},z,z';\omega) = \frac{2\pi i}{\beta_1}\frac{k_1^2}{\epsilon_1} e^{i\beta_1 L} \sum_{q=p,s} \xi_q \frac{E_{q1}^{>}(\mathbf{k},\omega,z) E_{q1}^{<}(-\mathbf{k},\omega,z')}{1 - r_{12}^q r_{13}^q e^{2i\beta_1 L}}, \tag{A.2}$$

where $\beta_j = \sqrt{k_j^2 - k^2} = \sqrt{\epsilon_j k_0^2 - k^2}$ is the out-of-plane wavevector, with $k_0 = \omega/c$. Furthermore, $r_{12}^q$ and $r_{13}^q$ are the conventional Fresnel reflection

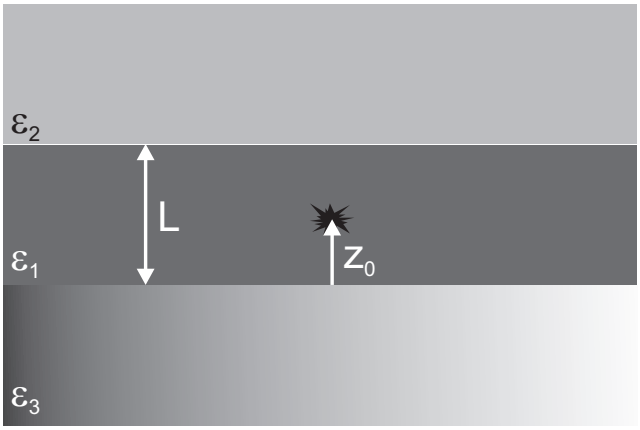


*Figure A.1: Sketch of the studied slab-system. Two semi-infinite media with permittivity $\epsilon_2$ and $\epsilon_3$ are at the top and bottom, respectively, of a third sandwiched medium with permittivity $\epsilon_1$. The middle medium has the height $L$. The emitter is situated $z_0$ from the bottom medium.*

coefficients for $s$- and $p$-polarized modes from medium 1 to 2 and 1 to 3,

$$r_{ij}^{p} = \frac{\epsilon_j\beta_i - \epsilon_i\beta_j}{\epsilon_j\beta_i + \epsilon_i\beta_j}, \tag{A.3}$$

$$r_{ij}^{s} = \frac{\beta_i - \beta_j}{\beta_i + \beta_j}. \tag{A.4}$$

Lastly,

$$E_{q1}^{>}(\mathbf{k},\omega,z) = \hat{\mathbf{e}}_{q1}^{+}(\mathbf{k})e^{i\beta_1(z-L)} + r_{12}^{q}\hat{\mathbf{e}}_{q1}^{-}(\mathbf{k})e^{-i\beta_1(z-L)}, \tag{A.5}$$

$$E_{q1}^{<}(\mathbf{k},\omega,z') = \hat{\mathbf{e}}_{q1}^{-}(\mathbf{k})e^{-i\beta_1 z'} + r_{13}^{q}\hat{\mathbf{e}}_{q1}^{+}(\mathbf{k})e^{i\beta_1 z'}, \tag{A.6}$$

$$E_{q1}^{<}(-\mathbf{k},\omega,z') = \hat{\mathbf{e}}_{q1}^{-}(-\mathbf{k})e^{-i\beta_1 z'} + r_{13}^{q}\hat{\mathbf{e}}_{q1}^{+}(-\mathbf{k})e^{i\beta_1 z'}, \tag{A.7}$$

where $\hat{\mathbf{e}}_{p1}^{\pm}(\mathbf{k}) = \frac{1}{k_1}(\mp\beta_1\hat{\mathbf{k}} + k\hat{\mathbf{z}}) = \hat{\mathbf{e}}_{p1}^{\mp}(-\mathbf{k})$ and $\hat{\mathbf{e}}_{s1}^{\pm}(\mathbf{k}) = \hat{\mathbf{k}}\times\hat{\mathbf{z}} = -\hat{\mathbf{e}}_{s1}^{\mp}(-\mathbf{k})$ and finally $\xi_p = 1$ and $\xi_s = -1$.

We have in our formalism used a dyadic Green's function decomposed into its nine cartesian tensor components. In order to bring the expression presented here to this form, we use that

$$\hat{\mathbf{k}} = (\cos\theta\hat{\mathbf{x}} + \sin\theta\hat{\mathbf{y}}), \tag{A.8}$$

$$\hat{\mathbf{k}}\times\hat{\mathbf{z}} = (\sin\theta\hat{\mathbf{x}} - \cos\theta\hat{\mathbf{y}}). \tag{A.9}$$

The resulting expressions for the products, i.e., $E^{>}_{q1}(\mathbf{k},\omega,z)E^{<}_{q1}(\mathbf{k},\omega,z')$, are straightforward to obtain, but become very lengthy. We will therefore not write them here.

We note that due to the simple dependence of the integrand of the dyadic Green's function on the coordinates $(x,x',y,y',z,z')$ it is straightforward to construct the spatial derivatives $(\nabla_j,\ \nabla'_j,\ \nabla_j\nabla'_k)$ of the integrand of the dyadic Green's function. After these are constructed we evaluate the expression in $x=x'=y=y'=0$ and $z=z'=z_0$, and change the integral over the in-plane wavevectors to cylindrical coordinates

$$\int d^2\mathbf{k} \rightarrow \int_0^\infty dk k \int_0^{2\pi} d\theta, \tag{A.10}$$

where the integral over $\theta$ is carried out analytically. All that remains is then to define the $z_0$, $L$, and the material parameters whereafter the integration over the in-plane wavevector $k$ is carried out numerically. We note that it is straightforward to subdivide the dyadic Green's function into contributions from different physical modes that can be distinguished by the length of their in-plane wavevector.

# Appendix B

# Maxwell's equations and dyadic Green's functions revisited

Maxwell's equations, i.e., Eq. (2.7), can be reformulated in terms of the vector- ($\mathbf{A}$) and scalar ($\phi$) potentials, from which the electric and magnetic field can be derived:

$$\mathbf{B} = \nabla \times \mathbf{A}, \tag{B.1}$$

$$\mathbf{E} = -\nabla\phi - \frac{\partial \mathbf{A}}{\partial t}. \tag{B.2}$$

The physical electric and magnetic field are unaffected by a gauge transformation of the potentials $\mathbf{A} \to \mathbf{A} + \nabla\lambda$ and $\phi \to \phi - \partial\lambda/\partial t$, which give us freedom to choose a gauge that is well-suited for our needs. The reformulated Maxwell's equations take the form

$$\nabla \cdot \left[\epsilon_r(\mathbf{r}) \left(\nabla\phi + \frac{\partial \mathbf{A}}{\partial t}\right)\right] = 0, \tag{B.3a}$$

$$\nabla \cdot \nabla \times \mathbf{A} = 0, \tag{B.3b}$$

$$\frac{\partial}{\partial t}\left[\nabla \times \mathbf{A}\right] - \nabla \times \left[\nabla\phi + \frac{\partial \mathbf{A}}{\partial t}\right] = 0, \tag{B.3c}$$

$$\nabla \times \nabla \times \mathbf{A} + \frac{1}{c^2}\frac{\partial}{\partial t}\left[\epsilon_r(\mathbf{r}) \left(\nabla\phi + \frac{\partial \mathbf{A}}{\partial t}\right)\right] = 0, \tag{B.3d}$$

where Eq. (B.3b) is trivially fulfilled. We utilize our freedom of gauge to set $\phi = 0$, which fulfils Eq. (B.3c) and results in the following constraints on $\mathbf{A}$

$$\nabla \cdot \left[ \epsilon_r(\mathbf{r}) \frac{\partial \mathbf{A}}{\partial t} \right] = 0, \tag{B.4}$$

$$\nabla \times \nabla \times \mathbf{A} + \epsilon_r(\mathbf{r}) \frac{1}{c^2} \frac{\partial^2 \mathbf{A}}{\partial t^2} = 0. \tag{B.5}$$

The first equation (Eq. (B.4)) is fulfilled when we choose $\nabla \cdot [\epsilon(\mathbf{r})\mathbf{A}] = 0$, which along with $\phi = 0$ is the generalized Coulomb gauge [49], which we will use in the following. The equation of motion for the vector potential is given by Eq. (B.5), which is an equivalent equation to the one derived for the electric field in Chapter 2. A vector potential that has harmonic time-dependence, fulfills the generalized Coulomb gauge, and fulfills the waveequation Eq. (B.5) can thus, as in Chapter 2, be decomposed into a sum of eigenfunctions $\mathbf{f}_l(\mathbf{r})$, that obey

$$\nabla \times \nabla \times \mathbf{f}_l(\mathbf{r}) - \epsilon_r(\mathbf{r}) \frac{\omega_\mu^2}{c^2} \mathbf{f}_l(\mathbf{r}) = 0, \tag{B.6}$$

$$\nabla \cdot [\epsilon(\mathbf{r}) \mathbf{f}_l(\mathbf{r})] = 0, \tag{B.7}$$

$$\int d^3\mathbf{r} \epsilon_r(\mathbf{r}) \mathbf{f}_l(\mathbf{r}) \cdot \mathbf{f}_m^*(\mathbf{r}) = \delta_{l,m}, \tag{B.8}$$

where $\omega_l$ is the eigenvalue associated with the mode from Eq. (B.6). Note that the orthonormality condition Eq. (B.8) is dependent on the environment $\epsilon_r(\mathbf{r})$, and reduces to the well-known condition for homogeneous media. The defining equation for the dyadic Green's function (Eq. (2.17) in Chapter 2) is equivalent to the equation for the field modes Eq. (B.6), except for the non-zero right hand side of Eq. (2.17). Therefore, a general solution to the dyadic Green's function can be expressed as an expansion on the field modes given above as

$$\mathbf{G}(\mathbf{r}, \mathbf{r}'; \omega) = \sum_l \mathbf{M}_l(\mathbf{r}'; \omega) \mathbf{f}_l(\mathbf{r}; \omega_l). \tag{B.9}$$

Inserting this into the definition of the dyadic Green's function and using Eq. (B.6) and Eq. (B.8) we find that the expansion coefficients are given by

$$\mathbf{M}_l(\mathbf{r}'; \omega) = c^2 \frac{\mathbf{f}_l^*(\mathbf{r}'; \omega_l)}{\omega_l^2 - \omega^2}, \tag{B.10}$$

which give the following form of the dyadic Green's function

$$\mathbf{G}(\mathbf{r}, \mathbf{r}'; \omega) = \sum_l c^2 \frac{\mathbf{f}_l^*(\mathbf{r}'; \omega_l) \mathbf{f}_l(\mathbf{r}; \omega_l)}{\omega_l^2 - \omega^2}. \tag{B.11}$$

By employing the mathematical identity [45]

$$\lim_{\eta \to 0} \mathrm{Im}\left[\frac{1}{\omega_l^2 - (\omega + i\eta)^2}\right] = \frac{\pi}{2\omega_l}\left[\delta(\omega - \omega_l) - \delta(\omega + \omega_l)\right], \tag{B.12}$$

we can relate the imaginary part of the dyadic Green's function to a simple sum over the field modes. We repeat that these field modes are the basis functions in a inhomogeneous environment for the electric field, as well as for the vector potential in the generalized Coulomb gauge. The resultant relationship is

$$\mathrm{Im}\left[\mathbf{G}(\mathbf{r}, \mathbf{r}'; \omega)\right] = \frac{\pi}{2} \sum_l \frac{1}{\omega_l} \mathbf{f}_l^*(\mathbf{r}'; \omega_l) \mathbf{f}_l(\mathbf{r}; \omega_l) \delta(\omega - \omega_l), \tag{B.13}$$

where we have dropped the term $\delta(\omega + \omega_l)$ from Eq. (B.12) that only contribute for non-physical negative frequencies. We note that we from this form also can construct the Green's function for a specific mode, e.g., a plasmonic mode on a nanowire.

# Appendix C

# Gauge dependent perturbation theory

In most practical calculations, two forms of the Hamiltonian for light-matter interaction are used: $\frac{q}{m}\mathbf{p}\cdot\mathbf{A}$ or $q\mathbf{E}\cdot\mathbf{r}$ both in the dipole approximation. In 1947 Lamb measured the spectrum of atomic hydrogen [3] and found that the results were described by the $q\mathbf{E}\cdot\mathbf{r}$ interaction Hamiltonian only. This result has often been misinterpreted as the two perturbations giving different physical results, and that only $q\mathbf{E}\cdot\mathbf{r}$ is the correct form of the interaction. Since then, the two forms have been shown to be connected through a unitary transformation, but the general attitude has been to use one form or the other with the same set of basis vectors (the proper method would also transform the basis vectors). For some processes this simply gives wrong results and has led to confusion in the literature. In 1976 Jaynes commented (cited from Ref. [115]): *"... a whole generation of physicists has stumbled on this problem and lived, not only under the shadow of the immediate difficulty: 'How can I ever know whether a practical calculation has been done right?', but the deeper mystery: 'How is it possible that a theory, for which formal gauge invariance is proved easily once and for all, can lead to grossly non-invariant results as soon as we try to apply it to the simplest real problem?'"*

We will in the following try to answer two relevant questions for the derivation presented in Chapter 3 in this thesis; 'What is the correct form of the mesoscopic interaction Hamiltonian, for use with the untransformed wavefunctions?'

and 'Is it necessary to transform the wavefunctions to get correct results?'

## C.1 In the dipole approximation

In the dipole approximation, theoretical, and due to Lamb, also experimental, arguments have been made as to why $q\mathbf{E}\cdot\mathbf{r}$ is the form that can be used without transforming wavefunctions. The argument relies on the proposal of an energy operator which generally is different from the Hamiltonian [115]. Especially it can be shown that the expectancy of the energy operator is gauge invariant while the expectancy of the Hamiltonian is not. In the case of the $q\mathbf{E}\cdot\mathbf{r}$-form of the interaction in the dipole approximation, it can be shown that the energy operator coincides with the unperturbed Hamiltonian, which ensures that the basis functions need not be transformed in this gauge to yield correct results, in general.

## C.2 Beyond the dipole approximation

The argument above, however, only works in the dipole approximation, so it does not imply that the multipolar Hamiltonian, which would be the natural generalization to the $q\mathbf{E}\cdot\mathbf{r}$-Hamiltonian, is the correct form of the interaction beyond the dipole approximation. In fact, it is written in Ref. [116] that *"It is the minimal coupling Hamiltonian, not the multipolar Hamiltonian, whose validity in time-evolution equations may be taken for granted."*

In the main text of the thesis we use the minimal coupling Hamiltonian in the generalized Coulomb gauge, and make the approximation that we only need to consider the constant term and the gradient term in the Taylor expansion for the field modes. It is from the above considerations not clear that this is the correct form of the Hamiltonian, in the sense that it would yield correct results without transforming the wavefunctions.

Without providing an answer to the first of the questions posed we proceed to the second, which is answered in the negative. For energy conserving transition processes, a hybrid approach is justified [57, 116], i.e., the wavefunctions do not need to be transformed in this case. This result applies to the dipole approximated form- as well as to the full interaction Hamiltonians. We study an intermediate form of the interaction, where neither the dipole approximation is

made nor the full spatial dependence is kept. As the calculations are correct for both extremes, we expect our calculations to be correct to the approximation order, i.e., to the first order in the Taylor expansion of the field modes.

# Appendix D

# Fabrication Recipies

The purpose of this appendix is to provide the details of the fabrication processes used to fabricate the samples described elsewhere in this thesis.

## D.1 The interface process

The interface process is repeated $n$ times to fabricate $2^n$ terraces into the surface of the sample. The direct and inverted sample each have 32 terraces corresponding to 5 repetition of the following process.

1. **Clean** sample in acetone, ethanol and isopropanol and blow dry with $N_2$ gun.
2. **Spin-coat** sample with AZ5214 photoresist using 6000 RPM for 30 s, after an initial distribution spin of 500 RPM for 5 s.
3. **Prebake** at 90 degrees Celsius for 60 s.
4. **UV exposure** for 20 s using a suitable mask that exposes half of the 32 terraces.
5. **Develop** in AZ351B:$H_2O$ mixed 1:5 for 40 s. Followed by $H_2O$ and $N_2$ gun.
6. **Postbake** at 120 degrees Celsius for 60 s.

7. **Ashering** in $O_2$-plasma at 40 % power setting for 60 s.

8. **Prepare deoxidation solution** as 10 mL of $H_3PO_4$ + 40 mL of $H_2O$, magnetic stirring for 5 min. at 500 RPM.

9. **Prepare etching solution** as 600 mL of $H_2O$ + 30 mL of $H_3PO_4$ (85%) + 10 mL $H_2O_2$ (30%), magnetic stirring for 30 min. at 300 RPM. Expected etch rate is $\sim 0.9$ nm/s.

10. **Calibrate etch rate** before each etch by etching on a dummy piece and measuring the resulting etch depth with a surface profiler.

11. **Etching** using this procedure: 30 s deoxidation, 10 s rinse in $H_2O$, blow dry with $N_2$ gun, etch for a time obtainable from the etch speed calibration. Rinse in $H_2O$ and blow dry with $N_2$ gun. It is important to replace the acid after each etching in order to maintain a constant etch rate.

12. **Clean** in acetone, ethanol and isopropanol and blow dry with $N_2$ gun.

By using 5 different masks and etching depths of L, 2L, 4L, 8L, and 16L one obtains 32 terraces equidistantly spaced L apart. The actual obtained depths were measured using a combination of secondary ion mass spectroscopy, atomic force microscopy, scanning electron microscopy, and surface profiling.

## D.2 Silver mirror process

After the interface process, the sample is subjected to an epitaxial lift-off and transferred onto a sapphire substrate. The epitaxial lift-off is detailed in the dissertation of Søren Stobbe [117]. The placement on a sapphire substrate allow us to excite and measure the quantum dots through the backside of the wafer, as the top of the wafer will be covered with silver.

1. **Epitaxial lift-off** of the top of the quantum dot wafer using a sapphire substrate with SU-8 as the destination substrate.

2. **Metal evaporation** in evaporation chamber. 200 nm of silver was evaporated onto the sample.

## D.3 The inverted interface process

The inverted interface process uses an epitaxial lift-off process, detailed in the dissertation of Søren Stobbe [117], to flip the surface of a wafer by transferring it onto a new destination substrate with the bottom side up. This enables processing of the semiconductor material immediately below the quantum dot layer. SU-8 is used for bonding to the destination substrate because it has a transmittance of 98 % for wavelengths above 560 nm and has excellent mechanical properties since it is epoxy-based. For that reason it is not dissolved in acetone which is central to make this process work.

1. **Spin-coat PMMA** on a $10 \times 10$ mm$^2$ silicon sample with polymethyl methacrylate in anisole (PMMA) 4% and bake on hotplate at 160 degrees Celsius for 60 s.

2. **Epitaxial lift-off** of the top of the quantum dot wafer using the silicon sample with PMMA as the destination substrate.

3. **Spin-coat SU-8** on a sapphire substrate. Use SU-8 2005 resist using 500 RPM for 60 s without prebake.

4. **Bond** the epitaxial lift-off film to the SU-8 by placing the silicon sample with PMMA and the ELO film on top of the sapphire with SU-8, so that the epitaxial lift-off film is in contact with the SU-8.

5. **Bake** at 120 degrees Celsius for 10 min. after which the hotplate should be turned off and allowed to cool slowly to avoid cracking of the SU-8 film.

6. **Remove PMMA** in acetone, discard the silicon substrate and if necessary remove residual PMMA using oxygen plasma.

7. **Perform the interface process** on the resulting sample which consists of an inverted epitaxial lift-off film bonded to sapphire by SU-8.

8. **Deoxidation** of surface before metal depostion, same deoxidation procedure as in the interface process.

9. **Metal Deposition** done in the same way as described in silver mirror process.

## D.4 Plasmonic gap waveguide process

First the relevant steps from the interface process is employed to produce a sample with the wanted distances to the quantum dots. The wafer piece will be mounted in the electron beam writer, therefore care should be made to choose a suitable sample size. We mounted the sample on an 8 mm slit, therefore the sample was made 10 mm wide. The spin coated resist is uneven near the edges of the sample, which should also be considered in the choice of sample size - our sample was $10 \times 12$ mm$^2$.

1. **Clean** sample in acetone, ethanol and isopropanol and blow dry with $N_2$ gun.

2. **Spin-coat** with The ZEP520A 3.7 %. First a distribution spin with an acceleration of 100 RPM/s to 500 RPM for 10 s. Immediately followed by an acceleration of 1500 RPM/s to 2000 RPM for 30 s.

3. **Bake** the sample at 180 degrees Celsius for 5 min on a silicon wafer.

4. **Inspect** the resulting resist. We found it to have a bluish color when the thickness is $\sim$ 100 nm. We also perfom a direct check of the resist thickness with a Filmtek machine.

5. **Electron-beam exposure** using a Jeol JBX-9300FS electron beam lithography system. Exposure using 100 kV acceleration voltage, current 6 nA, and dose 135, 145, 155, and 165 $\mu$C/cm$^2$. The multiple exposure values are used to counter variations in the resist thickness from sample to sample. We also fabricate plasmonic waveguides with different widths. For these structures the doses were 300, 320, 340, and 360 $\mu$C/cm$^2$.

6. **Develop** in ZED N-50 for 2 min., with manual stirring. Followed by 1 min. in isopropanol with manual stirring and jet from isopropanol squeezebottle. Hereafter thorough drying with $N_2$ gun.

7. **Inspect** the sample with atomic force microscope. As discussed in the main text, the degredation of the gap in the waveguides can be assesed with an atomic force microscope before further processing. If the degredation is found to be too severe, the sample can be cleaned and the process repeated.

8. **Cleaving.** We designed a sample with eigth identical subsamples and cleaved it correspondingly at this process step. This allowed us to have multiple tries at the rest of the process.

9. **Prepare deoxidation solution** as 10 mL of $H_3PO_4$ + 40 mL of $H_2O$, magnetic stirring for 5 min. at 500 RPM.

10. **Preparation of sample surface**, done immediately before metal evaporation. The sample is cleaned in $H_2O$ and dried with $N_2$ gun. Then ashering at 5% power setting for 10 s resulting in reducing the resist thickness by $\sim$ 2 nm. Followed by 30 s in deoxidation solution and 10 s in $H_2O$ and then dried with $N_2$ gun.

11. **Evaporation** of gold in a Physimeca metal evaporator. We deposit 15 nm at a rate of 0.5 nm/s.

12. **Lift-off** is done with a jet from an acetone squeezebottle followed by 10 min. in acetone bath. Hereafter $\sim$ 2 hours in R1165.

13. **Clean** in acetone and isopropanol and dry with $N_2$ gun.

The ZEP520A 3.7 % was prepared as a 1:2 solution of the available ZEP 520A 11% and anisole. The solution was left in a refrigerator and when taken out for use the bottle remained closed until temperature equilibrium with the room was established in order to avoid moisture in the solution, which degrades adhesion to the sample.

The spinning was showing effects of the small size of the sample with an uneven distribution as a result. We found that varying the acceleration of the spin could be used to form more uniform resist distributions.

The short ashering is done to remove any residue resist left in the exposed areas of the sample. The parameters used are a result of a study of the resist thickness reduction as function of power setting and time.

# Appendix E

# Optical measurement setups

Two different optical setups were used to perform the optical photoluminescence (PL) measurements presented in this thesis. The first (the ensemble setup), c.f Fig. E.1, was used to measure ensembles of quantum dots on the interface samples subject of Chapter 3 and Chapter 4 while the second setup, (the $\mu$-PL setup), c.f. Fig. E.2, was used to measure single quantum dots with a micron-sized spotsize on the plasmonic gap-waveguides subject of Chapter 5.

The two optical setups are very similar in function, and differ only in two aspects:

1. In the $\mu$-PL setup the excitation and collection is done confocally, whereas in the ensemble setup excitation and collection are independent of each other.

2. The excitation and collection area is much bigger in the ensemble setup than in the $\mu$-PL where it is diffraction limited.

Besides these optical differences, the stages are much coarser on the ensemble setup, and the cryogenic systems are different. The ensemble setup has a closed-cycle helium cryostat where the $\mu$-PL setup use a flow-cryostat. Further details on the optical setups can be found in the Ph.D. dissertation of Jeppe Johansen [118] (The ensemble setup) and Toke Lund-Hansen [119] (The $\mu$-PL setup).

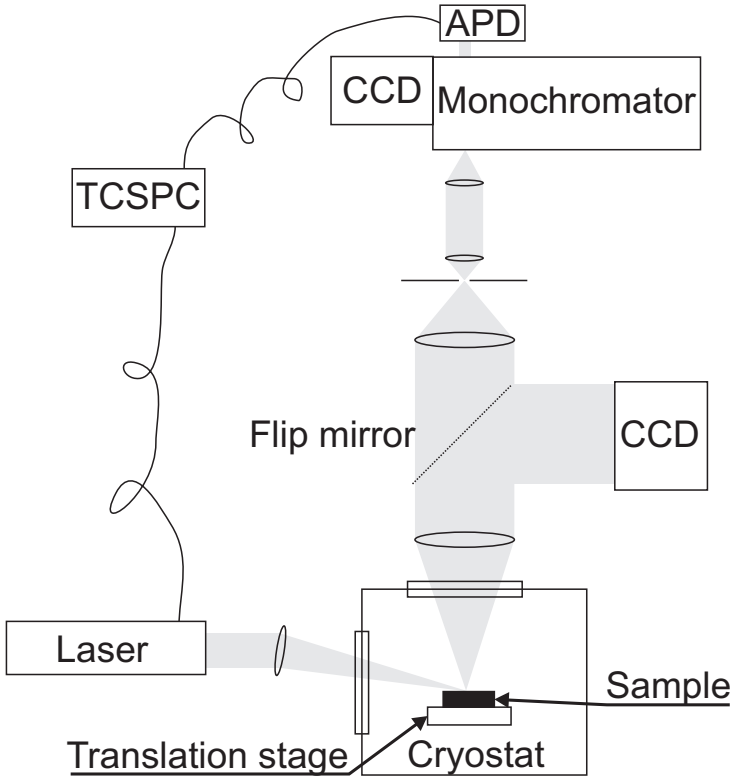


*Figure E.1: The ensemble setup. The sample is kept in a closed-cycle cryostat, mounted on an xyz-stage, and pumped near the Brewster angle with p-polarized light to minimize reflections. The emitted and/or scattered light can be directed onto a CCD camera for alignment or directed through a pinhole for spatial selection to a monochromator. The spatially dispersed light can then either be directed to a CCD camera for acquisition of spectra or onto an avalanche photodiode (APD) for time-resolved measurements. The arrival time of single photons on the APD are correlated to the emission time of laser pulses with time-correlated single-photon counting (TCSPC) hardware.*

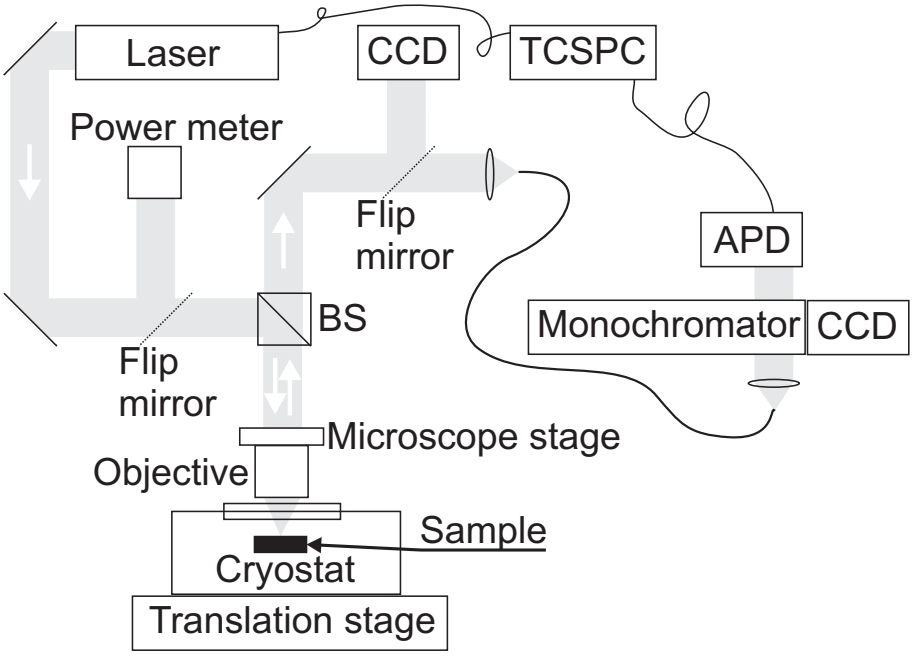


*Figure E.2: The $\mu$-PL setup. The sample is kept in a flow cryostat which is mounted on an xyz-stage. The excitation and collection optics are confocal and the emitted and/or scattered light can be directed onto a CCD camera for alignment or directed through a single-mode fiber for spatial selection to a monochromator. The spatially dispersed light can then either be directed to a CCD camera for acquisition of spectra or onto an avalanche photodiode (APD) for time-resolved measurements. The arrival time of single photons on the APD are, as was also the case for the ensemble setup, correlated to the emission time of laser pulses with time-correlated single-photon counting (TCSPC) hardware.*

# Appendix F

# Effect of the backside sapphire-substrate

In this appendix we show the resulting normalized decay rate for an emitter positioned in GaAs between a silver mirror and a sapphire substrate, like in the direct and inverted samples studied in Chapter 4. In the two samples studied in Chapter 4, the distance to the sapphire was fixed and the distance to the silver mirror was varied. The calculation is done using the dyadic Green's function presented in Appendix A.

The distance-dependencies to both silver and sapphire give rise to oscillations. The silver mirror results in a stronger oscillation as this is more reflecting than the sapphire substrate. The decay rates shown in Fig. F.1 contain the region relevant for the direct (623 nm) and inverted (302 nm) structures.

In Fig. F.2, we show the result for larger distances to the sapphire substrate. The dependence on the distance to the sapphire is seen even for distances larger than two microns as a "ringing" in the normalized decay rate.

We note that due to the fabrication procedure, the bordering material on the backside of the wafer is actually SU-8 which has a thickness of several micrometer ($\sim 10$ μm) and lies between the wafer and the sapphire substrate. We have modeled the decay dynamics with a backside refractive index $n = 1.75$ corresponding to a sapphire, but should have used $n = 1.56$ corresponding to SU-8 [120]. The difference between the two is, however, negligible in our structures.

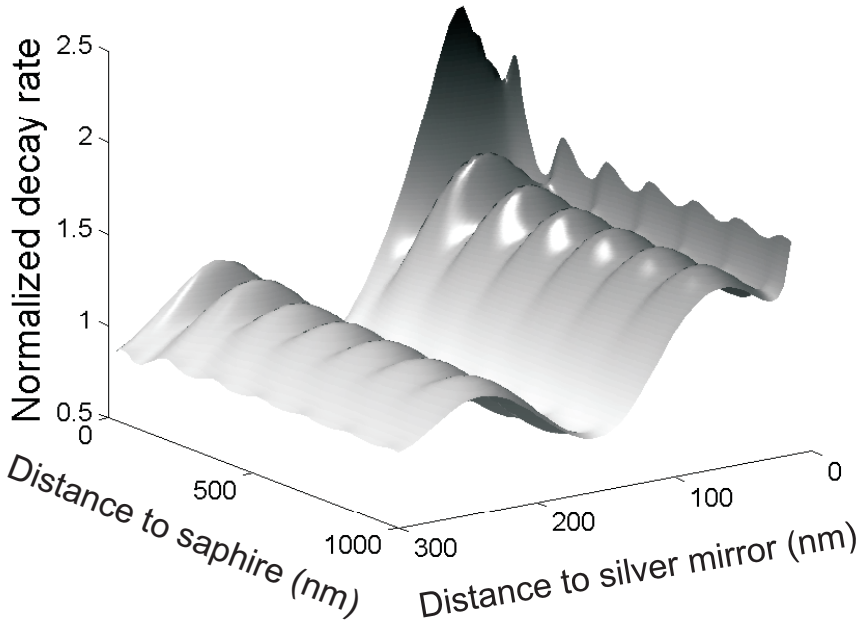


*Figure F.1: Normalized decay rate as function of distance to a silver mirror and to a backside sapphire substrate. Both distance dependencies give rise to a damped oscillation, with the stronger oscillation associated with the distance to the silver mirror.*

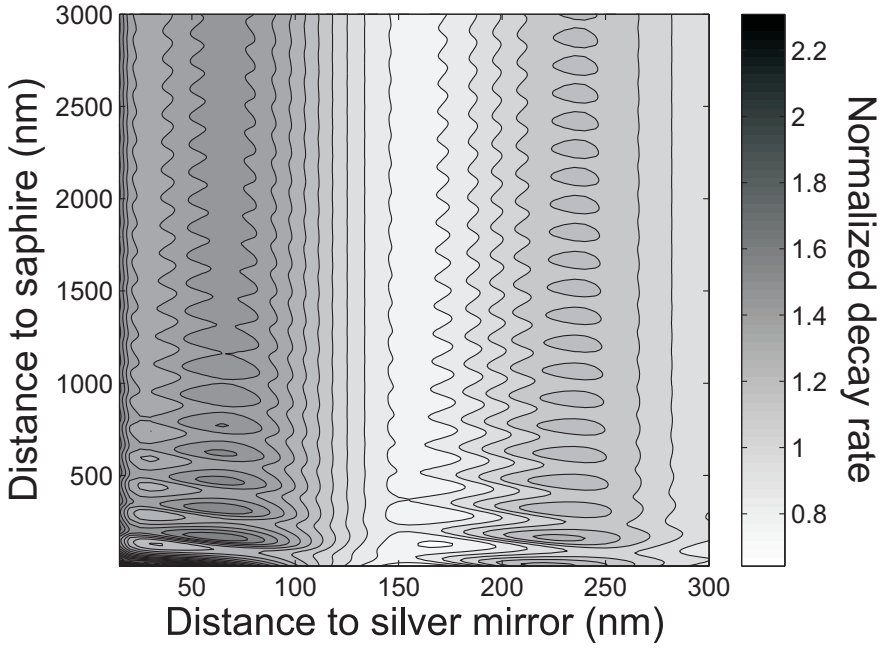


*Figure F.2: Normalized decay rate as function of distance to a silver mirror and to a backside sapphire substrate. The dependence of the decay rate on the distance to the sapphire substrate is clearly seen even for distances larger than 2 microns.*

# Appendix G

# Coupling to plasmonic modes beyond the dipole approximation

## G.1 Polarization considerations

The mesoscopic moments $\Lambda_{x,z}$ and $\Lambda_{z,x}$ couple to two different polarizations of the plasmonic field. We can study the different contributions by employing a single-mode model of the plasmonic field:

$$\mathrm{Im}(\mathbf{G}^{\mathrm{pl}}_{j,j'}(\mathbf{r},\mathbf{r}';\omega)) = \frac{\pi}{2\omega} f^{\mathrm{pl}}_{j}(\mathbf{r}) f^{\mathrm{pl}*}_{j'}(\mathbf{r}')\delta(\omega-\omega_{\mathrm{pl}}). \tag{G.1}$$

Here the field modes are given in term of the electric field for the surface plasmon polaritons $\mathbf{f}^{\mathrm{pl}}(\rho,z) \propto (E_{\parallel},E_z)e^{i(k_{\parallel}\rho+k_z z-\omega t)}$. The mesoscopic moment $\Lambda_{z,x}$ couples to $F_1 = \partial/\partial x f^{\mathrm{pl}}_z(\mathbf{r})$ and $\Lambda_{x,z}$ couples to $F_2 = \partial/\partial z f^{\mathrm{pl}}_x(\mathbf{r})$. We use the well-known [17] polarization and dispersion of surface plasmon polaritons introduced in Chapter 2 to find the ratio of the gradients that $\Lambda_{z,x}$ and $\Lambda_{x,z}$ couples to: $F_1/F_2 = |\epsilon_m/\epsilon_d| = 4.3$. Due to this large ratio we choose to neglect $\Lambda_{x,z}$, that couples to the weaker field, and define the moment $\Lambda$ used in the main text as $\Lambda = \Lambda_{z,x}$, with the added benefit of only having a single fitting parameter $\Lambda/\mu$ in the expression for the normalized decay rate.

## G.2 Modeling of the contributions from the two mesoscopic moments

In addition to the arguments above, we here also explicitly plot the effect of the two different moments of various sizes. In Fig. G.1 we plot two series of normalized decay rates, both with the dipole moment parallel to the interface $\mu = \mu_x$. In the first of these decay rate series we vary $\Lambda_{z,x}$ and have $\Lambda_{x,z} = 0$, and in the second we vary $\Lambda_{x,z}$ and set $\Lambda_{z,x} = 0$. We plot the normalized total, plasmon, and radiative decay rates, and find that the decay rate depends strongly on the sign and size of the $\Lambda$'s. Furthermore, we find that the result of including each of the two $\Lambda$'s is very different.

We have decomposed the decay rate to its constituent components (radiative, plasmon, and lossy modes), though we have not shown the behavior of the lossy modes explicitly as it only contributes significantly to the total decay rate for the innermost $\sim$ 25 nm. The ratio of $\Lambda$ and $\mu$ can be given in a length unit, and here we plot the resulting normalized decay rate for $\Lambda/\mu = (-10, -5, 0, 5, 10)$ nm, as this is the range of parameters needed to fit our measurements. Note that $\Lambda/\mu = 0$ nm corresponds to modeling a point-dipole. We find that within the shown parameter range that the dominating effect on the decay rate stems from the coupling to plasmons mediated by $\Lambda_{z,x}$ in agreement with the above considerations.

## G.3 Distance independent breakdown of the dipole approximation

We note that the first-order moment $\Lambda$ couples to the gradient of the Green's function while the point-dipole moment $\mu$ couples to its size, as derived in Chapter 3. For coupling to the plasmonic modes this corresponds to a scaling proportional to $ik_{\mathrm{pl}}\Lambda e^{ik_z z}$ for the mesoscopic contribution, and $\mu e^{ik_z z}$ for the dipole contribution. The breakdown of the dipole approximation is determined by the ratio of the zeroth and first-order moments, which, thus, is independent of the distance $z$ to the silver mirror. The breakdown does not scale with the strength of the plasmonic field but with its gradient. To further investigate this we have fitted our data sets excluding a number of the innermost points

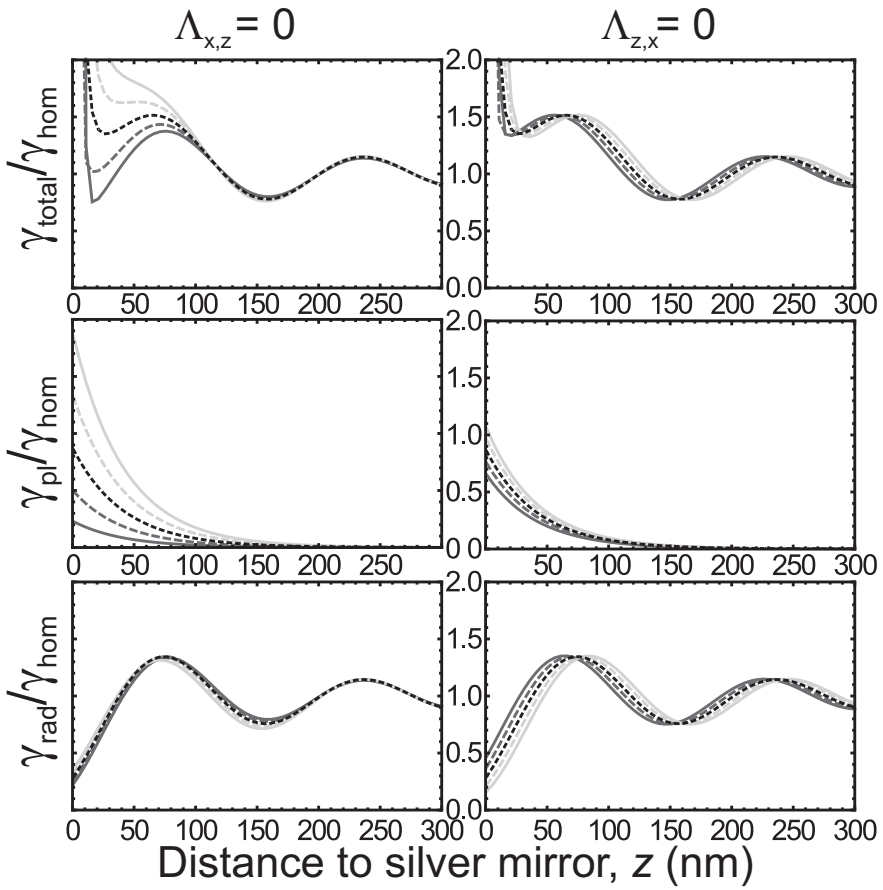


*Figure G.1: Normalized decay rates beyond the dipole approximation. For a dipole oriented parallel to the interface we study the effect of $\Lambda_{z,x}$ (left plots) and $\Lambda_{x,z}$ (right plots). From top to bottom we plot: the total decay rate, the decay rate into plasmon, and the decay rate into free photons. We set the $\Lambda/\mu$ to* -10 nm *(solid light gray)*, -5 nm *(dashed light gray)*, 0 nm *(dotted black = dipole result)*, 5 nm *(dashed dark gray)*, 10 nm *(solid dark gray)*

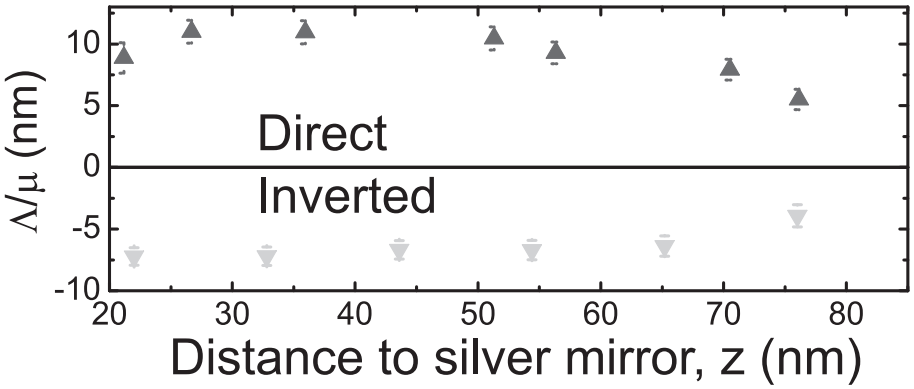


*Figure G.2: Extracted mesoscopic moment as function of the innermost included point in the fitting procedure, i.e., by including only data points for the specific- and longer distances.*

in a systematic way. The resulting mesoscopic moments are shown in Fig. G.2. The extracted mesoscopic moment is seen not to depend on the distance to the interface. However, the effect of the breakdown on the total decay rate falls off with the plasmonic field strength.

# Appendix H

# Orientation and position dependent coupling to plasmon waveguides

## H.1 Silver nanowire

The nature of the coupling of a mesoscopic quantum dot to a silver nanowire as presented in Chapter 4 is determined by which excited state that is prepared in the quantum dot. Real quantum dots support two excited states that are non-degenerate due to the broken in-plane rotational symmetry. In the nanowire coordinate system introduced in Chapter 4 these correspond to an azimuthally and parallelly oriented dipole when the quantum dots are directly beneath or above the nanowire.

When quantum dots are excited non-resonantly, both excited states are populated, and hence a multi-exponential decay will result. Here, we will show the result for each of the two excited states by themselves. Like in Chapter 4 we show the decay dynamics for a range of quantum dots with different mesoscopic character $\Lambda/\mu$ and for a range of distances to the nanowire $d$.

The decay dynamics of these two excited states are very different as we will show in this appendix. In the case where the quantum dot is directly underneath or above the nanowire as shown in Chapter 4, the excitation oriented

azimuthally do not couple to the wire. Neither the purely dipole nor mesoscopic moment contribute to the coupling.

For the silver nanowire calculations presented here we use the same parameters as in Chapter 4, i.e., a quantum dot emission wavelength of 1030 nm and a silver nanowire with a diameter of 25 nm ($r = 12.5$ nm) embedded in GaAs.

For the parallelly oriented excited state shown in Fig. H.1, we find that for a pure dipole emitter $\Lambda/\mu = 0$, there is a significant coupling to the nanowire. As a result there is interference between the dipole and mesoscopic moments, and the resulting coupling is dependent on the sign of $\Lambda$ as shown in Fig. H.1.

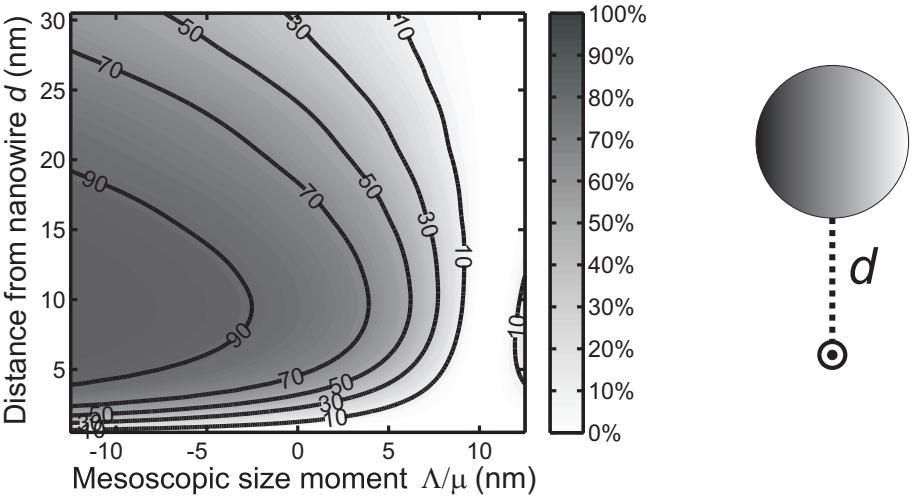


*Figure H.1: Coupling efficiency of an excited state that is oriented parallelly to the nanowire. The result is shown for a range of quantum dots with different mesoscopic character $\Lambda/\mu$ and for a range of distances to the nanowire d.*

We find that for a pure dipole $\Lambda/\mu = 0$ nm positioned 10 nm from the wire that the efficiency is $\beta = 85\%$. This number can be reduced to below 1% for $\Lambda/\mu = +10$ nm and enhanced to $\beta = 96\%$ for $\Lambda/\mu =$ -10 nm.

When the quantum dot is moved away from these positions of high field symmetry relative to the quantum dot states, the excited state that was originally purely along the azimuthal direction also gains a component along the radial direction relative to the wire. In these cases the resulting decay dynamics

become even more complex. We study the decay dynamics for the two excited quantum dot states individually when shifting the quantum dot sideways from an initial position 10 nm directly below/above the wire. This theoretical study resembles the experimental condition where the exact in-plane positions of the quantum dots are unknown.

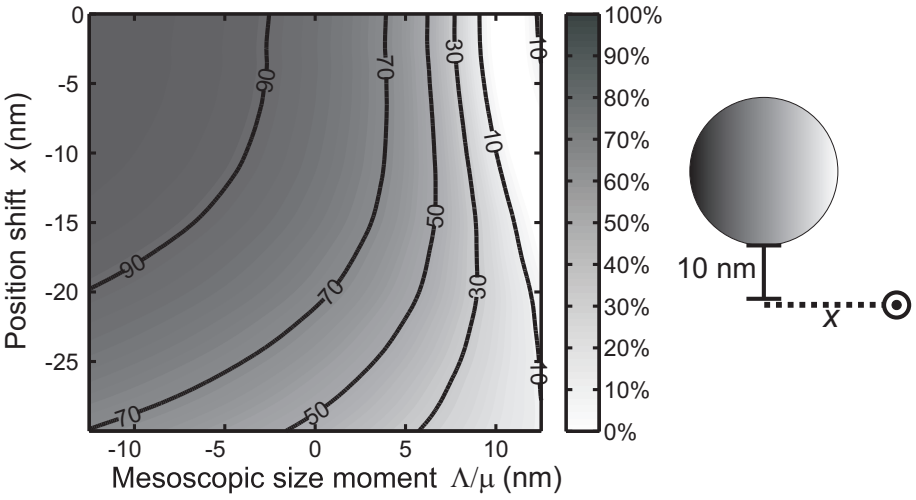


*Figure H.2: Coupling efficiency of an excited state that is oriented parallelly to the nanowire. The result is shown for a range of quantum dots with different mesoscopic character $\Lambda/\mu$ and for a range of distances to the highly symmetric starting point ($x = 0$).*

In Fig. H.2 we see that the result of shifting the quantum dot with an parallelly excited state away from the position directly underneath the wire generally diminishes the coupling. For the dipole contribution $\Lambda/\mu = 0$ nm the effect is purely due to the growing distance to the wire with the in-plane position shift.

The other excited quantum dot state is oriented parallel to the x-axis that we shift along as shown in Fig. H.3. At the starting point, $x = 0$, the emitter does not couple to the wire at all, but when the emitter is shifted along $x$

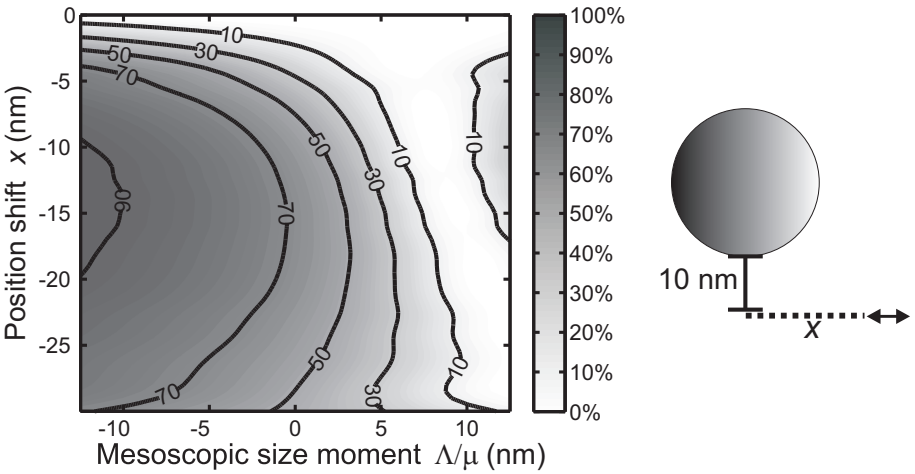


*Figure H.3: Coupling efficiency of an excited state that is oriented along the x-direction, see sketch. The result is shown for a range of quantum dots with different mesoscopic character $\Lambda/\mu$ and for a range of distances to the highly symmetric starting point ($x = 0$).*

the exited state can couple to the radial component of the plasmonic mode which gives rise to a significant coupling. The interference with the mesoscopic moment further alter the decay dynamics as shown in Fig. H.3. The uneven structure of the graphs is due to the finite mesh resulting from the finite-element calculation.

## H.2 Gold narrow-gap waveguide

For the calculation of the coupling to a gold narrow-gap waveguide we use the same parameters as in Chapter 5, i.e., a quantum dot emission wavelength of 920 nm and a gold gap waveguide with stripe widths of 250 nm placed atop the quantum-dot-containing GaAs wafer and with air as the top material. In the present calculations the width of the gap is 25 nm and we consider, like in Chapter 5, the coupling to the fundamental guided gap mode.

The resulting coupling efficiencies are shown, for quantum dot excitations

oriented along the $x$-axis for a range of distances to the interface while $x = 0$, in Fig. H.4. In Fig. H.5 and Fig. H.6 the coupling efficiency is shown for a range of position shifts along the $x$-axis. The distance to the interface is, in these plots, fixed at $d = 10$ nm and the results are shown for both an excited state oriented along the $x$- and $y$-axis.

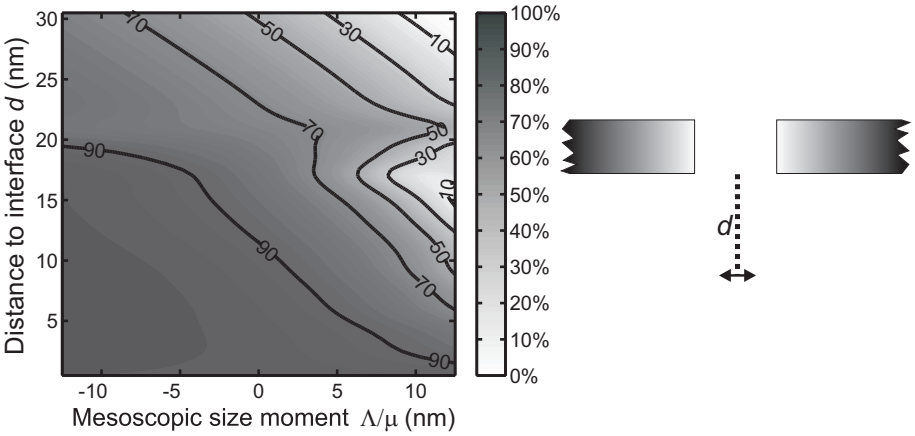


*Figure H.4: Coupling efficiency for quantum dot excitations oriented along the $x$-axis, see sketch, for a range of distances to the interface while retaining $x = 0$.*

The results shown on the coupling to a narrow-gap gold waveguide (Fig. H.4, Fig. H.5, and Fig. H.6) illustrate again the potential of utilizing the mesoscopic moment to enhance the coupling to guided modes. Note, that like for the nanowire calculations and the silver mirror measurements, we here find that the quantum dot should be turned upside-down to increase the coupling to the plasmonic mode, i.e., the best coupling occur for $\Lambda/\mu < 0$ nm. Upside-down should be understood as compared to a normal monolithic process where the waveguides are defined on top of the quantum dot layer. Note that we here, i.e. for a small gap (25 nm), find that the dipole moment oriented along $x$ give rise to the most efficient coupling to the nanowire. This was not the case in Chapter 5 where the $y$-component gave comparable, and even larger, contributions when the emitter was offset from the $x = 0$ position.

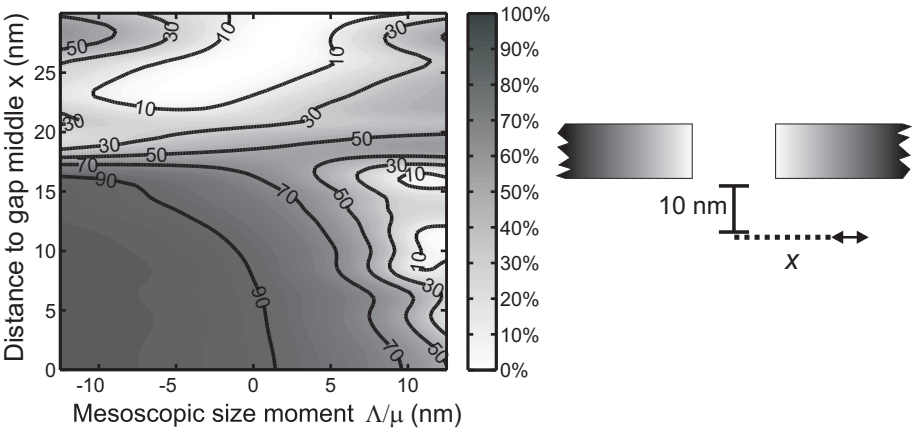


*Figure H.5: Coupling efficiency for a range of position shifts along $x$ while keeping the distance to the interface fixed at $d = 10$ nm for an excited state oriented along the $x$-axis.*

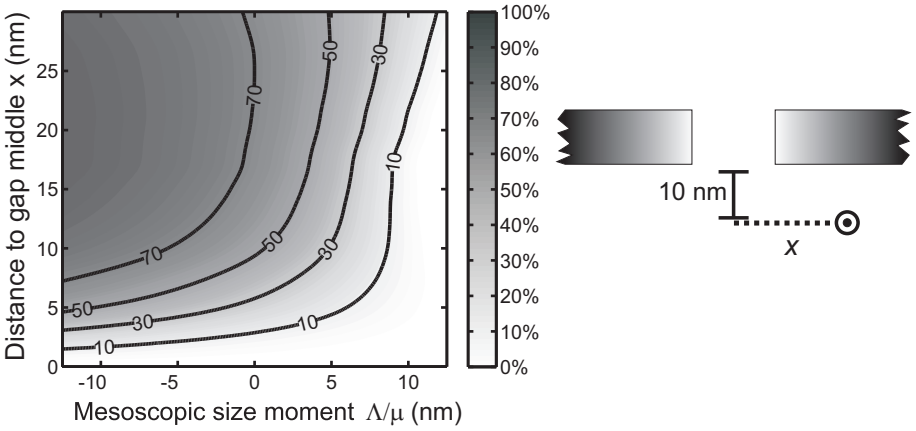


*Figure H.6: Coupling efficiency for a range of position shifts along $x$ while keeping the distance to the interface fixed at $d = 10$ nm for an excited state oriented along the $y$-axis.*

# Appendix I

# Microscopic theories for the mesoscopic moments

In this appendix we will construct two microscopic models for $\mu$ and $\Lambda$ in an attempt to model the quantum dot properties that we extracted through the fitting procedure described in Chapter 4. Both models are dependent on gradients of the electron and hole wavefunctions in the $z$-direction. The first approach explore effects stemming from the envelope functions while the second explore the effect on the crystal-unit-cell length scale.

## I.1 Effect of gradients on the envelope function overlap

We use the approximation that the envelope function does not change significantly over the span of a crystal unit cell [37] to evaluate the dipole moment as $\mu_x = \langle F_e|F_h\rangle\langle u_{c,0}|p_x|u_{v,0}\rangle$. In a similar manner the mesoscopic moment $\Lambda_1 = \Lambda_{z,x} = \hbar/(m\omega_0)\langle F_e|\partial/\partial z|F_h\rangle\langle u_{c,0}|p_x|u_{v,0}\rangle$ and $\Lambda_2 = \Lambda_{x,z} = \langle F_e|(z - z_0)|F_h\rangle\langle u_{c,0}|p_x|u_{v,0}\rangle$ can be calculated. In this description we can calculate the experimentally important ratios $\Lambda_1/\mu$ and $\Lambda_2/\mu$ solely from the envelope functions of the electron and hole states. The electron and hole envelope functions can be found as eigenstates to a Schrödinger like effective mass equation [31], where a spatially varying potential defines the quantum dot. The mod-

eled potential have a constant depth throughout the quantum dot, set by the amount of In in the quantum dot, In(x)Ga(1-x)As, we used $x = 0.46$ which have been used to model similar quantum dots successfully [31]. The shape of the quantum dot is defined as a rotationally symmetric half-ellipsoid where the diameter at the bottom $D$ and height $h$ are defining the shape of the quantum dot. We employ a COMSOL code to solve the equations for electron and hole envelope function [31], for a range of different quantum dot parameters. In Fig. I.1(a,b) we show the resulting envelope functions for the electron and the hole in a quantum dot with a height of 7 nm and with $D = 20$ nm. We note that the hole envelope functions is much stronger confined to the quantum dot than the electron envelope function, due to the larger effective mass of holes in the quantum dot.

The calculated envelope functions are used to numerically estimate the size of the mesoscopic moments. We define the envelope overlaps $EO = \langle F_e|F_h\rangle$, $EO_1 = \hbar/(m\omega_0)\langle F_e|\partial/\partial z|F_h\rangle$ and $EO_2 = \langle F_e|(z-z_0)|F_h\rangle$ that are proportional to the dipole moment $\mu_x^{cv} = EO\langle u_{c,0}|p_x|u_{v,0}\rangle$ and the first order moments $\Lambda_{1,2} = EO_{1,2}\langle u_{c,0}|p_x|u_{v,0}\rangle$, respectively.

Before proceeding further, we note that our envelope function model is an oversimplified representation of real quantum dots. The physical dipole moment (not transition dipole moment) of quantum dots has been measured [84]. The conclusion from these experiments is that the hole envelope function is shifted towards the apex of the quantum dot along the $z$-axis. The relative offset of the envelope functions is caused by In redistribution in the quantum dot under self-assembly, resulting in a higher In concentration towards the apex of the quantum dot. Here we will mimic a more complete quantum dot model by artificially introducing a shift along the $z$-axis of the envelope functions relative to each other.

Including this shift we first calculate the simple envelope functions overlap $EO$, see Fig. I.1e. Note that we have done the calculations even for very large shifts compared to the quantum dot heights, which naturally leads to a drop in $EO$ for large shifts. Previous work on quantum dot envelope functions [29, 31] extracted an overlap $EO \approx 0.8$, which compared with Fig. I.1e indicates that shifts larger than $\sim 3$ nm should not be considered representative of real quantum dots.

We find that the mesoscopic envelope overlaps $EO_{1,2}$, plotted in Fig. I.1(c,d),

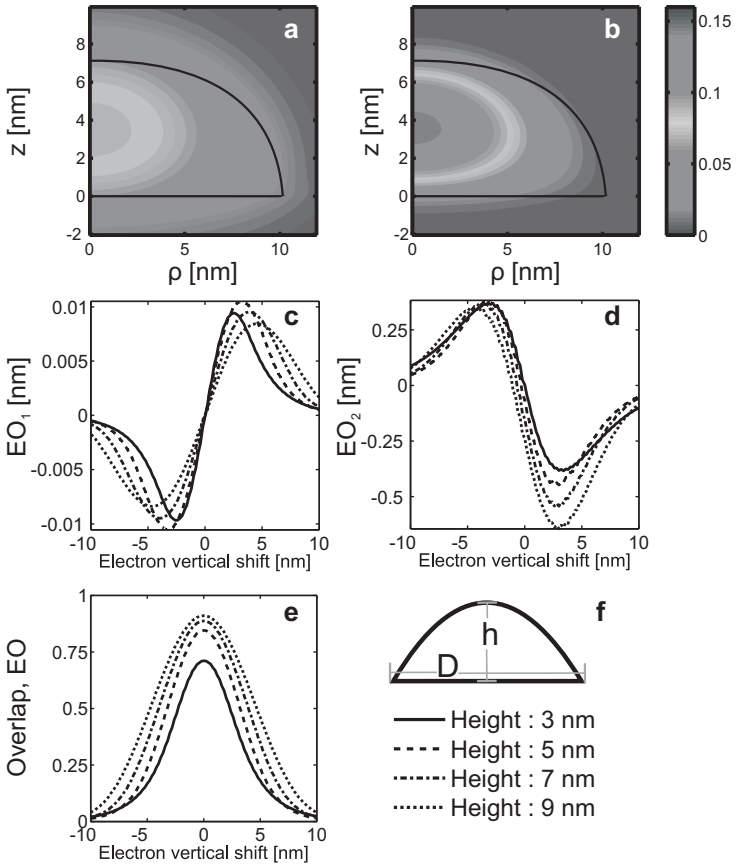


*Figure I.1: Envelope function for electron (***a***) and hole (***b***) in a quantum dot. The results in* **c**, **d**, *and* **e** *are shown for a series of quantum dot heights (as explained in* **f***) as function of envelope function position shift, while the ratio of diameter to height have been kept constant* $D/h = 2.86$. **c**, *The first order overlap* $EO_1$. **d**, *The first order overlap* $EO_2$. **e**, *The overlap of electron and hole,* $EO$.

are very sensitive to the relative shift of the envelope functions. The size of the resulting first order overlaps $|EO_1|$ and $|EO_2|$ have a maximum for a shift of a few nanometers, and is dependent on the quantum dot height. In order to compare the first-order envelope overlap with first-order mesoscopic moment that we extracted through a fit, we should compare $EO_1/EO$ to $\Lambda_1/\mu$ and $EO_2/EO$ to $\Lambda_2/\mu$. We will focus our conclusion on $\Lambda_1/\mu$ as this is the moment important for the experiment in Chapter 4. The resulting values from the microscopic theory are three orders of magnitude smaller than the $\Lambda_1/\mu$-value that we extracted through a fit to our measured data. This microscopic models ability to explain a large mesoscopic moment rely on the presence of very strong gradients in the envelope function. Large gradients could occur for changes in the wavefunction over shorter lengthscales. Thus, the numerical results presented here suggest that the reason for the large mesoscopic moments should not be found on the length scale of the envelope function, but rather at the nanoscopic crystal level.

## I.2 Effect of a periodicity-shift in the Bloch functions

In this section we explore the outcome of gradients at the crystal-unit-cell level. InAs and GaAs have slightly different lattice constant, which is the reason for the self-formation of quantum dots. The quantum dots, that consist of InGaAs are embedded in GaAs which give rise to a shift of the lattice constant throughout the quantum dot. Such an effect have been directly observed in recent high resolution transmission electron microscopy studies [121]. A sharp gradient of the in-plane crystal-lattice-constant along the $z$-axis (see Fig. I.2a) could lead to a large mesoscopic moment.

We here propose a simple model for such an effect, with the following form of the electron and hole wavefunctions.

$$|c\rangle = F_e(\mathbf{r})u_c(\mathbf{r},\mathbf{r}') \tag{I.1}$$

$$|v\rangle = F_h(\mathbf{r})u_v(\mathbf{r},\mathbf{r}') \tag{I.2}$$

where $F_e$ and $F_h$ are envelope functions that vary slowly over the size of a crystal unit cell, and the Bloch functions are periodic in $\mathbf{r}$ with the size of the unit cell. Furthermore, the size of the unit cell (and hereby the periodicity

of the Bloch function) is dependent on position as given by $\mathbf{r}'$. We make the anzats that the Bloch functions are given in the following simple way with $\mathbf{r} = (x, y, z)$,

$$u_c(\mathbf{r}, \mathbf{r}') = \sum_n a_n \cos(nk_0(\mathbf{r}')x) \tag{I.3}$$

$$u_v(\mathbf{r}, \mathbf{r}') = \sum_n b_n \sin(nk_0(\mathbf{r}')x). \tag{I.4}$$

This anzats ensures opposite parity of the conduction and valence band Bloch-functions, and that the quantum dot only have an in-plane dipole moment. The model only give rise to a dipole moment along $x$ but can easily be expanded to include a $y$ dipole as well. Furthermore, we implicitly assume, i.e. by disregarding changes in the expansion coefficients $a_n$ and $b_n$ with $r'$, that the shape of the Bloch functions remain the same, and thus that only their periodicity is effected. We calculate the $x$-dipole moment $\langle c|p_x|v\rangle$ in this model, where we use that $p_x = i\hbar\partial/(\partial x)$ to get

$$\langle c|\frac{\partial}{\partial x}|v\rangle = \int d\mathbf{r} F_e^*(\mathbf{r}) F_h(\mathbf{r}) \langle c|v\rangle_{\mathrm{B}}, \tag{I.5}$$

where

$$\langle c|v\rangle_{\mathrm{B}} = \sum_n \int_{dV} d\mathbf{r} a_n^*(\mathbf{r}) b_n(\mathbf{r}) n k_0(\mathbf{r}) \cos^2(nk_0(\mathbf{r})x). \tag{I.6}$$

In this derivation we made the approximation that $\partial k_0(\mathbf{r})/\partial x$ does not take large values, corresponding to the periodicity of the unit cells changing slowly perpendicular to the growth axis. The expression for the x-dipole transition moment bears much resemblance to the expression derived earlier. Furthermore, the $z$-transition dipole moment equals zero, consistent with measurements on real quantum dots. With these initial tests in place we go on to construct the higher order moments of interest to this study. We find that

$$\langle c|z\frac{\partial}{\partial x}|v\rangle = \int d\mathbf{r} F_e^*(\mathbf{r}) F_h(\mathbf{r}) z \langle c|v\rangle_{\mathrm{B}} \tag{I.7}$$

and

$$\langle c|x\frac{\partial}{\partial z}|v\rangle = \int d\mathbf{r} F_e^*(\mathbf{r}) F_h(\mathbf{r}) \frac{x^2}{\Delta z} \frac{\Delta k_0}{k_0(\mathbf{r})} (\Delta(z - z_{\mathrm{top}}) - \Delta(z - z_{\mathrm{bot}})) \langle c|v\rangle_{\mathrm{B}}. \tag{I.8}$$

Where Eq. (I.8) corresponds to the moment extracted in Chapter 4. We have used that there is a sharp transition in the periodicity of the crystal lattice $\Delta k_0/\Delta z$ along the $z$-axis at the top ($z = z_{\text{top}}$) and at the bottom ($z = z_{\text{bot}}$) of the quantum dot [121]. The use of $\Delta$ is to signify that the periodicity-shift occurs over a region with width $\Delta z$ around $z_{\text{top}}$ or $z_{\text{bot}}$.

The resulting expression for $\langle v|x\partial/\partial z|v\rangle$ depends quadratically on the in-plane size of the quantum dot, and will therefore grow to be large for large quantum dots. To numerically evaluate this model we use the same model for the envelope function as above, and use the shift in lattice vector $\Delta l = 0.093$ nm obtainable from Ref. [121] at the top of the quantum dot. We assume that the bottom transition does not overlap significantly with the envelope functions, as the hole is shifted upwards in real quantum dots, and vary only the position of the top transition. Also including the bottom transition diminishes the resulting mesoscopic moment. The results shown here, i.e. for only the top-transition, is therefore an ideal case.

We find, as shown in Fig. I.2, that our numerical results confirm that the overlap moment grows with the quantum dot size as shown in Fig. I.2b. Furthermore, we see that for a fixed quantum dot volume, the effect grows for flatter quantum dots, as shown in Fig. I.2c. Importantly, the resulting numbers are two orders of magnitude larger than the findings from the envelope gradient approach of the previous section, and are easily within an order of magnitude of the measured results ($\Lambda/\mu \approx \pm 10$ nm). This suggest that the description for the large measured mesoscopic moments should be found at the nanoscopic crystal length scale. The size of the effect is dependent on the mesoscopic size and shape of the quantum dots. A thorough study of real quantum dot shapes and internal crystal structure need to be performed in order to test the validity of this simple model.

Our microscopic models indicate that the origin of the mesoscopic moment is found at the interplay between the mesoscopic envelope function size and changes in the crystal lattice structure. The effects are thus critically dependent on detailed knowledge of the crystal lattice structure and material composition throughout the quantum dot.

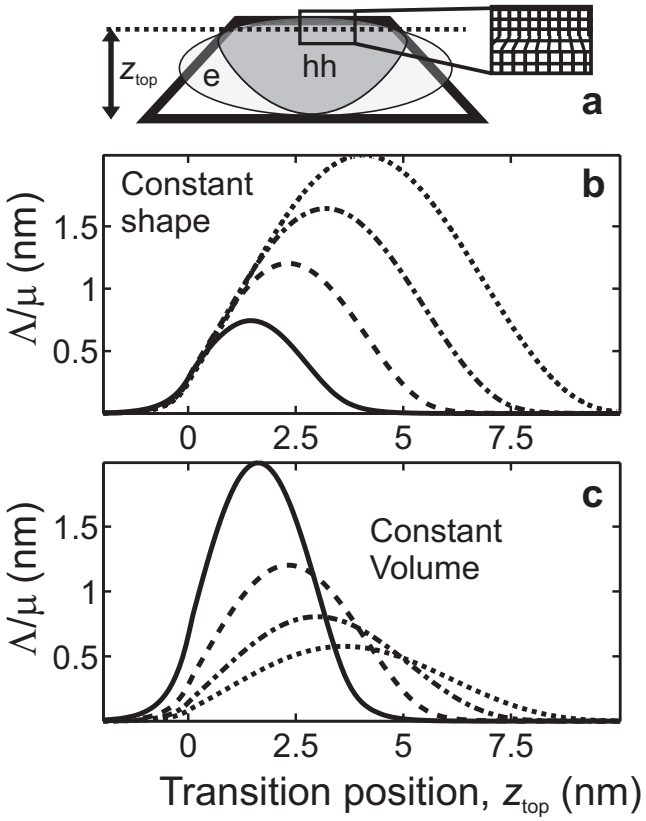


*Figure I.2: Mesoscopic moments induced by periodicity shift in quantum dot Bloch functions.* **a**, *Sketch of the effect: We model the effect of a shift in the crystal lattice periodicity at a certain position* $z_{\mathrm{top}}$, *within the envelope function overlap.* **b**, *The resulting first-order moment* $\Lambda_1/\mu$ *for quantum dots of various size. The diameter to height ratio is fixed at* $D/h = 4.7$ *and the height of the quantum dot set to* 3 nm *(solid lines),* 5 nm *(dashed lines),* 7 nm *(dash-dotted lines), and* 9 nm *(dotted lines). The lines indicate* $\langle v|x\partial/\partial z|v\rangle/\langle v|\partial/\partial x|v\rangle$ *which can be directly compared to the measured values of* $\Lambda/\mu$. **c**, *The resulting first-order moment for various geometries. Same convention as above for linetype to quantum dot height, here the volume* ($V \approx h(D/2)^2 = 700$ nm$^3$) *is kept constant. We note that the envelope function overlap is larger than 80% for all the shown calculated quantum dot realizations, and thus consistent with experiments [29, 31].*

# Bibliography


[1] P. A. M. Dirac, The quantum theory of the emission and absorption of radiation, *Proceedings of the Royal Society of London. Series A, Containing Papers of a Mathematical and Physical Character* **114**, 243–265 (1927).

[2] E. Fermi, Quantum theory of radiation, *Rev. Mod. Phys.* **4**, 87 (1932).

[3] W. E. Lamb & R. C. Rutherford, Fine structure of the hydrogen atom by a microwave method, *Phys. Rev.* **72**, 241–243 (1947).

[4] E. Purcell, Proceedings of the American Physical Society, *Phys. Rev.* **69**, 674 (1946).

[5] H. Casimir, *Proc. Kon. Ned. Akad. Wetensch.* **51**, 793 (1948).

[6] A. Einstein, B. Podolsky, & N. Rosen, Can quantum-mechanical description of physical reality be considered complete?, *Phys. Rev.* **47**, 777–780 (1935).

[7] J. S. Bell, On the problem of hidden variables in quantum mechanics, *Rev. Mod. Phys.* **38**, 447–452 (1966).

[8] A. Aspect, P. Grangier, & G. Roger, Experimental tests of realistic local theories via Bell's theorem, *Phys. Rev. Lett.* **47**, 460–463 (1981).

[9] D. Bouwmeester, *et al.*, Experimental quantum teleportation, *Nature* **390**, 575–579 (1997).

[10] J. F. Sherson, *et al.*, Quantum teleportation between light and matter, *Nature* **443**, 557–560 (2006).

[11] J. D. Jost, *et al.*, Entangled mechanical oscillators, *Nature* **459**, 683–685 (2009).

[12] E. Togan, *et al.*, Quantum entanglement between an optical photon and a solid-state spin qubit, *Nature* **466**, 730–734 (2010).

[13] T. D. Ladd, *et al.*, Quantum computers, *Nature* **464**, 45–53 (2010).

[14] C. H. Bennett & G. Brassard, Quantum cryptography: Public key distribution and coin tossing, in *IEEE International Conference on Computers, Systems, and Signal Processing*, 175–179 (Bangalore, 1984).

[15] E. Knill, R. Laflamme, & G. J. Milburn, A scheme for efficient quantum computation with linear optics, *Nature* **409**, 46–52 (2001).

[16] K. Vahala, Optical microcavities., *Nature* **424**, 839–846 (2003).

[17] S. A. Maier, *Plasmonics: Fundamentals and Applications* (Springer, Berlin, 2007).

[18] J. D. Joannopoulos, S. G. Johnson, J. N. Winn, & R. D. Meade, *Photonic Crystals: Molding the Flow of Light (Second Edition)* (Princeton University Press, 2008), 2 edition.

[19] D. E. Chang, A. S. Sørensen, P. R. Hemmer, & M. D. Lukin, Quantum optics with surface plasmons, *Phys. Rev. Lett.* **97**, 053002 (2006).

[20] D. E. Chang, A. S. Sørensen, E. A. Demler, & M. D. Lukin, A single-photon transistor using nanoscale surface plasmons, *Nat. Phys.* **3**, 807–812 (2007).

[21] R. Loudon, *The Quantum Theory of Light* (Oxford University Press, Oxford, 2000), 3rd edition.

[22] W. L. Barnes, A. Dereux, & T. W. Ebbesen, Surface plasmon subwavelength optics, *Nature* **424**, 824–830 (2003).

[23] J. Homola, S. S. Yee, & G. Gauglitz, Surface plasmon resonance sensors: review, *Sensors and Actuators B: Chemical* **54**, 3 – 15 (1999).

[24] B. O. Dabbousi, *et al.*, (CdSe)ZnS core-shell quantum dots: synthesis and characterization of a size series of highly luminescent nanocrystallites, *The Journal of Physical Chemistry B* **101**, 9463–9475 (1997).

[25] J. R. Guest, *et al.*, Measurement of optical absorption by a single quantum dot exciton, *Phys. Rev. B* **65**, 241310 (2002).

[26] A. C. Johnson, *et al.*, Triplet-singlet spin relaxation via nuclei in a double quantum dot, *Nature* **435**, 925–928 (2005).

[27] F. Tinjod, B. Gilles, S. Moehl, K. Kheng, & H. Mariette, II–VI quantum dot formation induced by surface energy change of a strained layer, *Applied Physics Letters* **82**, 4340–4342 (2003).

[28] P. Michler, *et al.*, A quantum dot single-photon turnstile device, *Science* **290**, 2282–2285 (2000).

[29] J. Johansen, *et al.*, Size dependence of the wavefunction of self-assembled InAs quantum dots from time-resolved optical measurements, *Phys. Rev. B.* **77**, 073303 (2008).

[30] O. G. Schmidt, ed., *Lateral Alignment of Epitaxial Quantum Dots* (Springer, Berlin, 2007).

[31] S. Stobbe, J. Johansen, P. T. Kristensen, J. M. Hvam, & P. Lodahl, Frequency dependence of the radiative decay rate of excitons in self-assembled quantum dots: Experiment and theory, *Phys. Rev. B* **80**, 155307 (2009).

[32] P. Michler, ed., *Single Quantum Dots : Fundamentals, Applications and New Concepts* (Springer, Berlin, 2003).

[33] S. L. Chuang, *Physics of Optoelectronic Devices* (John Wiley and sons, inc, 1995).

[34] C. Kittel, *Introduction to Solid State Physics* (John Wiley and sons, inc, 1996).

[35] M. P. Marder, *Condensed Matter Physics* (John Wiley and sons, inc, 2000).

[36] P. T. Kristensen, *Light-matter interaction in nano-structured materials*, Ph.D. thesis, Department of Photonics Engineering at the Technical University of Denmark (2009).

[37] L. Coldren & S. Corzine, *Diode Lasers and Photonic Integrated Circuits* (Wiley, 1995).

[38] J. Johansen, B. Julsgaard, S. Stobbe, J. M. Hvam, & P. Lodahl, Probing long-lived dark excitons in self-assembled quantum dots, *Phys. Rev. B* **81**, 081304 (2010).

[39] M. Bayer, *et al.*, Fine structure of neutral and charged excitons in self-assembled In(Ga)As/(Al)GaAs quantum dots, *Phys. Rev. B* **65**, 195315 (2002).

[40] K. H. Drexhage, Influence of a dielectric interface on fluorescence decay time, *Journal of Luminescence* **1-2**, 693 – 701 (1970).

[41] K. Hennessy, *et al.*, Quantum nature of a strongly coupled single quantum dot–cavity system, *Nature* **445**, 896–899 (2007).

[42] P. Lodahl, *et al.*, Controlling the dynamics of spontaneous emission from quantum dots by photonic crystals, *Nature* **430**, 654–657 (2004).

[43] M. O. Scully & M. S. Zubairy, *Quantum Optics* (Cambridge University Press, 1997).

[44] J. D. Jackson, *Classical Electrodynamics* (John Wiley and sons, 1999).

[45] B. H. Lukas Novotny, *Principles of Nano-Optics* (Cambridge University Press, 2006).

[46] P. Drude, Zur elektronentheorie der metalle, *Annalen der Physik* **306**, 566–613 (1900).

[47] L. C. Andreani, G. Panzarini, & J.-M. Gérard, Strong-coupling regime for quantum boxes in pillar microcavities: Theory, *Phys. Rev. B* **60**, 13276–13279 (1999).

[48] D. P. Craig & T. Thirunamachandran, *Molecular Quantum Electrodynamics: An Introduction to Radiation-Molecule Interactions (Theoretical Chemistry; a Series of Monographs)* (Academic Pr, 1984).

[49] R. J. Glauber & M. Lewenstein, Quantum optics of dielectric media, *Phys. Rev. A* **43**, 467–491 (1991).

[50] K. Jun Ahn & A. Knorr, Radiative lifetime of quantum confined excitons near interfaces, *Phys. Rev. B* **68**, 161307 (2003).

[51] I. D. Rukhlenko, *et al.*, Spontaneous emission of guided polaritons by quantum dot coupled to metallic nanowire: Beyond the dipole approximation, *Opt. Express* **17**, 17570–17581 (2009).

[52] J. R. Zurita-Sánchez & L. Novotny, Multipolar interband absorption in a semiconductor quantum dot. I. Electric quadrupole enhancement, *J. Opt. Soc. Am. B* **19**, 1355–1362 (2002).

[53] J. R. Zurita-Sánchez & L. Novotny, Multipolar interband absorption in a semiconductor quantum dot. II. Magnetic dipole enhancement, *J. Opt. Soc. Am. B* **19**, 2722–2726 (2002).

[54] V. Weisskopf & E. Wigner, Berechnung der natürlichen linienbreite auf grund der diracschen lichttheorie, *Zeitschrift fur Physik* **63**, 54–73 (1930).

[55] A. D. Andreev & E. P. O'Reilly, Optical matrix element in InAs/GaAs quantum dots: Dependence on quantum dot parameters, *Applied Physics Letters* **87**, 213106 (2005).

[56] J. Kalkman, H. Gersen, L. Kuipers, & A. Polman, Excitation of surface plasmons at a $SiO_2$/Ag interface by silicon quantum dots: Experiment and theory, *Phys. Rev. B* **73**, 075317 (2006).

[57] R. R. Schlicher, W. Becker, J. Bergou, & M. O. Scully, Interaction Hamiltonian in quantum optics or: $\vec{p}\cdot\vec{A}$ vs. $\vec{E}\cdot\vec{r}$ revisited, in A. O. Barut, ed., *Quantum Electrodynamics and Quantum Optics* (Boulder, Colorado, 1983).

[58] L. D. Barron & C. G. Gray, The multipole interaction Hamiltonian for time dependent fields, *Journal of Physics A: Mathematical, Nuclear and General* **6**, 59 (1973).

[59] R. G. Woolley, A comment on 'The multipole Hamiltonian for time dependent fields', *Journal of Physics B: Atomic and Molecular Physics* **6**, L97 (1973).

[60] J. J. Sakurai, *Modern Quantum Mechanics* (Addison-Wesley Publishing Company, Inc., 1994).

[61] H. A. Atwater & A. Polman, Plasmonics for improved photovoltaic devices, *Nature Materials* **9**, 205–213 (2010).

[62] A. J. Nozik, Quantum dot solar cells, *Physica E: Low-dimensional Systems and Nanostructures* **14**, 115 – 120 (2002).

[63] D. Fattal, E. Diamanti, K. Inoue, & Y. Yamamoto, Quantum teleportation with a quantum dot single photon source, *Phys. Rev. Lett.* **92**, 037904 (2004).

[64] J. M. Taylor, C. M. Marcus, & M. D. Lukin, Long-lived memory for mesoscopic quantum bits, *Phys. Rev. Lett.* **90**, 206803 (2003).

[65] D. Loss & D. P. DiVincenzo, Quantum computation with quantum dots, *Phys. Rev. A* **57**, 120–126 (1998).

[66] T. Lund-Hansen, *et al.*, Experimental realization of highly efficient broadband coupling of single quantum dots to a photonic crystal waveguide, *Phys. Rev. Lett.* **101**, 113903 (2008).

[67] D. E. Chang, A. S. Sørensen, P. R. Hemmer, & M. D. Lukin, Strong coupling of single emitters to surface plasmons, *Phys. Rev. B* **76**, 035420 (2007).

[68] A. V. Akimov, *et al.*, Generation of single optical plasmons in metallic nanowires coupled to quantum dots, *Nature* **450**, 402–406 (2007).

[69] Y. C. Jun, R. D. Kekatpure, J. S. White, & M. L. Brongersma, Nonresonant enhancement of spontaneous emission in metal-dielectric-metal plasmon waveguide structures, *Phys. Rev. B* **78**, 153111 (2008).

[70] J. L. O'Brien, A. Furusawa, & J. Vuckovic, Photonic quantum technologies, *Nature Photonics* **3**, 687–695 (2009).

[71] S. Strauf, *et al.*, Self-tuned quantum dot gain in photonic crystal lasers, *Phys. Rev. Lett.* **96**, 127404 (2006).

[72] D. K. Gramotnev & S. I. Bozhevolnyi, Plasmonics beyond the diffraction limit, *Nature Photonics* **4**, 83–91 (2010).

[73] J. A. Schuller, *et al.*, Plasmonics for extreme light concentration and manipulation, *Nature Materials* **9**, 193–204 (2010).

[74] R. Kolesov, *et al.*, Wave particle duality of single surface plasmon polaritons, *Nat. Phys.* **5**, 470–474 (2009).

[75] D. J. Bergman & M. I. Stockman, Surface plasmon amplification by stimulated emission of radiation: Quantum generation of coherent surface plasmons in nanosystems, *Phys. Rev. Lett.* **90**, 027402 (2003).

[76] M. A. Noginov, *et al.*, Demonstration of a SPASER-based nanolaser, *Nature* **460**, 1110–1112 (2009).

[77] E. Pehlke, N. Moll, A. Kley, & M. Scheffler, Shape and stability of quantum dots, *Applied Physics A* **65**, 525–534 (1997).

[78] C. Vieu, *et al.*, Electron beam lithography: resolution limits and applications, *Applied Surface Science* **164**, 111 – 117 (2000).

[79] Y. Sun, B. Gates, B. Mayers, & Y. Xia, Crystalline silver nanowires by soft solution processing, *Nano Letters* **2**, 165–168 (2002).

[80] Y. Chen, T. R. Nielsen, N. Gregersen, P. Lodahl, & J. Mørk, Finite-element modeling of spontaneous emission of a quantum emitter at nanoscale proximity to plasmonic waveguides, *Phys. Rev. B* **81**, 125431 (2010).

[81] V. V. Klimov & M. Ducloy, Spontaneous emission rate of an excited atom placed near a nanofiber, *Phys. Rev. A* **69**, 013812 (2004).

[82] S. M. Barnett & R. Loudon, Sum rule for modified spontaneous emission rates, *Phys. Rev. Lett.* **77**, 2444–2446 (1996).

[83] G. Bester, S. Nair, & A. Zunger, Pseudopotential calculation of the excitonic fine structure of million-atom self-assembled $In_{1-x}Ga_xAs/GaAs$ quantum dots, *Phys. Rev. B* **67**, 161306 (2003).

[84] J. J. Finley, *et al.*, Quantum-confined Stark shifts of charged exciton complexes in quantum dots, *Phys. Rev. B* **70**, 201308 (2004).

[85] J. H. Davies, *The Physics of Low-Dimensional Semiconductors* (Cambridge University Press, 1998).

[86] S. Arulkumaran, *et al.*, Investigations on Au, Ag, and Al Schottky diodes on liquid encapsulated Czochralski grown n-GaAs<100>, *Journal of Electronic Materials* **24**, 813–817 (1995).

[87] B. Alén, *et al.*, Oscillator strength reduction induced by external electric fields in self-assembled quantum dots and rings, *Physical Review B (Condensed Matter and Materials Physics)* **75**, 045319 (2007).

[88] J. Hours, P. Senellart, E. Peter, A. Cavanna, & J. Bloch, Exciton radiative lifetime controlled by the lateral confinement energy in a single quantum dot, *Phys. Rev. B* **71**, 161306 (2005).

[89] H. Ditlbacher, *et al.*, Silver nanowires as surface plasmon resonators, *Phys. Rev. Lett.* **95**, 257403 (2005).

[90] Y. X. Benjamin Wiley, Yugang Sun, Polyol synthesis of silver nanostructures: Control of product morphology with Fe(II) or Fe(III) species, *Langmuir* **21**, 8077 (2005).

[91] P. Nagpal, N. C. Lindquist, S.-H. Oh, & N. D. J., Ultrasmooth patterned metals for plasmonics and metamaterials, *Science* **325**, 594 (2009).

[92] T. Deckert-Gaudig, F. Erver, & V. Deckert, Transparent silver microcrystals: Synthesis and application for nanoscale analysis, *Langmuir* **25**, 6032–6034 (2009), pMID: 19415914.

[93] Z. Guo, *et al.*, Facile synthesis of micrometer-sized gold nanoplates through an aniline-assisted route in ethylene glycol solution, *Colloids and Surfaces A: Physicochemical and Engineering Aspects* **278**, 33 – 38 (2006).

[94] G. Lecamp, P. Lalanne, & J. P. Hugonin, Very large spontaneous-emission $\beta$ factors in photonic-crystal waveguides, *Phys. Rev. Lett.* **99**, 023902 (2007).

[95] H. Thyrrestrup, L. Sapienza, & P. Lodahl, Extraction of the beta-factor for single quantum dots coupled to a photonic crystal waveguide, *Applied Physics Letters* **96**, 231106 (2010).

[96] A. Sørensen, D. E. Chang, & M. D. Lukin, Single photon generation and nonlinear optics with surface plasmons, in *Conference on Coherence and Quantum Optics*, CTuB3 (Optical Society of America, 2007).

[97] J. Jung, T. Søndergaard, & S. I. Bozhevolnyi, Theoretical analysis of square surface plasmon-polariton waveguides for long-range polarization-independent waveguiding, *Phys. Rev. B* **76**, 035434 (2007).

[98] Y. Chen, N. Gregersen, T. R. Nielsen, J. Mørk, & P. Lodahl, Spontaneous decay of a single quantum dot coupled to a metallic slot waveguide in the presence of leaky plasmonic modes, *Opt. Express* **18**, 12489–12498 (2010).

[99] J. A. Dionne, L. A. Sweatlock, H. A. Atwater, & A. Polman, Plasmon slot waveguides: Towards chip-scale propagation with subwavelength-scale localization, *Phys. Rev. B* **73**, 035407 (2006).

[100] P. B. Johnson & R. W. Christy, Optical constants of the noble metals, *Phys. Rev. B* **6**, 4370–4379 (1972).

[101] S. Anantathanasarn, *et al.*, Wavelength controlled InAs/InP quantum dots for telecom laser applications, *Microelectronics Journal* **37**, 1461 – 1467 (2006).

[102] M. Zheludkevich, *et al.*, *Protection of Materials and Structures from Space Environment* (Springer, Netherlands, 2004).

[103] S. Zollner, Optical constants and critical-point parameters of GaAs from 0.73 to 6.60 eV, *Journal of Applied Physics* **90**, 515–517 (2001).

[104] D. C. Reynolds, *et al.*, Refractive index, n, and dispersion, -dn/d$\lambda$, of GaAs at 2 K determined from Fabry–Perot cavity oscillations, *Journal of Applied Physics* **61**, 342–345 (1987).

[105] A. Boltasseva, *et al.*, Triangular metal wedges for subwavelength plasmon-polariton guiding at telecom wavelengths, *Opt. Express* **16**, 5252–5260 (2008).

[106] E. D. Palik, *Handbook of Optical Constants of Solids* (Elsevier, 1998).

[107] E. Verhagen, M. Spasenović, A. Polman, & L. K. Kuipers, Nanowire plasmon excitation by adiabatic mode transformation, *Phys. Rev. Lett.* **102**, 203904 (2009).

[108] H. J. Lezec, *et al.*, Beaming light from a subwavelength aperture, *Science* **297**, 820–822 (2002).

[109] S. Kühn, U. Håkanson, L. Rogobete, & V. Sandoghdar, Enhancement of single-molecule fluorescence using a gold nanoparticle as an optical nanoantenna, *Phys. Rev. Lett.* **97**, 017402 (2006).

[110] O. L. Muskens, V. Giannini, J. A. Sanchez-Gil, & J. G. Rivas, Strong enhancement of the radiative decay rate of emitters by single plasmonic nanoantennas, *Nano Letters* **7**, 2871–2875 (2007).

[111] T. H. Taminiau, F. D. Stefani, F. B. Segerink, & N. F. Van Hulst, Optical antennas direct single-molecule emission, *Nature photonics* **2**, 234–237 (2008).

[112] A. G. Curto, *et al.*, Unidirectional emission of a quantum dot coupled to a nanoantenna, *Science* **329**, 930–933 (2010).

[113] M. S. Tomaš, Green function for multilayers: Light scattering in planar cavities, *Phys. Rev. A* **51**, 2545–2559 (1995).

[114] V. V. Klimov & M. Ducloy, Quadrupole transitions near an interface: General theory and application to an atom inside a planar cavity, *Phys. Rev. A* **72**, 043809 (2005).

[115] D. H. Kobe & A. L. Smirl, Gauge invariant formulation of the interaction of electromagnetic radiation and matter, *American Journal of Physics* **46**, 624–633 (1978).

[116] K. Haller, $\vec{A}\cdot\vec{p}$ vs. $\vec{r}\cdot\vec{E}$ minimal coupling and multipolar Hamiltonians in the quantum theory of radiation, in A. O. Barut, ed., *Quantum Electrodynamics and Quantum Optics* (Boulder, Colorado, 1983).

[117] S. Stobbe, *Enhancement of Light-Matter Interaction in Semiconductor Nanostructures*, Ph.D. thesis, Department of Photonics Engineering at the Technical University of Denmark (2009).

[118] J. Johansen, *Decay Dynamics of Quantum Dots in Nanophotonic Structures*, Ph.D. thesis, Department of Photonics Engineering at the Technical University of Denmark (2008).

[119] T. Lund-Hansen, *Time-Resolved Spectroscopy of Quantum Dot Single-Photon Sources*, Ph.D. thesis, Department of Photonics Engineering at the Technical University of Denmark (2009).

[120] http://www.microchem.com/products/pdf/SU-82000DataSheet2000_5thru2015Ver4.pdf .

[121] D. M. Bruls, *et al.*, Determination of the shape and indium distribution of low-growth-rate InAs quantum dots by cross-sectional scanning tunneling microscopy, *Applied Physics Letters* **81**, 1708–1710 (2002).